HIGH QUALITY COMPUTATIONAL SCREENING OF METAL-ORGANIC FRAMEWORKS FOR CONTAMINANT REMOVAL

A Dissertation
Presented to
The Academic Faculty

by

Dalar Nazarian

In Partial Fulfillment
of the Requirements for the Degree
Doctor of Philosophy in the
School of Chemical and Biomolecular Engineering

Georgia Institute of Technology
August 2016

HIGH QUALITY COMPUTATIONAL SCREENING OF METAL-ORGANIC FRAMEWORKS FOR CONTAMINANT REMOVAL

Approved by:

Dr. David Sholl, Advisor
School of Chemical and Biomolecular Engineering
Georgia Institute of Technology

Dr. Krista Walton
School of Chemical and Biomolecular Engineering
Georgia Institute of Technology

Dr. Ryan Lively
School of Chemical and Biomolecular Engineering
Georgia Institute of Technology

Dr. P. Ganesh
Center for Nanophase Material Science
Oak Ridge National Laboratories

Dr. Angus Wilkinson
School of Chemistry and Biochemistry
Georgia Institute of Technology

Date Approved: [May 03, 2016]

Ծնողներիս, Վրեժ եւ Ծաղիկղին

ACKNOWLEDGEMENTS

The list of individuals who have contributed to my completion of this dissertation is packed with colorful, generous, and incredible individuals. These people have my deepest gratitude and respect. Specifically I would like to thank Dr. David Sholl who has been a great mentor, a patient teacher, a supportive advisor, and a role-model to me. His confidence in my abilities and insistence on my personal and professional development have pushed me to grow more than I could have anticipated. I am grateful for his example.

I wish to express my gratitude to my undergraduate research advisor Dr. Nancy Lape for inspiring me to pursue a graduate degree and her continuous support throughout the past four years.

I would also like to thank Dr. Krista Walton, Dr. Ryan Lively, Dr. Angus Wilkinson, and Dr. Ganesh Panchapakesan, my committee members, for their helpful comments and suggestions throughout the Ph.D. process. In particular, thank you to Dr. Ganesh Panchapakesan for his collaboration on the benchmarking portion of this work. I was also fortunate to collaborate with a group of specialists working on related fields through the Nanoporous Materials Genome Center and am grateful for the generous funding provided by the center.

I am also grateful for the training and support provided by the staff and faculty at the School of Chemical and Biomolecular Engineering at Georgia Tech. From the rigorous coursework to the sidebar conversations about work and life balance, they have given me the tools I need to succeed. I especially want to thank Dr. Martha Grover and Dr. Elsa Reichmanis for all their support and enlightening conversations during our monthly

lunches. I am also grateful to Dr. Michael Filler for investing the time to help me become a better educator. This department has been a collaborative, supportive, and exciting home for me.

During my years at Georgia Teach, I had the pleasure of working alongside many bright and dynamic individual whom I now call friends. Within the Sholl Group, I want to especially thank Dr. Jason Gee, Dr. Kelly Nicholson, Dr. Salah E Boulfelfel, and Ross Verploegh for their help and useful discussions. It was these discussions that made this work possible. Thank you to Jeffrey Camp for doing the same, but also for being a collaborator in a significant portion of this work. Your value to this dissertation cannot be overstated.

To the many friends I have met at Georgia Tech, thank you for taking this journey with me. I could not have dreamed of a better second family of misfits to help celebrate life for the past four years. I am honored to have you in my life and excited to share the rest of life's journey with you.

Finally, I would like to thank my family whose support has made this dissertation possible. I am forever indebted to my parents for the countless sacrifices they have made for the success and happiness of their daughters. Thank you to my mother for her unconditional love and my father for his wisdom and patience. Thank you to my sisters who are the only two people in the world who make me feel completely understood. I could not ask for a greater gift.

TABLE OF CONTENTS

LIST OF TABLES

LIST OF FIGURES

SUMMARY

High-throughput computational screening of thousands of metal-organic frameworks (MOFs) have been performed for separation applications using selective adsorption. First, a MOF-specific benchmarking study of DFT functionals for predicting MOF structural parameters, elastic properties, and atomic point charges was performed. To achieve this task, a test set of diverse MOFs with high accuracy experimentally derived crystallographic structures was compiled. Results indicate that the discrepancies in the properties predicted by the various functionals is small compared the accuracy necessary for most practical applications. Motivated by these observations, the PBE functional was used to assign atomic point charges derived from periodic DFT electronic structure calculations for thousands of MOFs. As an example of using these charges, each MOF was examined for adsorptive removal of tert-butyl mercaptan (TBM) from natural gas. Monte Carlo (MC) simulations revealed many candidate MOF structures with high selectivity for TBM. Based on results from the benchmarking study, DFT was used to predict the energy minimized structure of over 800 MOFs. These energy minimized structures are used to analyze the relationship between nanopore structure and gas adsorption properties. Results indicate that structure precision is crucial for MC prediction of CO_2 adsorption in MOFs. Given the findings, preliminary studies of impact of MOF flexibility on the MC prediction of adsorption properties of CO_2 and xylenes were performed.

CHAPTER 1

INTRODUCTION

Separation technologies account for a substantial portion of the energy use in the United States. Innovations in low-energy separation methods, such as adsorption, have the potential to substantially reduce industrial energy consumption. Metal-organic frameworks (MOFs) are a class of materials with great promise in separations. Thousands of MOFs have been synthesized with a range of properties. The engineering challenges in implementing such adsorption based separations include the identification of the appropriate material and the characteristics of the material that enhance adsorption properties. Computational methods can significantly enhance the efficiency with which we study properties of a large set of materials. A combination of geometric, atomic Monte Carlo, density functional theory, and statistical analysis can be applied in high-throughput screening processes to thousands of existing MOFs to quickly identify promising candidates for a range of applications.

1.1 Metal-Organic Frameworks

MOFs are crystalline nanoporous materials of inorganic secondary building units (SBU) connected together with organic linkers. The term MOF first appeared in literature by Yaghi et at. in 1995.[1] The first example of a stable, porous MOF, IRMOF-1, was reported by Eddaudi et al. in 1999.[2] Since their first appearance in literature, thousands of MOF structures have been synthesized.[3] These synthesized materials only represent a small fraction of possible structures. The large number of possible combinations of SBUs and linkers of different length, conformation and functionalization allow for MOFs of versatile

range in pore topologies and chemical environments. Over 137,000 hypothetical MOFs based on 102 SBUs and structures of known MOFs have been identified by Snurr et al..[4] The versatility of MOFs make them attractive for applications such as gas adsorption,[5-7] separation,[8-11] purification,[12] catalysis,[13, 14] chemical sensors,[15, 16] and drug delivery.[17-19] More recently, MOFs have shown their potential for use in liquid phase applications such as adsorption,[20-27] separation[28-32] and catalysis[33, 34]

1.2 MOF Databases

An initial step in computer simulation of MOFs is to obtain crystallographic information of the structure. The experimentally refined crystal structure can be obtained either from the supporting information of the synthesis literature or from the Cambridge Structural Database (CSD).[35] MOF structure data is typically determined using single crystal x-ray diffraction (XRD) or x-ray powder diffraction (XRPD). XRD is typically used to determine structure for crystal sizes larger than 5 micrometers and XRPD is used for smaller crystals.[36] More than 90% of the MOF structures found in the CSD were resolved using XRD. The quality of diffraction tools and characterization conditions play a role in the quality of the crystal data obtained experimentally. The choice of diffractometer may affect the data resolution of resulting crystal structures and structures obtained at higher temperatures will include the impact of thermal motion.[36] These reported structures often include artifacts such as solvent molecules and partially occupied or disordered atoms. Solvent molecules exist because crystal structures are often resolved before activation, with the presence of residual synthesis solvent molecules within the MOF pores. In some cases, the crystal structure data will include the solvent, but in other cases the solvent is not

resolved during the structural refinement. To perform reliable simulations, these components of the crystal structure must be corrected.

The Computation-Ready Experimental MOF (CoRE MOF) database of Chung et al.[37] constructed a large set of experimentally refined MOF structures from the CSD by removing solvent molecules and selecting a single representation of any disordered atoms in the reported structures. The CoRE MOF database eliminates an initial hurdle to high-throughput molecular simulations of MOFs and has already been used to screen MOFs in applications such as methane storage[38] and natural gas (including higher hydrocarbons) storage.[39] While the CoRE MOF database is a helpful step in performing efficient high-throughput screening of MOFs, additional concerns about the MOFs structures should be addressed. Structures resolved with residual solvent within the pores or with solvent molecules bound to the metal centers may adopt a different geometry once solvent is removed. Each MOF in the CoRE MOF database is represented by a structure without solvent. Generating these structures assumed that the structure geometry remains the same after activation.[37]

1.3 DFT for Predicting MOF Structural Properties

Density functional theory (DFT) methods express the ground-state energy of a system as a function of electron density. The use of electron density significantly reduces the number of degrees of freedom in the system. This makes it possible to apply quantum chemistry to larger systems like MOFs, specifically for structural properties. Although DFT methods are exact in principle, they are approximate in practice because the functional that maps between electron density and energy is only known as an approximate. Some examples of such approximate functionals used for MOFs include Perdew-Burke-

Ernzerhof (PBE),[40] Perdew-Wang 91 (PW91)[41], the semiempirical approach of Grimme[42, 43] with PBE-D2, the nonempirical vdW-DF method of Dion et al.,[44] and Minnesota Functionals such as M05 and M06.[45] Poloni et al. have benchmarked a range of DFT functionals, concluding that vdW-DF and vdW-DF2 approaches can predict CO_2 adsorption enthalpies in MOFs with chemical accuracy.[46] Yu et al. have assessed various DFT functionals for prediction of CO_2 adsorption in the CPO-27 MOF by comparing to both experimental and MP2 results.[47] Assessment of the quality of experimental data, specifically structure, for these materials is difficult. However, many computational methods, especially screening procedures, depend critically on access to accurate MOF structure. Although there are multiple possible methods to verify the structure of a MOF, including a vast range of quantum chemistry methods,[48] to date there has been no systematic assessment of methods for MOF structure predictions.

1.4 Monte Carlo Methods for Predicting Adsorption in MOFs

Grand canonical Monte Carlo (GCMC) simulations have played an important role in the development of adsorbents for gas storage and separations.[49-53] GCMC simulations have also been increasingly used to screen big databases of MOFs for application in separations and storage. Such screening studies are accessible given the assumption that the MOF framework can be treated as rigid during the GCMC simulation. While it has been assumed, with the exception of breathing[7, 54-56] and gate-opening[57, 58] MOFs, that the impact of flexibility will be negligible for adsorption simulations, it is also a known fact that MOFs are not rigid. Many studies of gas diffusion in MOFs have demonstrated the importance of small fluctuations in the MOF framework on the predicted adsorption property.[55, 57-59] Recently, there has been development of methods to account for

framework flexibility during GCMC simulations, but these methods are computationally expensive and not yet commonly used.[60-62] While there are numerous examples of computational studies which have successfully reproduced experimental adsorption results, there is currently no consensus on the importance of flexibility on predicting adsorption. However, it is clear that there are cases where flexibility can play an important role, especially when applied to adsorption of larger polar adsorbates.[62, 63]

1.5 References

1. O. Yaghi, G. Li and H. Li, *Nature*, 1995, 378, 703-706.

2. H. Li, M. Eddaoudi, M. O'Keeffe and O. Yaghi, *Nature*, 1999, 402, 276-279.

3. J. Long and O. Yaghi, *Chemical Society Reviews*, 2009, 38, 1213-1214.

4. C. Wilmer, M. Leaf, C. Lee, O. Farha, B. Hauser, J. Hupp and R. Snurr, *Nature Chemistry*, 2012, 4, 83-89.

5. J. Li, R. Kuppler and H. Zhou, *Chemical Society Reviews*, 2009, 38, 1477-1504.

6. A. Millward and O. Yaghi, *Journal of the American Chemical Society*, 2005, 127, 17998-17999.

7. S. Bourrelly, B. Moulin, A. Rivera, G. Maurin, S. Devautour-Vino, C. Serre, T. Devic, P. Horcajada, A. Vimont, G. Clet, M. Daturi, J. Lavalley, S. Loera-Serna, R. Denoyel, P. Llewellyn and G. Ferey, *Journal of the American Chemical Society*, 2010, 132, 9488-9498.

8. R. Kuppler, D. Timmons, Q. Fang, J. Li, T. Makal, M. Young, D. Yuan, D. Zhao, W. Zhuang and H. Zhou, *Coordination Chemistry Reviews*, 2009, 253, 3042-3066.

9. H. Yang, Z. Xu, M. Fan, R. Gupta, R. Slimane, A. Bland and I. Wright, *Journal of Environmental Sciences-China*, 2008, 20, 14-27.

10. E. Haldoupis, S. Nair and D. Sholl, *Journal of the American Chemical Society*, 2010, 132, 7528-7539.

11. S. Keskin, T. van Heest and D. Sholl, *Chemsuschem*, 2010, 3, 879-891.

12. A. Czaja, N. Trukhan and U. Muller, *Chemical Society Reviews*, 2009, 38, 1284-1293.

13. J. Lee, O. Farha, J. Roberts, K. Scheidt, S. Nguyen and J. Hupp, *Chemical Society Reviews*, 2009, 38, 1450-1459.

14. L. Vilhelmsen, K. Walton and D. Sholl, *Journal of the American Chemical Society*, 2012, 134, 12807-12816.

15. S. Achmann, G. Hagen, J. Kita, I. Malkowsky, C. Kiener and R. Moos, *Sensors*, 2009, 9, 1574-1589.

16. A. Khoshaman and B. Bahreyni, *Sensors and Actuators B-Chemical*, 2012, 162, 114-119.

17. K. Taylor-Pashow, J. Della Rocca, Z. Xie, S. Tran and W. Lin, *Journal of the American Chemical Society*, 2009, 131, 14261.

18. P. Horcajada, C. Serre, G. Maurin, N. Ramsahye, F. Balas, M. Vallet-Regi, M. Sebban, F. Taulelle and G. Ferey, *Journal of the American Chemical Society*, 2008, 130, 6774-6780.

19. J. An, S. Geib and N. Rosi, *Journal of the American Chemical Society*, 2009, 131, 8376.

20. A. Nalaparaju and J. Jiang, *Langmuir*, 2012, 28, 15305-15312.

21. N. Khan and S. Jhung, *Angewandte Chemie-International Edition*, 2012, 51, 1198-1201.

22. E. Haque, J. Jun and S. Jhung, *Journal of Hazardous Materials*, 2011, 185, 507-511.

23. K. Cychosz and A. Matzger, *Langmuir*, 2010, 26, 17198-17202.

24. D. Patil, P. Rallapalli, G. Dangi, R. Tayade, R. Somani and H. Bajaj, *Industrial & Engineering Chemistry Research*, 2011, 50, 10516-10524.

25. M. Maes, S. Schouteden, L. Alaerts, D. Depla and D. De Vos, *Physical Chemistry Chemical Physics*, 2011, 13, 5587-5589.

26. B. Van de Voorde, A. Munn, N. Guillou, F. Millange, D. De Vos and R. Walton, *Physical Chemistry Chemical Physics*, 2013, 15, 8606-8615.

27. A. Henschel, I. Senkovska and S. Kaskel, *Adsorption-Journal of the International Adsorption Society*, 2011, 17, 219-226.

28. L. Alaerts, M. Maes, L. Giebeler, P. Jacobs, J. Martens, J. Denayer, C. Kirschhock and D. De Vos, *Journal of the American Chemical Society*, 2008, 130, 14170-14178.

29. K. Cychosz, R. Ahmad and A. Matzger, *Chemical Science*, 2010, 1, 293-302.

30. Z. Hu, Y. Chen and J. Jiang, *Langmuir*, 2013, 29, 1650-1656.

31. J. Gutierrez-Sevillano, D. Dubbeldam, L. Bellarosa, N. Lopez, X. Liu, T. Vlugt and S. Calero, *Journal of Physical Chemistry C*, 2013, 117, 20706-20714.

32. P. Moghadam and T. Duren, *Journal of Physical Chemistry C*, 2012, 116, 20874-20881.

33. M. Alkordi, Y. Liu, R. Larsen, J. Eubank and M. Eddaoudi, *Journal of the American Chemical Society*, 2008, 130, 12639-+.

34. M. Lalonde, O. Farha, K. Scheidt and J. Hupp, *Acs Catalysis*, 2012, 2, 1550-1554.

35. F. H. Allen, *Acta Crystallogr B*, 2002, 58, 380-388.

36. J. Su, E. Kapaca, L. F. Liu, V. Georgieva, W. Wan, J. L. Sun, V. Valtchev, S. Hovmoller and X. D. Zou, *Microporous and Mesoporous Materials*, 2014, 189, 115-125.

37. Y. G. Chung, J. Camp, M. Haranczyk, B. J. Sikora, W. Bury, V. Krungleviciute, T. Yildirim, O. K. Farha, D. S. Sholl and R. Q. Snurr, *Chem Mater*, 2014, 26, 6185-6192.

38. C. M. Simon, J. Kim, D. A. Gomez-Gualdron, J. S. Camp, Y. G. Chung, R. L. Martin, R. Mercado, M. W. Deem, D. Gunter and M. Haranczyk, *Energy & Environmental Science*, 2015, 8, 1190-1199.

39. H. Zhang, P. Deria, O. K. Farha, J. T. Hupp and R. Q. Snurr, *Energy & Environmental Science*, 2015, 8, 1501-1510.

40. J. P. Perdew, J. A. Chevary, S. H. Vosko, K. A. Jackson, M. R. Pederson, D. J. Singh and C. Fiolhais, *Phys Rev B*, 1992, 46, 6671-6687.

41. J. P. Perdew, K. Burke and Y. Wang, *Phys Rev B*, 1996, 54, 16533-16539.

42. S. Grimme, *Journal of Computational Chemistry*, 2006, 27, 1787-1799.

43. S. Grimme, J. Antony, S. Ehrlich and H. Krieg, *Journal of Chemical Physics*, 2010, 132, 154104-154101-154119.

44. D. Langreth, M. Dion, H. Rydberg, E. Schroder, P. Hyldgaard and B. Lundqvist, *International Journal of Quantum Chemistry*, 2005, 101, 599-610.

45. Y. Zhao and D. G. Truhlar, *Journal of Chemical Physics*, 2006, 125, 194101-194101-194117.

46. R. Poloni, B. Smit and J. Neaton, *Journal of Physical Chemistry a*, 2012, 116, 4957-4964.

47. D. Yu, A. Yazaydin, J. Lane, P. Dietzel and R. Snurr, *Chemical Science*, 2013, 4, 3544-3556.

48. S. Odoh, C. Cramer, D. Truhlar and L. Gagliardi, *Chemical Reviews*, 2015, 115, 6051-6111.

49. P. Ryan, O. K. Farha, L. J. Broadbelt and R. Q. Snurr, *Aiche Journal*, 2011, 57, 1759-1766.

50. M. P. Suh, H. J. Park, T. K. Prasad and D. W. Lim, *Chemical Reviews*, 2012, 112, 782-835.

51. H. Wu, Q. Gong, D. Olson and J. Li, *Chemical Reviews*, 2012, 112, 836-868.

52. T. Watanabe, S. Keskin, S. Nair and D. S. Sholl, *Physical Chemistry Chemical Physics*, 2009, 11, 11389-11394.

53. C. M. Simon, J. Kim, D. A. Gomez-Gualdron, J. S. Camp, Y. G. Chung, R. L. Martin, R. Mercado, M. W. Deem, D. Gunter, M. Haranczyk, D. S. Sholl, R. Q. Snurr and B. Smit, *Energy & Environmental Science*, 2015, 8, 1190-1199.

54. T. Loiseau, C. Serre, C. Huguenard, G. Fink, F. Taulelle, M. Henry, T. Bataille and G. Ferey, *Chemistry-a European Journal*, 2004, 10, 1373-1382.

55. A. M. Walker, B. Civalleri, B. Slater, C. Mellot-Draznieks, F. Corà, C. M. Zicovich-Wilson, G. Román-Pérez, J. M. Soler and J. D. Gale, *Angewandte Chemie International Edition*, 2010, 49, 7501--7503.

56. C. Serre, F. Millange, C. Thouvenot, M. Nogues, G. Marsolier, D. Louer and G. Ferey, *Journal of the American Chemical Society*, 2002, 124, 13519-13526.

57. D. Fairen-Jimenez, S. Moggach, M. Wharmby, P. Wright, S. Parsons and T. Duren, *Journal of the American Chemical Society*, 2011, 133, 8900-8902.

58. B. Zheng, Y. Pan, Z. Lai and K. Huang, *Langmuir*, 2013, 29, 8865-8872.

59. N. Ramsahye, G. Maurin, S. Bourrelly, P. Llewellyn, T. Loiseau, C. Serre and G. Ferey, *Chemical Communications*, 2007, DOI: 10.1039/b702986a, 3261-3263.

60. D. Dubbeldam, R. Krishna and R. Q. Snurr, *Journal of Physical Chemistry C*, 2009, 113, 19317-19327.

61. F. Coudert, A. Boutin, M. Jeffroy, C. Mellot-Draznieks and A. Fuchs, *Chemphyschem*, 2011, 12, 247-258.

62. J. A. Gee and D. S. Sholl, *Journal of Physical Chemistry C*, 2016, 120, 370-376.

63. K. V. Lawler, Z. Hulvey and P. M. Forster, *Physical Chemistry Chemical Physics*, 2015, 17, 18904-18907.

CHAPTER 2

COMPUTATIONAL METHODS

2.1 Computational Screening Methods for Nanoporous Materials

Computational screening of metal organic frameworks (MOFs) has become more prevalent with development of efficient algorithms and greater access to crystal structure information of MOFs and high performance computing systems. This section will discuss the methods used in our hierarchical approach to high-throughput screening of MOF adsorption properties. First, we obtain the crystal structure information of a large set of MOFs. Using the structure information, we assess kinetic barriers to adsorption by calculating geometric characteristics such as pore limiting diameters (PLDs) and largest cavity diameters (LCDs)[1]. In the third step, we analyze materials for adsorbates at the limit of infinite dilution. The adsorption is characterized by calculating the Henry's constant and heat of adsorption using a Monte Carlo integration over the potential energy surface. After reducing the number of possible candidates from thousands to hundreds, we analyze materials for adsorbates at the application conditions. In the final step, we analyze materials for stability and ease of synthesis by referring to literature.

2.1.1 CoRE MOF Database

In all screening processes in this work, we have used the Computation-Ready Experimental MOF (CoRE MOF) database of Chung et al.[2]. The CoRE MOFs are a large set of experimentally refined MOF structures from the Cambridge Structural Database[3]

(CSD) that were prepared for molecular simulations by removing solvent molecules and selecting a single representation of any disordered atoms in the reported structures. The CoRE MOF database eliminates an initial hurdle to high-throughput molecular simulations of MOFs and has already been used to screen MOFs in applications such as methane storage, natural gas (including higher hydrocarbons) storage, and geometric analysis of molecular infiltration.

2.1.2 Geometric Characteristic Analysis

Pores in MOFs can have a large variety of shapes and connectivities. Because the goal of this work is determine the adsorption properties within a material, it is important to quantify the features of the pores that controls access of adsorbed molecules. One such geometric characteristic is the pore limiting diameter (PLD) is defined such that a sphere with a diameter larger than the PLD to travel through the structure without overlapping one or more framework atoms. Since MOF atoms are not rigid, molecules larger than the PLD can diffuse (although very slowly) through the MOF. Therefore, a pore is considered accessible by an adsorbate if its pore size is 1 Å smaller than the adsorbate size. Another pore size that can influence a molecule's access to an adsorption site is the largest cavity diameter (LCD), defined as the largest spherical particle that can be inserted at some point within the material's pores without overlapping with any framework atoms[1]. The LCD, PLD, and pore size distributions were calculated using the Zeo++ geometry analysis package.[4]

2.1.3 Henry's Constant and Heat of Adsorption

For selective adsorption, the material of interest should have a high affinity for the adsorbate. An efficient method of quantifying affinity is the Henry's constant, which

defines the slope of the adsorption isotherm in the limit of low activity. A thorough measurement of the Henry's constant would require a fully flexible adsorbent structure and adsorbate molecule. However such calculations are too expensive to apply to a large set of structures. Since structure change will most likely be induced for MOFs with high affinity for the adsorbate, calculating the Henry's constant in rigid MOFs is acceptable for an initial screening method.

For a spatially periodic material simulated as a rigid structure, the Henry's constant can be calculated using the Widom particle insertion method. The Widom particle insertion method is used to calculate the residual chemical potential at the limit of infinite dilution. The Henry's constant (K_H) and the infinite dilution residual chemical potential of an adsorbate are related by

$$K_H = \rho k + B \exp\left(\frac{\mu_{res}}{k_B T}\right) \tag{2.1}$$

where $\mu_{res} = \mu - \mu^{ideal\ gas}$ and μ is the chemical potential of the adsorbate, $\mu^{ideal\ gas}$ is the chemical potential of an ideal gas at the same temperature and pressure, and k_B is the Boltzmann constant.[5] Given these Henry's constants, we can eliminate MOFs with low affinity. The heat of adsorption is related to Henry's constant as

$$Q_s = \frac{dlnK_H}{d\beta} \tag{2.2}$$

where $\beta = \frac{1}{k_B T}$. Given the heat of adsorption, we can draw conclusions regarding the affinity of the adsorbate and the reversibility of the adsorption to the material.[5] Classical grand canonical Monte Carlo (GCMC) simulations of methane adsorption were conducted on all optimized structures using the RASPA 2.0 code[6].

2.1.4 GCMC at Application Conditions

While evaluation of adsorption properties at infinite dilution are an efficient and helpful step in determining adsorption affinity, they represent only a first step in understanding the capabilities of MOFs. Many interesting and worthwhile investigations take place at higher pressure and with multicomponent fluid mixtures. In such cases, simulations are used at the application condition (whether that be higher temperature, pressure or multicomponent mixtures) to determine the adsorbate loading within the framework. Because adsorption is an equilibrium property, it can be averaged over a relevant thermodynamic ensemble, the grand canonical ensemble, which includes all system configurations that correspond to a specific value of temperature, pressure and chemical potential. The grand canonical ensemble can be sampled using a Monte Carlo sampling scheme. This is known as grand canonical Monte Carlo (GCMC). During a Monte Carlo calculation the system undergoes a series of random transformations chosen to sample all the degrees of freedom which are accepted or rejected based on a probability criterion. The Monte Carlo moves required to calculate adsorption typically include insertions and deletions of adsorbate molecules within the unit cell volume, translational moves in all three directions, and rotational moves.[7] For certain calculations, adsorption of tert-butyl mercaptan, we have used the configurational biased Monte Carlo (CBMC) method in improve the move acceptance rate.[8] For adsorption of xylenes, we have adopted a continuous fractional component Monte Carlo (CFCMC) method.[9]

2.2 Potentials for Interatomic Interactions

To predict adsorption properties such Henry's constant and loading, we describe the physisorption inside the framework pores with Van der Waals and Coulombic interactions.

Prediction of adsorption properties in this work was done entirely at the classical level, using an empirical pairwise Lennard-Jones potential function for the var der Waals interactions and Coulomb's law using point charges calculated for each atom in the system. The Lennard-Jones potential for an atomic pair *ij* is defined as

$$U_{LJ}^{ij} = 4\varepsilon\left[\left(\frac{\sigma}{r_{ij}}\right)^{12} - \left(\frac{\sigma}{r_{ij}}\right)^{6}\right] \tag{2.3}$$

where r_{ij} is the interatomic distance between the atoms, σ is a value characteristic of the size of an atom, and ε is a value characteristic of how strongly the atom interacts.[10] For screening studies, these parameters are typically obtained from "off-the shelf" generic force fields. For MOFs, the Universal Force Field (UFF)[11] and the Dreiding[12] force field are commonly used for modeling Van der Waals interactions between guest molecules and adsorbates. Good agreement between experiments and calculations has been observed[13], although progress is increasing in developing more reliable FFs for specific classes of materials using extensive data derived from electronic structure calculations.[14-17] Typically, the σ and ε are typically reported for interactions between atoms of the same type. To combine parameters of interaction between different atom types, the Lorentz-Berthelot mixing rules are commonly applied. This involves taking the mean of the σ parameters and the geometric mean of the ε parameters. [18]

In the event that electrostatic interactions play a role in adsorption, such as CO_2, the interactions between atoms *ij* can be accounted for using Coulomb's law defined as

$$U_c^{ij} = \frac{q_i q_j}{4\pi\varepsilon_0 r_{ij}} \tag{2.4}$$

where q is the point change and ε_0 is the permittivity of vacuum. Calculating point charges will be described in more detail in Section 4.2.2. It is important to note that classical

simulations of MOFs do not have to rely on point charges assigned to framework atoms. If calculations are performed in which the MOF framework is assumed to be rigid, the electrostatic potential due to the MOF can be more accurately represented by directly tabulating the electrostatic potential energy surface as computed from an electronic structure calculation inside the material's pores and interpolating among these tabulated values during classical simulations.[19] Explicitly polarizable forcefields are a promising alternative to fitting to an effective potential. There are ongoing efforts to develop transferable polarizable forcefields, but currently such forcefields have been used mostly for zeolitic imidazolate framework and are not readily implemented in standard classical simulations codes.[20, 21] Therefore, the approach of assigning point charges to framework atoms is likely to remain the standard approach in essentially all classical calculations.

2.3 Density Functional Theory

Density Functional Theory (DFT) is a quantum mechanics-based method for describing a system of electrons and nuclei based on the total electron density. Although DFT methods are exact in principle, they are approximate in practice because the functional that maps between electron density and energy is only known as an approximate.[22] Despite this approximation, DFT has been found to accurately reproduce the geometry of nanoporous materials.[23]

2.3.1 The Functionals

When using DFT, the choice of the approximate functional is crucial to reproduction of material geometry. The simplest approximation to the true Kohn-Sham functional is the local density approximation (LDA) functional defined as the exchange potential for the spatially uniform electron gas with the same density as the local electron

density. The next set of functionals are the generalized gradient approximations (GGA) which take into account the local electron density and the gradient in the electron density. Typical GGA functionals used for MOFs include Perdew-Burke-Ernzerhof (PBE)[24] and Perdew-Wang 91 (PW91)[25]. The next level of theory includes meta-GGA functional which contain the same physical information as the Laplacian of the electron density. The Minnesota Functionals such as M05 and M06 are commonly used meta-GGA functionals.[26] A higher level of theory, hyper-GGA, describes exchange using a mixture of exact exchange and GGA exchange functional. The most commonly used hyper-GGA functional is B3LYP.[27-30]

A shortcoming of DFT is its inadequate description of dispersion interactions. DFT functionals can be further improved by adding dispersion-like contributions to the total energy between each pair of atoms. Two notable methods are the semiempirical approach of Grimme,[31, 32] referred to as DFT-D1, DFTD2, or DFT-D3, and the nonempirical vdW-DF method of Dion et al.[33] Walker et al. compared the performance of several DFT functionals for MIL-53 and show that dispersion corrected functionals are required to predict phase transition behavior and sorption properties of MOF material.[34]

2.3.2 Ab initio Molecular Dynamics[35]

Another use for DFT is to use to perform ab initio molecular dynamics (AIMD), which works by numerically solving Newton's equations of motion and updating the positions and velocities of the particles in the system based on the applied forces. In AIMD, the forces are obtained by performing a DFT calculation at every step. This does not require specification of a force field and is suitable for treating chemically diverse materials.

Because AIMD is a computationally expensive method, the time scales accessible to AIMD are on the order of picseconds.

2.3.3 Elasticity Tensor

DFT methods can also be used to compute the elastic tensor of a material. Each ion is displaced in the direction of each Cartesian coordinate and the forces are calculated using DFT. From the forces the Hessian matrix is determined.[36] Then using the strain-stress relationship obtained by six finite distortions of the lattice the elastic tensor is determined. Using the elastic tensor, mechanical properties (Young's modulus, shear modulus, linear compressibility and Poisson's ratio) were calculated using ELATE, a program by Coudert et al..[37]

2.4 Atomic Point Charge Assignment

There is no unique solution to the task of assigning point charges to represent the full three dimensional distribution of charge in a material.[38] To date, multiple methods have been explored for assigning charges in MOFs. Semi-empirical methods such as charge equilibration have been used because they can be applied without performing an electronic structure calculation.[18, 39] When possible, it is preferable to use atomic charges derived from the electron density calculated from an electronic structure calculation for either discrete clusters cleaved from MOF structures or from fully periodic representations of MOF crystals.[40] Methods for assigning charges based on partitioning the electron density of MOF clusters include ChelpG[41] and more recent charge model techniques.[42]

Cluster techniques have been used to screen small numbers (~ 20 MOFs) of experimentally synthesized MOF for CO_2 storage.[43, 44] Fully periodic methods for partitioning the electron density such as DDEC[38], fitting the local electrostatic field around

atoms such as REPEAT[45], or period populations analysis such as CM5[42] avoid the problem of ambiguous bond termination inherent in cluster based methods.[40, 46] Both the DDEC and REPEAT methods were designed in part to accurately reproduce the electrostatic potential energy surface for locations outside the van der Waals radius of atoms in the material, a property that is desirable in modeling adsorption in MOFs.

Other methods that have been widely used to assign point charges to periodic materials such as Bader charges do not have this property.[38, 47] Unlike the Bader method, DDEC incorporates spherical averaging and uses reference ion densities to enhance the transferability and chemical meaning of the charges. Studies have shown that DDEC charges minimize the Bader overestimation of atomic multipole moments.

2.5 References

1. E. Haldoupis, S. Nair and D. Sholl, *Journal of the American Chemical Society*, 2010, 132, 7528-7539.

2. Y. G. Chung, J. Camp, M. Haranczyk, B. J. Sikora, W. Bury, V. Krungleviciute, T. Yildirim, O. K. Farha, D. S. Sholl and R. Q. Snurr, *Chem Mater*, 2014, 26, 6185-6192.

3. F. H. Allen, *Acta Crystallographica Section B: Structural Science*, 2002, 58, 380-388.

4. T. F. Willems, C. Rycroft, M. Kazi, J. C. Meza and M. Haranczyk, *Microporous and Mesoporous Materials*, 2012, 149, 134-141.

5. K. Shing and K. Gubbins, *Molecular Physics*, 1981, 43, 717-721.

6. D. Dubbeldam, S. Calero, D. Ellis and R. Snurr, unpublished work.

7. B. Smit, K. Esselink and D. Frenkel, *Molecular Physics*, 1996, 87, 159-166.

8. J. I. Siepmann and D. Frenkel, *Molecular Physics*, 1992, 75, 59-70.

9. B. J. Sikora, Y. J. Colon and R. Q. Snurr, *Molecular Simulation*, 2015, 41, 1339-1347.

10. J. Hoshen and R. Kopelman, *Phys Rev B*, 1976, 14, 3438-3445.

11. A. K. Rappé, C. J. Casewit, K. Colwell, W. Goddard and W. Skiff, *Journal of the American Chemical Society*, 1992, 114, 10024-10035.

12. S. L. Mayo, B. D. Olafson and W. Goddard *Journal of Physical Chemistry*, 1990, 94, 8897-8909.

13. N. Khan and S. Jhung, *Angewandte Chemie-International Edition*, 2012, 51, 1198-1201.

14. J. G. McDaniel, S. Li, E. Tylianakis, R. Q. Snurr and J. R. Schmidt, *The Journal of Physical Chemistry C*, 2015, 119, 3143-3152.

15. E. Haldoupis, J. Borycz, H. Shi, K. D. Vogiatzis, P. Bai, W. L. Queen, L. Gagliardi and J. I. Siepmann, *The Journal of Physical Chemistry C*, 2015, 119, 16058-16071.

16. A. Kulkarni and D. S. Sholl, *Langmuir*, 2015.

17. H. Fang, H. Demir, P. Kamakoti and D. S. Sholl, *Journal of Materials Chemistry A*, 2014, 2, 274-291.

18. E. Haldoupis, S. Nair and D. Sholl, *Journal of the American Chemical Society*, 2012, 134, 4313-4323.

19. T. Watanabe, T. A. Manz and D. S. Sholl, *The Journal of Physical Chemistry C*, 2011, 115, 4824-4836.

20. J. G. McDaniel, K. Yu and J. Schmidt, *The Journal of Physical Chemistry C*, 2012, 116, 1892-1903.

21. J. G. McDaniel and J. Schmidt, *The Journal of Physical Chemistry C*, 2012, 116, 14031-14039.

22. D. Sholl and J. A. Steckel, *Density Functional Theory: A Practical Introduction*, Wiley, 2009.

23. S. O. Odoh, C. J. Cramer, D. G. Truhlar and L. Gagliardi, *Chemical Reviews*, 2015, 115, 6051-6111.

24. J. P. Perdew, J. A. Chevary, S. H. Vosko, K. A. Jackson, M. R. Pederson, D. J. Singh and C. Fiolhais, *Phys Rev B*, 1992, 46, 6671-6687.

25. J. P. Perdew, K. Burke and Y. Wang, *Phys Rev B*, 1996, 54, 16533-16539.

26. Y. Zhao and D. G. Truhlar, *Journal of Chemical Physics*, 2006, 125, 194101-194101-194117.

27. A. D. Becke, *Journal of Chemical Physics*, 1993, 98, 5648-5652.

28. C. T. Lee, W. T. Yang and R. G. Parr, *Phys Rev B*, 1988, 37, 785-789.

29. S. H. Vosko, L. Wilk and M. Nusair, *Can J Phys*, 1980, 58, 1200-1211.

30. P. J. Stephens, F. J. Devlin, C. F. Chabalowski and M. J. Frisch, *Journal of Physical Chemistry*, 1994, 98, 11623-11627.

31. S. Grimme, *Journal of Computational Chemistry*, 2006, 27, 1787-1799.

32. S. Grimme, J. Antony, S. Ehrlich and H. Krieg, *Journal of Chemical Physics*, 2010, 132, 154104-154101-154119.

33. D. Langreth, M. Dion, H. Rydberg, E. Schroder, P. Hyldgaard and B. Lundqvist, *International Journal of Quantum Chemistry*, 2005, 101, 599-610.

34. A. M. Walker, B. Civalleri, B. Slater, C. Mellot-Draznieks, F. Corà, C. M. Zicovich-Wilson, G. Román-Pérez, J. M. Soler and J. D. Gale, *Angewandte Chemie International Edition*, 2010, 49, 7501--7503.

35. D. Marx and M. Parrinello, *Journal of Chemical Physics*, 1996, 104, 4077-4082.

36. A. U. Ortiz, A. Boutin, A. H. Fuchs and F. X. Coudert, *Phys Rev Lett*, 2012, 109, 195502-195501-195505.

37. A. U. Ortiz, A. Boutin, A. H. Fuchs and F. X. Coudert, *Journal of Chemical Physics*, 2013, 138, 174703-174701-174708.

38. T. A. Manz and D. S. Sholl, *Journal of Chemical Theory and Computation*, 2010, 6, 2455-2468.

39. C. Wilmer, M. Leaf, C. Lee, O. Farha, B. Hauser, J. Hupp and R. Snurr, *Nature Chemistry*, 2012, 4, 83-89.

40. S. Hamad, S. R. G. Balestra, R. Bueno-Perez, S. Calero and A. R. Ruiz-Salvador, *J Solid State Chem*, 2015, 223, 144-151.

41. C. M. Breneman and K. B. Wiberg, *Journal of Computational Chemistry*, 1990, 11, 361-373.

42. A. V. Marenich, S. V. Jerome, C. J. Cramer and D. G. Truhlar, *Journal of Chemical Theory and Computation*, 2012, 8, 527-541.

43. R. Babarao and J. W. Jiang, *Energy & Environmental Science*, 2008, 1, 139-143.

44. C. Zheng, D. Liu, Q. Yang, C. Zhong and J. Mi, *Industrial & Engineering Chemistry Research*, 2009, 48, 10479-10484.

45. C. Campana, B. Mussard and T. K. Woo, *Journal of Chemical Theory and Computation*, 2009, 5, 2866-2878.

46. S. Keskin, J. Liu, R. B. Rankin, J. K. Johnson and D. S. Sholl, *Industrial & Engineering Chemistry Research*, 2009, 48, 2355-2371.

47. T. Manz and D. Sholl, *Journal of Chemical Theory and Computation*, 2012, 8, 2844-2867.

CHAPTER 3

BENCHMARKING DENSITY FUNCTIONAL THEORY FUNCTIONALS FOR PREDICTING METAL-ORGANIC FRAMEWORK STRUCTURAL PROPERTIES

3.1 Introduction

Simulations have become an indispensable tool to characterize, screen and design Metal Organic Frameworks (MOFs).[1-5] The computational methods for describing molecular adsorption,[1] diffusion,[6, 7] and stability[8] in MOFs include classical simulation (Monte Carlo (MC), Molecular Dynamics (MD) or combination MC-MD) as well as plane-wave Density Functional Theory (DFT). A combination of such methods is used in screening procedures to find promising materials for a range of applications.[9-17] The choice of computational methods depends on the size of the system under consideration, the type of property being predicted and the level of accuracy required. For example, classical methods perform well for predicting gas adsorption in materials without strong binding sites but insufficiently describe strong gas/framework interactions.[18-21]

There are a large number of options available for each method, including choice of code (LAMMPS[22], CHARMM[23], VASP[24], GAUSSIAN[25], etc.), calculation scheme, parameters (force field choice for classical and functional choice for DFT simulations), etc.. The choice of an appropriate method is important for the reproduction of material properties. Therefore, the accuracy of and variance within methods should be quantified before application. The performance of a method can be assessed either by comparing its

The content of this chapter has been published: D. Nazarian, P. Ganesh and D. S. Sholl, J Mater Chem A, 2015, 3, 22432-22440

results to the results of a higher-order computational method or the results of a high quality experiment. Higher-order quantum chemical methods such as MP2[26] and CCSD(T)[27] have been used to benchmark prediction of structural, thermochemical and electronic properties of small molecules in databases such as the S22 database[28-30] and AM database.[31] These methods can be computationally demanding for property prediction in larger periodic structures. For certain property calculations such as adsorbate/adsorbent binding energies in larger structures like MOFs, it is possible to use fragments to represent the crystal system. However, the size of the fragment can significantly impact the results.[1] Witte et al. have assessed the strengths and weakness of multiple wave-function and DFT methods for gas-ligand interactions in MOFs.[32]

Computational methods used for MOFs are typically assessed by their ability to predict experimental results such as lattice parameters and adsorption isotherms. Poloni et al. have benchmarked a range of DFT functionals, concluding that vdW-DF and vdW-DF2 approaches can predict CO_2 adsorption enthalpies in MOFs with chemical accuracy.[33] Yu et al. have assessed various DFT functionals for prediction of CO_2 adsorption in the CPO-27 MOF by comparing to both experimental and MP2 results.[34] Assessment of the quality of experimental data, specifically structure, for these materials is difficult. However, many computational methods, especially screening procedures, depend critically on access to accurate MOF structure data typically obtained using x-ray powder diffraction (XRPD) or single crystal x-ray diffraction (XRD).[35] These reported structures often include complications such as partially occupied or disordered atoms. A common issue for reported structures is residual solvent left in the MOF pores. Structures reported with residual solvent may have a different structure once solvent is removed. Although there are multiple

The content of this chapter has been published: D. Nazarian, P. Ganesh and D. S. Sholl, J Mater Chem A, 2015, 3, 22432-22440

possible methods to verify the structure of a MOF, including a vast range of quantum chemistry methods,[36] to date there has been no systematic assessment of methods for MOF structure predictions.

The aim of this study is to compile and demonstrate the use of a test set of MOFs with high quality experimental structure data and chemical diversity to assess methods for MOF property predictions. We have benchmarked the performance of DFT functionals for prediction of MOF structure by comparing to the accurate experimental data. We also assessed the variance among DFT functionals for prediction of elastic properties and partial charges. Mechanical properties such as Young's modulus, shear modulus, linear compressibility, and Poisson ratio, provide useful insight to MOF flexibility and stability. For example, for MOFs that have a spontaneous ferroelectric polarization, an ease of flexing the materials can result in higher flexoelectricity, a technologically important property that is measurable as well as computable.[37, 38] Such properties can be predicted using *ab initio* or classical methods.[39] Although there are no experimental elastic properties available for the structures in the test set we have compiled, we can quantify the variance in predicted values among functionals for a diverse set of MOFs.

Many computational property predictions for MOFs require a description of the electrostatic potential energy surface.[40, 41] For classical methods, the electrostatic potential energy surface can be described with point charges assigned to each atom in the structure. These point charges are determined using methods such as the Density Derived Electrostatic and Chemical (DDEC) method,[42, 43] which uses ab initio derived electron and spin density distributions as input. We studied the impact of DFT functional on the assigned

The content of this chapter has been published: D. Nazarian, P. Ganesh and D. S. Sholl, J Mater Chem A, 2015, 3, 22432-22440

charges by quantifying the variance in assigned charges calculated using a range of functionals for a diverse test set of MOFs.

3.2 Methods and Computational Details

3.2.1 Criteria for test set

To ensure high quality structural data, only crystallographic structure information obtained from single X-ray diffraction (XRD) data with an R_{F2}-value of less than 10 was used. The R-value quantifies the agreement of calculated and observed structure factors, with lower R-values indicating better structure data.[44] For consistency, only materials with XRD data obtained at room temperature (290-310 K) were considered. XRD data with disorder or residual solvent were excluded. We chose to pursue structures that are solvent and disorder free with low R-value over structures that have been observed frequently in literature. While MOFs like MOF-5, ZIF-8 and HKUST-1 have been repetitively studied, they are reported in the CSD with a range of structures, each with slightly different angles and bond lengths. These differences are most likely due to solvent and disorder. We also endeavored to develop a diverse test set as characterized by the metal of the structure building unit (SBU) of each MOF. Twelve different metal centers were chosen, including two different oxidation states of copper and iron. Below, MOFs are denoted using the REFCODE associated with each structure in the Cambridge Structural Database (CSD) and CoRE MOF database.[17]

3.2.2 Benchmarking DFT functional performance for structure predictions

We considered functionals commonly used in literature for MOF structure and property predictions, including the GGA functionals PBE,[45, 46] and PW91,[45, 47-49] the

dispersion corrected functionals PBE-D2,[50] PBE-D3,[51, 52] and vdw-DF2,[53] and the meta-GGA functional M06L.[54] M06L uses semilocal functionals with parameters fit semiempirically to a diverse data sets which can minimize the deficiencies in treatment of dispersion by traditional functionals.

We chose to include PBE-D3 because unlike PBE-D2, the dispersion coefficient used in PBE-D3 are geometry dependent and are adjusted on the basis of the local coordination number around the atoms of interest. PBE-D3 calculations were carried out using the plane-wave DFT computational package VASP5.3.5. All other calculations were carried out using VASP5.2.12. For all simulations, the Brillouin zone was sampled with a Monkhorst-Pack grid. To determine the parameters for the grid size, two structures were chosen from the test set: a small structure, HAWVOQ01 (Co) with 22 atoms and a moderate size structure, QEJZUB01 (Cu), with 56 atoms. Each structure was energy minimized with varying grid densities. Based on results shown in Figure 3.1, a grid density of 1000 points per atom was chosen and used for all materials.

The content of this chapter has been published: D. Nazarian, P. Ganesh and D. S. Sholl, J Mater Chem A, 2015, 3, 22432-22440

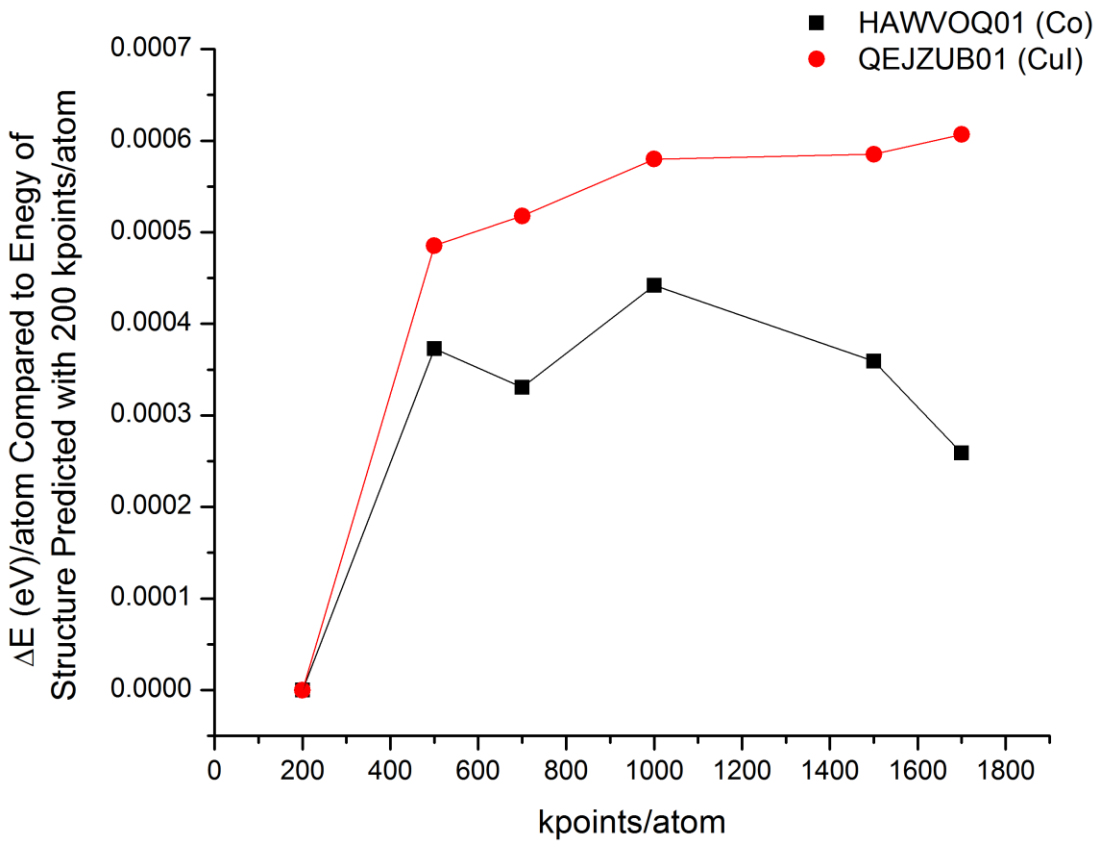

Figure 3.1: HAWVOQ01 and QEJZUB01, with metal centers of Co and Cu, respectively were analyzed for change in predicted energy per atom with increase in kpoint density. The PBE-D2 functional was used. After 1000 kpoints/atom, the predicted energies are within the convergence criteria of 0.0001 eV.

The impact of including spin polarization was also studied. Three structures, HAWVOQ01, HOGWAB, and the anti-ferromagnetic DEMLIR with magnetic centers, Co, Fe, and Fe respectively, were chosen from the test set and energy minimized using the PBE functional. These structures were analyzed for change in volume, the geometry of the local metal center environment (bond length, bond angle, and torsion angle) and ground state energy. We found that including spin polarization noticeably impacts the volume of

The content of this chapter has been published: D. Nazarian, P. Ganesh and D. S. Sholl, J Mater Chem A, 2015, 3, 22432-22440

all three MOFs (see Figure 3.2).This indicates that spin polarization should be included for some structures with ferromagnetic metals. To determine which structures should include spin polarization, an initial, short DFT calculation was performed for each structure to determine its magnetic moment. Structures found to have high magnetic moments greater than 0.004 μB per atom were treated with spin polarization during minimization.

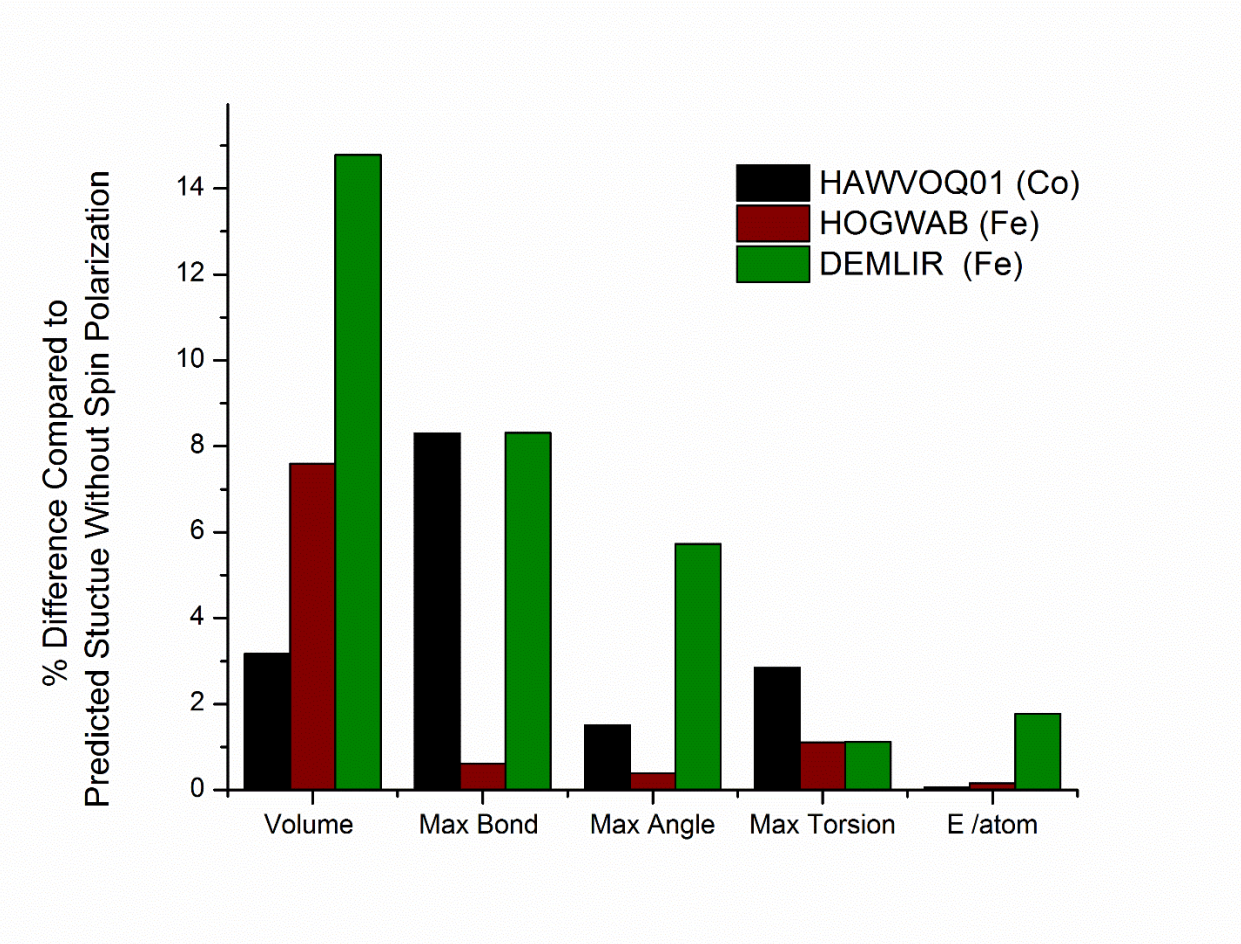

Figure 3.2: HAWVOQ01, HOGWAB, and anti-ferromagnetic DEMLIR with magnetic centers, Co, Fe, and Fe, respectively, were analyzed for change in volume, the geometry of the local metal center environment (bond length, bond angle, and torsion angle) and ground state energy. The results are shown as magnitude of percent change compared to structures predicted without spin polarization. The PBE functional was used.

The content of this chapter has been published: D. Nazarian, P. Ganesh and D. S. Sholl, J Mater Chem A, 2015, 3, 22432-22440

For the two anti-ferromagnetic materials in the test set, DEMLIR (Fe) and MURCEH(Cu), an exhaustive set of initial metal electron spin states were tested. The initial spin configuration that produced the lowest ground state energy was used for remaining calculations. See Table A.1 for initial spin states for each metal in the structures.

Simulations were performed in two parts. First, we performed energy minimization for only ionic positions based on a conjugate gradient algorithm. A subsequent minimization used the final positions of the first minimization, introduced the cell shape and volume as degrees of freedom and switched to a quasi-Newton minimization algorithm. For elements with atomic number higher than 94, the missing C_6 and R_0 parameters needed for the PBE-D2 scheme were taken from the D3 scheme (see Table A.1). To determine the performance of the functionals, strict Cartesian coordinate convergence criteria of a maximum change in system energy of 1×10^{-3} eV per atom and a maximum change in force of 1×10^{-4} eV Å^{-1} were applied to all energy minimization calculations.

The lattice parameters, unit cell volume, bond length, bond angle, and torsion angles associated with the metal center, and pore limiting and largest cavity diameter (PLD and LCD) were measured using the crystallographic data of the experimental and DFT predicted structures. The PLD is defined as the diameter of the smallest sphere along a free path[15]. The LCD is defined as the largest sphere along a path through the material.[15] These pore diameters were measured using the zeo++ software.[55-57] For each MOF, the parameters of each predicted structure were compared to those of the experimental structure. Most results are reported in terms of Mean Absolute Deviation (MAD) from the experimental structure parameters, defined as

The content of this chapter has been published: D. Nazarian, P. Ganesh and D. S. Sholl, J Mater Chem A, 2015, 3, 22432-22440

$$MAD_f = \sum_i^N \frac{abs(x_{exp,i} - x_i)}{N} \quad (3.1)$$

where f is the functional of interest, N is the total number of bond length, angles, or torsions considered for a MOF or a collection of MOFs, $x_{exp,i}$ is the measured value for the experimental structure and x_i is the measured value for the DFT predicted structure. To determine if the calculated MAD of the five functionals are statistically distinguishable, analysis of variance (ANOVA) tests were applied.

3.2.3 Variance in Prediction of Mechanical Properties

The elastic tensor for each structure was calculated using the strain-stress relationship obtained by six finite distortions of the lattice.[58] All calculations were carried out in VASP. Mechanical properties (Young's modulus, shear modulus, linear compressibility and Poisson's ratio) were calculated using ELATE, a program by Coudert et al.[39] The process was repeated for each functional. Convergence tests were performed on 3 of structures with grid densities ranging from 500 to 4,000 kpoints per atom. We found a less than 0.3% difference between moduli calculated for 4,000 and 500 grid density. For consistency with geometry optimization calculations, we chose 1000 points per atom grid density.

3.2.4 Assigning DDEC Point Charges

Charges were assigned using the January 2014 version of the Density Derived Electrostatic and Chemical (DDEC) program provided by Manz et al.[42] DDEC charges have been tested for dense and porous solids, surfaces of solids, small molecules, and large molecules with buried atoms.[59] The electron and spin density distributions used as input

The content of this chapter has been published: D. Nazarian, P. Ganesh and D. S. Sholl, J Mater Chem A, 2015, 3, 22432-22440

for the DDEC code were generated with VASP. Single ionic step self-consistent plane wave DFT calculations with each functional were performed using the same criteria described for energy minimization of the test set. Given that Grimme dispersion corrections are added after the DFT calculation, PBE-D2 and PBE-D3 calculations will result in the same charge density as PBE after a single step. Therefore, D2 and D3 were not included in these calculations. While the DDEC method provides an individual charge for each atom in the system, it is computationally more convenient to distinguish between atom types within a structure. Therefore, point charges were assigned for each atom type in a structure. Atom types were assigned based on the atom's neighboring environment and charges for each atom type are averaged to obtain a net neutral system.

3.3 Test Set Results

An initial set of candidate materials was chosen from the CoRE MOF database.[17] Of the thousands of already synthesized MOFs, approximately 2000 structures were found to be solvent and disorder free. Three quarters of these structures were porous but only 300 qualified as high quality based on R-value. The 300 structures consisted of 75 different metal types, including MOFs with multiple metals. Of these, twelve structures, with a different metal center including two oxidation states of copper and iron (commonly found in MOFs), were chosen for the test set. To increase topological porosity, we included an additional cadmium MOF with a large LCD of 12.59 Å. As shown in Table 3.1, structures also vary in porosity with a LCD range of 1.1 - 12.6 Å.

The content of this chapter has been published: D. Nazarian, P. Ganesh and D. S. Sholl, J Mater Chem A, 2015, 3, 22432-22440

Table 3.1: Test set of chemically diverse MOFs with high quality experimental crystallographic structure information.

Metal	Chemical Formula	REFCODE	LCD (Å)
Ag	$Ag_4C_{12}Cl_4O_8$	RORQOE	1.57
Cd	$Cd_6H_{24}C_{36}N_{36}O_{24}$	GUPCUQ01	12.59
Cd	$Cd_2H_{10}C_{16}N_4O_{10}$	PIJGEV	1.37
Co	$Co_2C_8N_{12}$	HAWVOQ01	1.85
Cu	$Cu_3H_4C_{10}O_{10}$	MURCEH	3.24
Cu	$Cu_8H_8C_8N_{12}Cl_8$	QEJZUB01	1.10
Dy	$Dy_2H_{12}C_{12}N_2O_{16}$	YORSII	1.92
FeII	$Fe_4H_4C_4O_{12}$	HOGWAB	1.83
FeIII	$Fe_4P_4H_{16}C_8O_{24}$	DEMLIR	1.37
Li, Zn	$Li_{32}Zn_{32}H_{24}C_{72}O_{96}$	WAJJAU	7.48
Sm	$Sm_2H_{12}C_{10}O_{14}$	KOMJEC	3.28
Zn	$Zn_1H_4C_4O_4$	OFUWIV01	1.81

3.4 Benchmarking Structural Properties

To compare the performance for overall structure prediction, the predicted lattice parameters and volume of each structure were compared to the experimental values. Figure 3.3 shows the MAD and the corresponding 95% confidence interval, indicated by error bars, of all lattice parameters and volumes in the test set. Figure 3.3 (b) shows an up to 8 % MAD in volume for the structures in the test set. Simulations of properties such as gas adsorption typically require that lattice parameters be accurate within a few percent. The larger change in volume seen in Figure 3.3 (b) are primarily due to the small size of the unit cells in the test set. In such small structures, minor changes in the lattice parameters result in relatively large percent change in cell volume. While there is a difference in the

The content of this chapter has been published: D. Nazarian, P. Ganesh and D. S. Sholl, J Mater Chem A, 2015, 3, 22432-22440

MAD of lattice parameters among the functionals, the MAD of less than 0.3 Å is insignificant relative to the accuracy necessary for most applications.

The dashed lines in Figure 3.3 show that there is essentially no overlap of the confidence intervals of PBE-D2 and PBE-D3 with PBE, PW91, M06L or vdw-DF2. That is, the MAD of PBE-D2 and D3 predicted lattice parameters and volumes show a statistically significant difference from PBE, PW91, and M06L functional predicted values.

The content of this chapter has been published: D. Nazarian, P. Ganesh and D. S. Sholl, J Mater Chem A, 2015, 3, 22432-22440

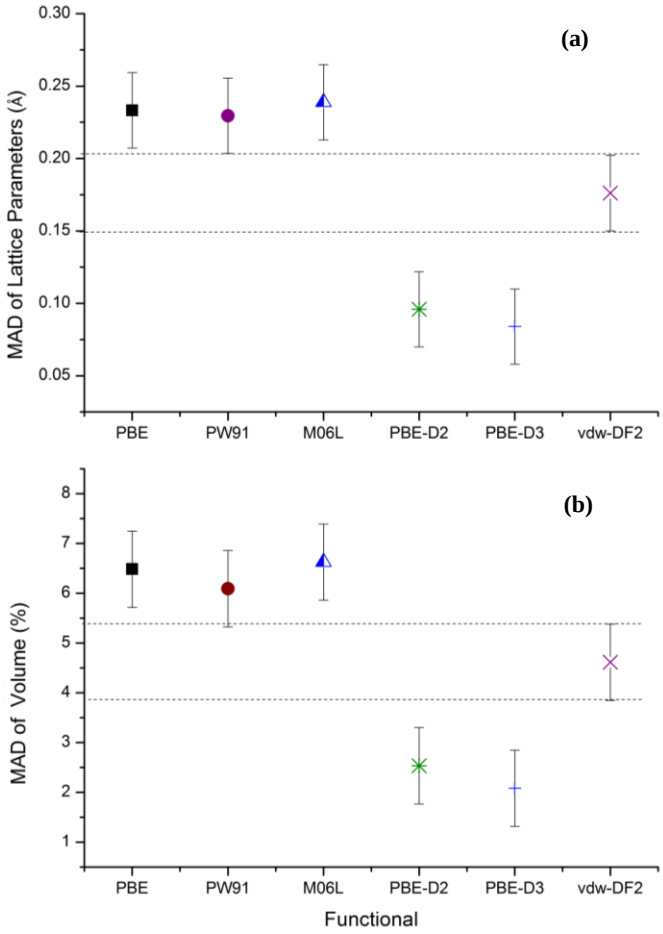

Figure 3.3: The MAD and the corresponding 95% confidence interval (shown as error bars) of all predicted (a) lattice parameters and (b) unit cell volume relative to the experimental structure. The dashed lines encompassing the 95% confidence interval of the vdw-DF2 MAD overlap with values of all other functionals.

The unit cell volumes for the individual materials in the test set are shown in Figure 3.4. The dispersion corrected functionals, PBE-D2, PBE-D3 and vdw-DF2, are in general closest to the experimental values and tend to under predict unit cell volumes. It is important to note that no single functional is the most accurate for all materials. Examples exist, for instance, where the dispersion corrected functionals do not give the most accurate results.

The content of this chapter has been published: D. Nazarian, P. Ganesh and D. S. Sholl, J Mater Chem A, 2015, 3, 22432-22440

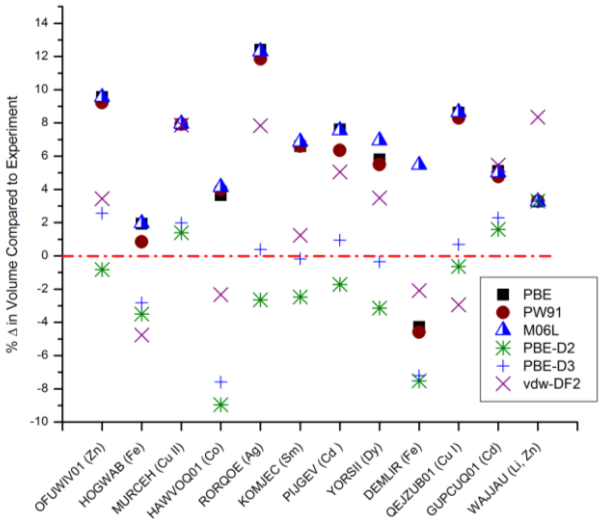

Figure 3.4: The percent deviation of unit cell volume from the experimental structure for each material in the test set. Structures ordered with increasing unit cell volume.

The RORQOE (Ag) DFT predicted structure with PBE, shown in Figure 3.5, has the largest deviation in unit cell parameters (0.5 Å, 0.3 Å, 1.0 Å), shape (orthorhombic to triclinic) and volume (12%). This is due largely to the 10° over prediction of an O-Ag-Cl angle by the PBE, PW91, and M06L functionals. This particular bond angle is predicted more accurately by the PBE-D2 and vdw-DF2 functionals, with a deviation of less than 0.5°. Figure 3.6 examines this example in terms of the charge density predictions of functionals. We analyzed the difference between change density isosurfaces predicted by vdw-DF2 and PBE and found slightly higher oxygen and chlorine density is predicted for oxygen with vdw-DF2 than PBE.

The content of this chapter has been published: D. Nazarian, P. Ganesh and D. S. Sholl, J Mater Chem A, 2015, 3, 22432-22440

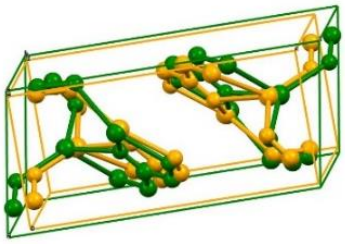

Figure 3.5: The RORQOE (Ag) structure, with yellow representing the experimental structure and green represents the PBE predicted structure, shows a change in shape and size of the unit cell.

Deviations from experimentally predicted structures were investigated in more detail through analysis of bonded interactions. Only bond lengths associated with the metal center and bond and torsion angles with a metal at the center were considered. As shown in 3.7, when averaged among all structures, torsion angles predicted with vdw-DF2 deviate the least from the experimental structures. The MAD of bond angles show that PBE-D3 predicted bond angles deviate the least on average from experimentally observed bond angles.

The content of this chapter has been published: D. Nazarian, P. Ganesh and D. S. Sholl, J Mater Chem A, 2015, 3, 22432-22440

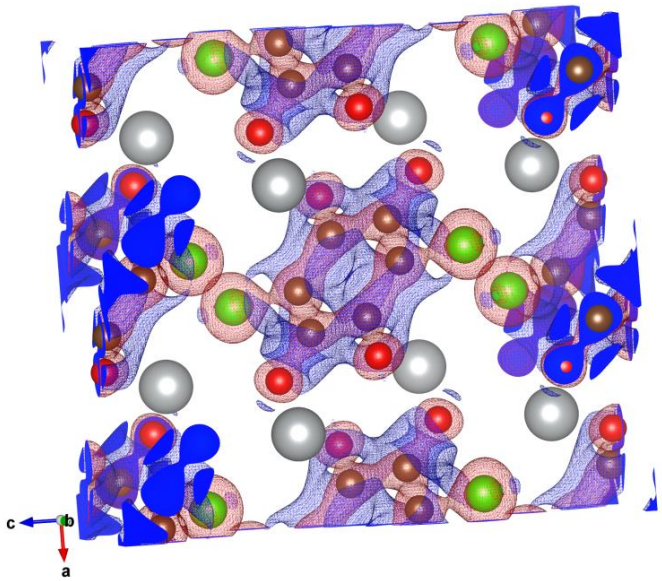

Figure 3.6: Charge density difference isosurfaces between vdw-DF2 and PBE for the experimental structure of RORQOE MOF. (Ag: silver, C: brown, O: red, Cl: green). Isosurfaces plotted at 0.002 electrons/ bohr3 with red indicating a positive and blue a negative difference. Slightly higher oxygen and chlorine density is predicted for oxygen with vdw-DF2 than PBE. When the structure of RORQOE energy is minimized, vdw-DF2 predicts a more accurate, 10° smaller, Cl-Ag-O bond angle then PBE.

The dashed lines in Figure 3.7 (b) show that the confidence interval of vdw-DF2 MAD for bond angles overlaps with the MAD interval of all other functionals. However, the average deviations in bonded interactions are small relative to the accuracy necessary for most applications. When the performance of the different functionals was compared for each structure, we found that the largest deviation in bond length, 0.25 Å, is seen in a Cu-N bond of QEJZUB01 predicted by PBE.

The content of this chapter has been published: D. Nazarian, P. Ganesh and D. S. Sholl, J Mater Chem A, 2015, 3, 22432-22440

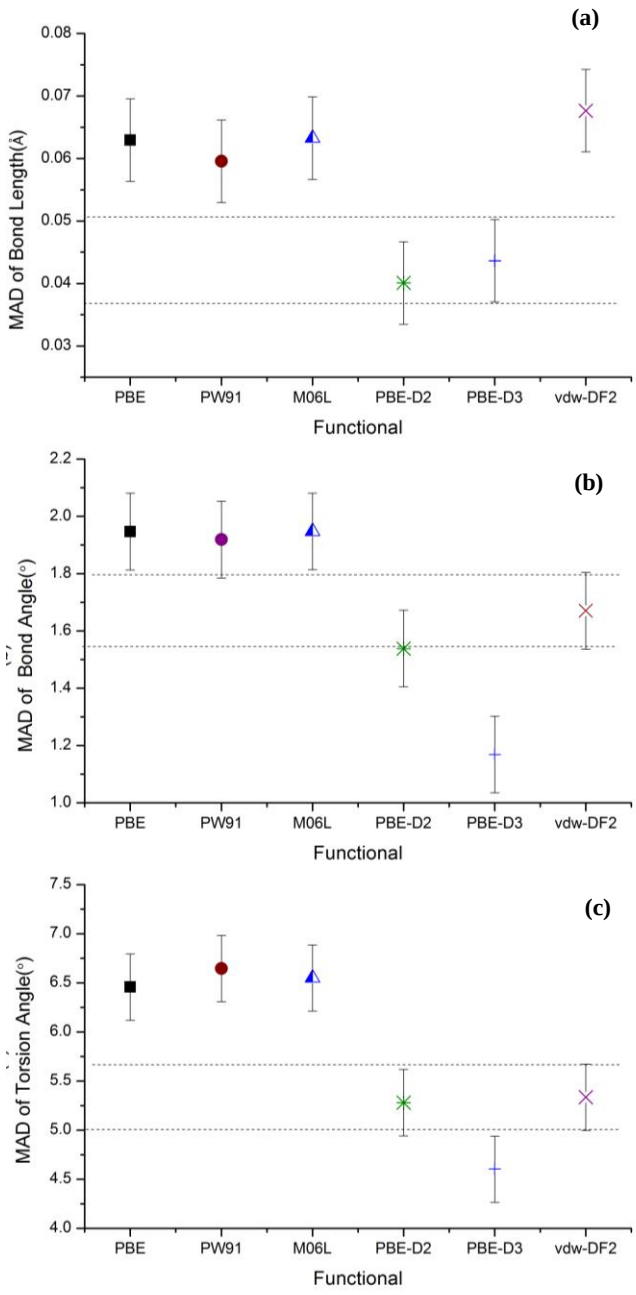

Figure 3.7: The MAD and the 95% confidence interval of bonded parameters relative to the experimental structure are shown. (a) MAD of bond lengths (b) MAD of bond angles (c) MAD of torsion angles.

The content of this chapter has been published: D. Nazarian, P. Ganesh and D. S. Sholl, J Mater Chem A, 2015, 3, 22432-22440

The absolute deviation for the predicted bond angles within a MOF were averaged for each MOF in the test set. No MOFs were found with significant differences among the MAD of PBE, PW91 and M06L predicted bond angles. In the twelve structures, only nine structures were found to have a statistically significant difference in bond angle prediction among functionals. The PBE-D2 and vdw-DF2 predicted a lower deviation for four structures, while PBE, PW91 and M06L predict a lower deviation for three structures.

We observed large deviations of specific angles in the RORQOE (Ag) and HOGWAB (FeII) structures. As discussed earlier, PBE, PW91, and M06L predicted RORQOE (Ag) O-Ag-Cl angles deviate by 12° while vdw-DF2 and PBE-D2 predict the angles more accurately, see Table A.8 for the type and magnitude of angles considered. For HOGWAB (FeII), some vdw-DF2 and PBE-D2 predicted O-Fe-O angles deviate by 13° while PBE, PW91 and M06L functionals predict the angles more accurately. This supports the concept that there is no "one size fits all" option for functionals in terms of accurately predicting MOF structures. This observation suggests that selecting a functional to optimize MOF structures based largely on computational accessibility or efficiency is a reasonable approach when applied to a diverse set of MOFs.

Torsion angles are typically softer degrees of freedom than bond angles and can have larger deviations without significant impact on the structure. In our study we observed deviations in the range of 0.5-20° for torsion angles. When comparing the MAD of torsion angles for structures individually, vdw-DF2 or PBE-D2 results in the lowest MAD for only five structures. One such example is HAWVOQ01 (Co), with a more than 7° larger MAD for PW91 than PBE-D2 (see Table A.5). These differences in torsion angle are apparent in the shift in pore morphology as shown in Figure 3.8. PBE, PW91 and M06L outperformed

The content of this chapter has been published: D. Nazarian, P. Ganesh and D. S. Sholl, J Mater Chem A, 2015, 3, 22432-22440

PBE-D2 and vdw-DF2 with statistical significance for only two structures, DEMLIR and HOGWAB. We found that the HOGWAB iron MOF (with spin polarization included in the DFT predictions) showed a larger deviation between DFT predicted and experimentally observed structures.

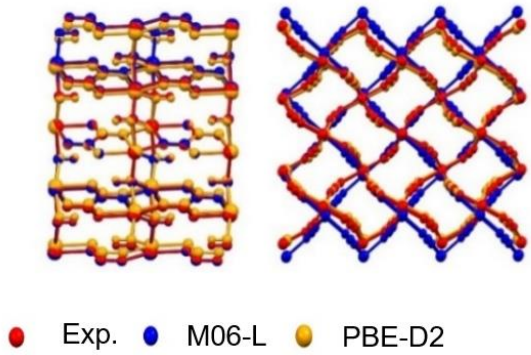

Figure 3.8: Impact of large deviation in torsion angle on pore morphology on HOGWAB (Fe II) and HAWVOQ01 (Co).

Despite deviations in torsion angles, the deviations from the calculated PLD and LCD of the experimental crystallographic structure data are less than 0.5 Å. One-way ANOVA analysis of the deviation of PLDs and LCDs from the experimental values show there is no statistical difference between the MAD of pore descriptors calculated by any of the functionals. That is, we have no evidence that any functional performs better than another (see Figure 3.9). When considering the mean deviation of PLDs and LCDS, we find that PBE-D2 and vdw-DF2 tend under predict PLDs (see Table A.6 and Table A.7).

The content of this chapter has been published: D. Nazarian, P. Ganesh and D. S. Sholl, J Mater Chem A, 2015, 3, 22432-22440

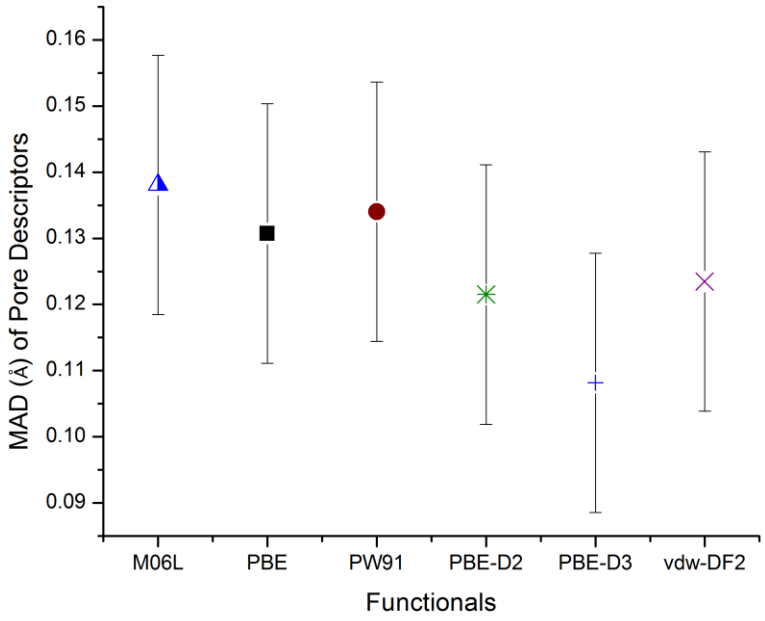

Figure 3.9: MAD of PLDs and LCDs for all MOFs in test set.

3.5 Benchmarking Elastic Properties[5]

The minimum and maximum Young's modulus, shear modulus, linear compressibility and Poisson ratio were calculated for all twelve structures. Figure 3.10 (a) shows the minimum Young's modulus for 10 of 12 structures in the test set, calculated with PBE, PW91, M06L, vdw-DF2, PBE-D2, and PBE-D3 functionals. The results show that the test set includes a wide range of Young's modulus in the MOF's direction of lowest rigidity. According to the nomenclature of Ortiz et al., the large values for minimum Young's modulus indicate that the test set does not contain flexible materials.[39] Figure 3.10 (b) shows similar trends for the minimum shear modulus of the test set MOFs.

The content of this chapter has been published: D. Nazarian, P. Ganesh and D. S. Sholl, J Mater Chem A, 2015, 3, 22432-22440

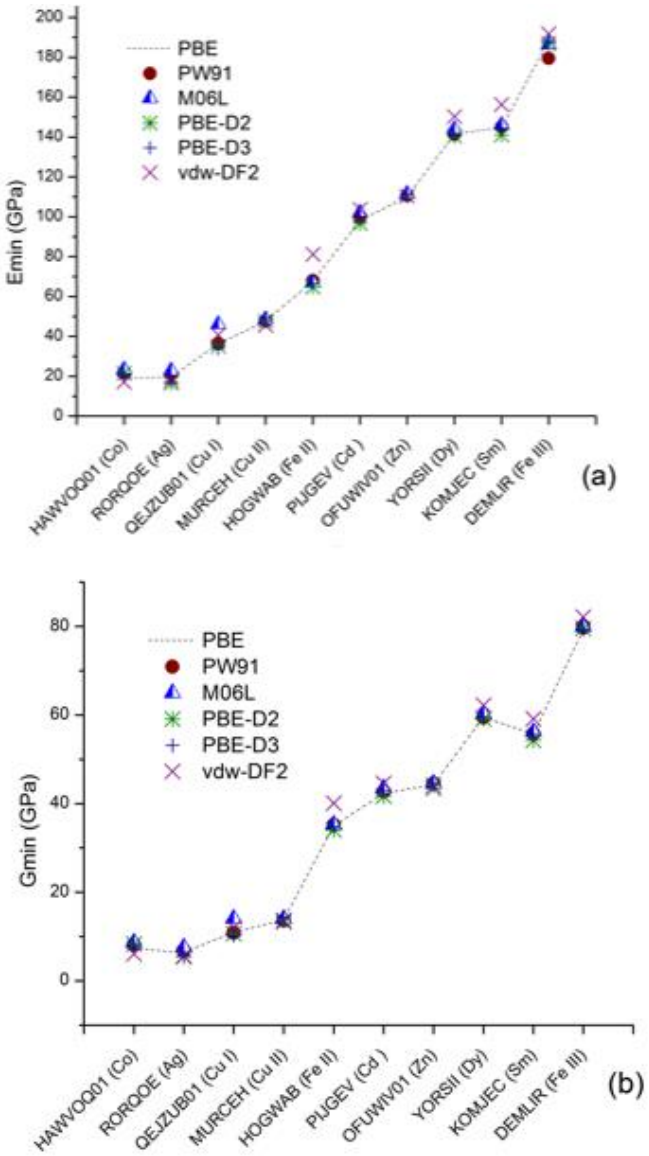

Figure 3.10: The predicted magnitude of the (a) Young's modulus and (b) shear modulus in the direction of least rigidity for each structure computed using six functionals. Results with PBE are shown with a dotted line to guide the eye.

The content of this chapter has been published: D. Nazarian, P. Ganesh and D. S. Sholl, J Mater Chem A, 2015, 3, 22432-22440

When comparing results among functionals, we find that on average vdw-DF2 predicts a more rigid structure. In rigid structures, the minimum Young's modulus has an average range of 9 GPa among functionals and shear an average range of 3 GPa. For some structures, results can differ up to 20 GPa. While this provides a clear distinction between functionals, a 20 GPa deviation is not large relative to the typical accuracy of experimental results available for elastic properties of rigid MOFs such as those in the test set. Tan et al. found that calculated values for moduli are noticeably higher than experimental observations potentially due to physical degradation of the crystals.[60]

As shown in Figure 3.11, the minimum Young's modulus calculated by M06L for QEJZUB01(Cu) noticeably deviates from PBE and PW91. Similarly, M06L calculated maximum linear compressibility and Poisson ratio also deviate significantly, up to 20%, from PBE calculated values. This deviation is higher than those observed for other structures in the test set. The direction of minimum Young's modulus for QEJZUB01 is along the channel axis of the yz plane, see Figure 3.11. Two of the four sides of this channel are dominated by Cl-Cu-Cl bonds. Deformations in these bonds are also responsible for the maximum linear compressibility. Similarly, the Cl-Cu-N bonds adjacent to the channels of the MOF are the primary bonds under strain in the direction of the maximum Poisson ratio of QEJZUB01.

The content of this chapter has been published: D. Nazarian, P. Ganesh and D. S. Sholl, J Mater Chem A, 2015, 3, 22432-22440

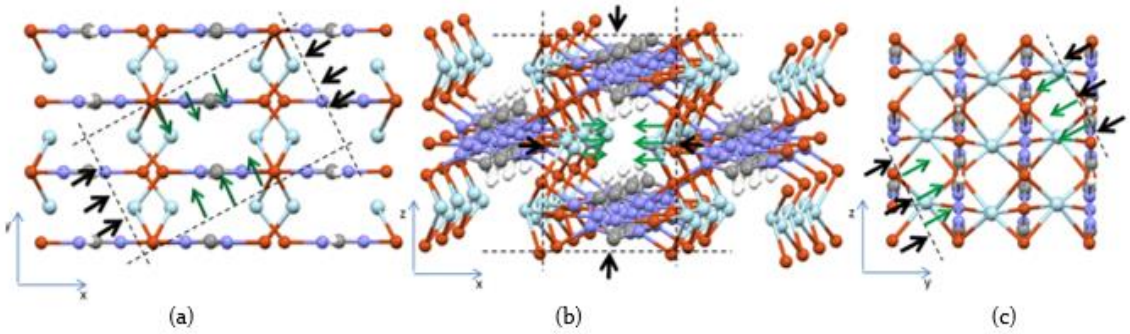

Figure 3.11: The structure of QEJZUB01(Cu) with black arrows showing direction of stress and green arrows showing direction of strain in (a) maximum Poisson ratio, (b) maximum linear compressibility, and (c) minimum Young's modulus.

We find similar deviations of M06 from PBE calculated elastic properties for RORQOE (Ag), another Cl containing MOF. RORQOE has oval shaped channels that run diagonally across its unit cell. The Young's modulus, maximum linear compressibility and Poisson ratio of RORQOE are all properties related to distortions associated with torsion angles of Cl-Ag-O-Ag. For these properties, M06 predict an approximately 20% more rigid MOF than PBE calculated values.

Because of the absence of experimental data, we cannot conclude which functional accurately predicts the elastic properties of these MOFs. However, results for our test set show that vdw-DF2 on average predicts higher rigidity for MOFs compared to other functionals. We also find that while M06 produces comparable results to PBE and PW91 for most MOFs, it predicts more rigid properties associated with Cl-Metal bonds. However, the magnitude of the differences among the functionals is small relative to the accuracy of experimental results.

The content of this chapter has been published: D. Nazarian, P. Ganesh and D. S. Sholl, J Mater Chem A, 2015, 3, 22432-22440

3.6 Benchmarking Atomic Point Charges

Partial charges on individual atoms are not experimental observables, but they are crucial ingredients in many atomistic simulation methods. We examined the influence of functional choice on the assignment of partial charges in two ways. First, we considered differences in partial charges between calculations with different functionals. Second, for each functional, we examined the difference in predicted partial charges for the experimentally observed MOF geometry and the unit cell optimized with DFT.

To compare predicted atomic charges using different functionals, we calculated the DDEC partial charges for only the experimental structure of the MOFs in the test set based on the charge density calculated by PBE, PW91, M06L and vdw-DF2. For each MOF, atoms with similar charge and same coordination were categorized into atom types, resulting in 100 atom types. To quantify the variance in assigned charges among functionals, we calculated the mean absolute deviation relative to other functionals. The MAD for charges is defined as

$$MAD_f = \sum_i \ \sum_{j \neq f} \frac{(x_i^f - x_i^j)}{3N} \tag{3.2}$$

where f is the functional of interest, i is atom type. j is all functionals other than f, x is the DDEC charge, and N is the number of atom types.

One-way ANOVA analysis of the arc cosine normalized partial charges show no difference between the MAD of partial charges calculated by PBE, PW91, and M06L for the MOFs in our test set (see Table 3.2). Unlike the MAD calculated for structural parameters, the magnitude of the MAD calculated for changes here only captures if there is a statistically difference between the predicted charged by different functionals and does

The content of this chapter has been published: D. Nazarian, P. Ganesh and D. S. Sholl, J Mater Chem A, 2015, 3, 22432-22440

not represent the average deviation from a value calculated for an experimental structure. Overall, the variation in partial charges between calculations with different functionals is small. This is consistent with the earlier results of Manz et al. for DFT calculations with a range of materials.[59]

Table 3.2: The MAD and the 95% confidence interval of partial charges.

	MAD	**Confidence interval (+/-)**
PBE	0.0359	0.0042
PW91	0.0380	0.0042
M06L	0.0357	0.0042
vdw-DF2	0.0961	0.0042

Partial charges calculated by vdw-DF2 deviate the most from the calculations of other functionals. The largest deviation was 0.12 electrons for Phosphorus in DEMLIR (FeII) where vdw-DF2 predicted larger charge transfer. Previous studies suggest that the self-consistent vdw-DF2 method is most accurate for layered materials with magnetic metal ions where the charge-transfer plays a crucial role in predicting the spin-polarized electronic configuration of the ion and modifies its polarizability significantly compared to the metal-atom and hence equivalently the empirical C_6 parameter in the Grimme parametrization.[61]

To test the impact of charge transfer as described by vdw-DF2 on prediction of MOF structure, we compared the MAD of predicted partial charges to the difference in MAD of vdw-DF2 and PBE-D2 for structural parameters (see Table A.16). However, no

The content of this chapter has been published: D. Nazarian, P. Ganesh and D. S. Sholl, J Mater Chem A, 2015, 3, 22432-22440

correlation was found between larger charge transfer being predicted by vdw-DF2 and better prediction of structural parameters when compared to PBE-D2.

As discussed above, optimization of MOF structures with DFT gives structures that deviate slightly from experimentally observed crystal structures. To assess the impact of these deviations on partial charges, we calculated the partial charges of the DFT energy minimized structures and compared them to charges calculated for the experimental structure.

For simplicity, we used PBE to assign the partial charges in all cases, noting from the discussion above that the variation in partial charges among functionals (for the same structure) is small. Figure 3.12 shows the MAD of PBE partial charges for each DFT predicted structure relative to the experimental. On average, partial charges change by less than 0.06 electrons. The oxygen atom connected to a Sm atom in the vdw-DF2 predicted KOMJEC(Sm) has the largest change in charge of 0.3 electrons. These results suggest that assigning partial charges directly from experimentally observed MOF structures is likely to be sufficient to provide accurate charges for atomistic simulations; the additional effort of optimizing a structure using DFT prior to assigning charges leads to little change in the assigned charges.

The content of this chapter has been published: D. Nazarian, P. Ganesh and D. S. Sholl, J Mater Chem A, 2015, 3, 22432-22440

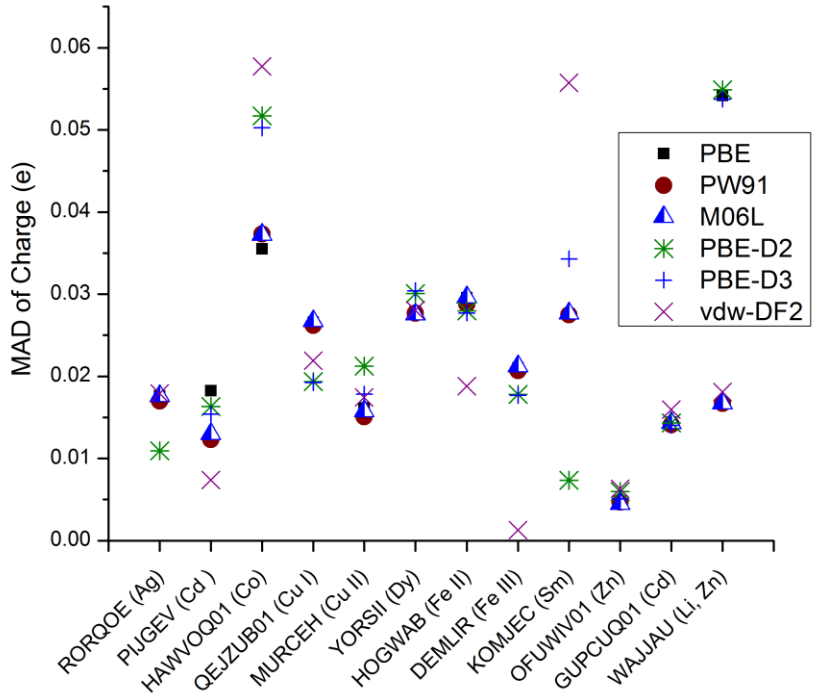

Figure 3.12: The MAD of partial charges calculated for DFT minimized structures (minimized using PBE, PW91, M06L, PBE-D2, PBE-D3, and vdw-DF2) from the partial charges calculated the experimental structures. All partial charges calculated with PBE functional.

3.7 Conclusions

We have compiled a test set of chemically diverse MOFs with high accuracy experimentally derived crystallographic structure data. The test set contains MOFs with a range of topologies and elastic properties. We have demonstrated the significance of a test set with high accuracy structural data by benchmarking the performance of DFT functionals for predicting lattice parameters, unit cell volume, bonded parameters and pore descriptors. We found that for MOFs with magnetic metals, with calculated magnetic moments, spin polarization can significantly impact structure prediction. We have found that on average PBE-D2, PBE-D3, and vdw-DF2 calculations predict a lower deviation in

The content of this chapter has been published: D. Nazarian, P. Ganesh and D. S. Sholl, J Mater Chem A, 2015, 3, 22432-22440

structure than the other functionals we tested. However, we found that M06L, PBE, and PW91 each predict lower deviation for some MOFs in the test set. Despite deviations in unit cell and bonded parameters, we found that all functionals predicted the PLD and LCD for every MOF in the test set within 0.5 Å of the experimental value.

We have also demonstrated the significance of a chemically diverse test set by assessing the variance in DFT functional performance for properties where accurate experimental values are unavailable. We first showed that DFT predicted elastic properties such as the minimum shear modulus and Young's modulus can differ by an average of 3 and 9 GPa for rigid MOFs such as those in the test set. This deviation is small relative to the precision of experimental results available for elastic properties of MOFs. By calculating DDEC partial charges, we found that there is no correlation between the DFT functional's ability to reproduce structural parameters and electrostatic potential surface of a MOF. When assessing the variance in assigned charges among functionals, we showed that there is no difference between the MAD of partial charges calculated by PBE, PW91, and M06L for the MOFs in our test.

Our results indicate that there is no "one size fits all" functional suitable for accurately predicting the structure and other properties of MOFs. That is, no single functional shows accuracy that demonstrates strong statistical significance over other functionals for the full range of MOFs in our test set. Although the choice of specific functional may be justified in some limited instances, it appears that the choice of functional for efforts aimed at screening large numbers of MOFs can justifiably be made based on computational convenience and availability.

The content of this chapter has been published: D. Nazarian, P. Ganesh and D. S. Sholl, J Mater Chem A, 2015, 3, 22432-22440

3.8 References

1. R. B. Getman, Y. S. Bae, C. E. Wilmer and R. Q. Snurr, *Chemical Reviews*, 2012, 112, 703-723.

2. T. Duren, Y. Bae and R. Snurr, *Chemical Society Reviews*, 2009, 38, 1237-1247.

3. J. W. Jiang, *Molecular Simulation*, 2014, 40, 516-536.

4. S. S. Han, J. L. Mendoza-Cortes and W. A. Goddard, *Chemical Society Reviews*, 2009, 38, 1460-1476.

5. S. Keskin, J. Liu, R. B. Rankin, J. K. Johnson and D. S. Sholl, *Industrial & Engineering Chemistry Research*, 2009, 48, 2355-2371.

6. A. I. Skoulidas and D. S. Sholl, *Journal of Physical Chemistry B*, 2005, 109, 15760-15768.

7. J. Li, R. Kuppler and H. Zhou, *Chemical Society Reviews*, 2009, 38, 1477-1504.

8. Y. Cai, A. R. Kulkarni, Y. G. Huang, D. S. Sholl and K. S. Walton, *Cryst Growth Des*, 2014, 14, 6122-6128.

9. Y. J. Colon and R. Q. Snurr, *Chemical Society Reviews*, 2014, 43, 5735-5749.

10. S. G. Han, Y. G. Huang, T. Watanabe, Y. Dai, K. S. Walton, S. Nair, D. S. Sholl and J. C. Meredith, *Acs Comb Sci*, 2012, 14, 263-267.

11. J. Jelic, D. Denysenko, D. Volkmer and K. Reuter, *New J Phys*, 2013, 15, 115004–115015.

12. C. Wilmer, M. Leaf, C. Lee, O. Farha, B. Hauser, J. Hupp and R. Snurr, *Nature Chemistry*, 2012, 4, 83-89.

The content of this chapter has been published: D. Nazarian, P. Ganesh and D. S. Sholl, J Mater Chem A, 2015, 3, 22432-22440

13. A. O. Yazaydin, R. Q. Snurr, T. H. Park, K. Koh, J. Liu, M. D. LeVan, A. I. Benin, P. Jakubczak, M. Lanuza, D. B. Galloway, J. J. Low and R. R. Willis, *Journal of the American Chemical Society*, 2009, 131, 18198–18199.

14. C. E. Wilmer and R. Q. Snurr, *Chem Eng J*, 2011, 171, 775-781.

15. E. Haldoupis, S. Nair and D. Sholl, *Journal of the American Chemical Society*, 2010, 132, 7528-7539.

16. T. Watanabe, S. Keskin, S. Nair and D. S. Sholl, *Physical Chemistry Chemical Physics*, 2009, 11, 11389-11394.

17. Y. G. Chung, J. Camp, M. Haranczyk, B. J. Sikora, W. Bury, V. Krungleviciute, T. Yildirim, O. K. Farha, D. S. Sholl and R. Q. Snurr, *Chem Mater*, 2014, 26, 6185-6192.

18. A. L. Dzubak, L. C. Lin, J. Kim, J. A. Swisher, R. Poloni, S. N. Maximoff, B. Smit and L. Gagliardi, *Nature Chemistry*, 2012, 4, 810-816.

19. L. Chen, C. Morrison and T. Duren, *Journal of Physical Chemistry C*, 2012, 116, 18899-18909.

20. M. Fischer, J. Gomes, M. Froba and M. Jorge, *Langmuir*, 2012, 28, 8537-8549.

21. M. Fischer, B. Kuchta, L. Firlej, F. Hoffman and M. Froba, *Journal of Physical Chemistry C*, 2010, 114, 19116-19126.

22. S. Plimpton, *J Comput Phys*, 1995, 117, 1-19.

23. B. R. Brooks, R. E. Bruccoleri, B. D. Olafson, D. J. States, S. Swaminathan and M. Karplus, *Journal of Computational Chemistry*, 1983, 4, 187-217.

24. G. Kresse and J. Furthmuller, *Phys Rev B*, 1996, 54, 11169-11186.

25. M. J. Frisch, G. W. Trucks, H. B. Schlegel, G. E. Scuseria, M. A. Robb, J. R. Cheeseman, G. Scalmani, V. Barone, B. Mennucci, G. A. Petersson, H. Nakatsuji, M.

Caricato, X. Li, H. P. Hratchian, A. F. Izmaylov, J. Bloino, G. Zheng, J. L. Sonnenberg, M. Hada, M. Ehara, K. Toyota, R. Fukuda, J. Hasegawa, M. Ishida, T. Nakajima, Y. Honda, O. Kitao, H. Nakai, T. Vreven, J. A. Montgomery Jr., J. E. Peralta, F. Ogliaro, M. J. Bearpark, J. Heyd, E. N. Brothers, K. N. Kudin, V. N. Staroverov, R. Kobayashi, J. Normand, K. Raghavachari, A. P. Rendell, J. C. Burant, S. S. Iyengar, J. Tomasi, M. Cossi, N. Rega, N. J. Millam, M. Klene, J. E. Knox, J. B. Cross, V. Bakken, C. Adamo, J. Jaramillo, R. Gomperts, R. E. Stratmann, O. Yazyev, A. J. Austin, R. Cammi, C. Pomelli, J. W. Ochterski, R. L. Martin, K. Morokuma, V. G. Zakrzewski, G. A. Voth, P. Salvador, J. J. Dannenberg, S. Dapprich, A. D. Daniels, Ö. Farkas, J. B. Foresman, J. V. Ortiz, J. Cioslowski and D. J. Fox, *Journal*, 2009.

26. C. Moller and M. S. Plesset, *Phys Rev*, 1934, 46, 0618-0622.

27. M. Musial and R. J. Bartlett, *Journal of Chemical Physics*, 2007, 127, 024106-024101-024109.

28. P. Jurecka, J. Sponer, J. Cerny and P. Hobza, *Physical Chemistry Chemical Physics*, 2006, 8, 1985-1993.

29. Y. Zhao and D. G. Truhlar, *Journal of Physical Chemistry C*, 2008, 112, 4061-4067.

30. M. Xue, G. S. Zhu, Y. X. Li, X. J. Zhao, Z. Jin, E. Kang and S. L. Qiu, *Cryst Growth Des*, 2008, 8, 2478-2483.

31. M. Korth and S. Grimme, *Journal of Chemical Theory and Computation*, 2009, 5, 993-1003.

32. J. Witte, J. Neaton and M. Head-Gordon, *Journal of Chemical Physics*, 2014, 140, 104707-104701-104709.

The content of this chapter has been published: D. Nazarian, P. Ganesh and D. S. Sholl, J Mater Chem A, 2015, 3, 22432-22440

33. R. Poloni, B. Smit and J. Neaton, *Journal of Physical Chemistry a*, 2012, 116, 4957-4964.

34. D. Yu, A. Yazaydin, J. Lane, P. Dietzel and R. Snurr, *Chemical Science*, 2013, 4, 3544-3556.

35. P. A. Jacobs, E. M. Flanigen, J. C. Jansen and H. van Bekkum, *Introduction to Zeolite Science and Practice*, Elsevier Science, 2001.

36. S. Odoh, C. Cramer, D. Truhlar and L. Gagliardi, *Chemical Reviews*, 2015, 115, 6051-6111.

37. W. Zhang and R. G. Xiong, *Chemical Reviews*, 2012, 112, 1163-1195.

38. J. W. Hong and D. Vanderbilt, *Phys Rev B*, 2013, 88, 174107-174101-174124.

39. A. U. Ortiz, A. Boutin, A. H. Fuchs and F. X. Coudert, *Phys Rev Lett*, 2012, 109, 195502-195501-195505.

40. J. Karra and K. Walton, *Langmuir*, 2008, 24, 8620-8626.

41. Q. Y. Yang and C. L. Zhong, *Chemphyschem*, 2006, 7, 1417-1421.

42. T. Manz and D. Sholl, *Journal of Chemical Theory and Computation*, 2012, 8, 2844-2867.

43. T. Watanabe, T. A. Manz and D. S. Sholl, *Journal of Physical Chemistry C*, 2011, 115, 4824-4836.

44. P. JONES, *Chemical Society Reviews*, 1984, 13, 157-172.

45. J. P. Perdew, K. Burke and M. Ernzerhof, *Phys Rev Lett*, 1996, 77, 3865-3868.

46. J. P. Perdew, K. Burke and M. Ernzerhof, *Phys Rev Lett*, 1997, 78, 1396-1396.

47. J. P. Perdew, J. A. Chevary, S. H. Vosko, K. A. Jackson, M. R. Pederson, D. J. Singh and C. Fiolhais, *Phys Rev B*, 1993, 48, 4978-4978.

The content of this chapter has been published: D. Nazarian, P. Ganesh and D. S. Sholl, J Mater Chem A, 2015, 3, 22432-22440

48. J. P. Perdew, J. A. Chevary, S. H. Vosko, K. A. Jackson, M. R. Pederson, D. J. Singh and C. Fiolhais, *Phys Rev B*, 1992, 46, 6671-6687.

49. J. P. Perdew, K. Burke and Y. Wang, *Phys Rev B*, 1998, 57, 14999-14999.

50. S. Grimme, *Journal of Computational Chemistry*, 2006, 27, 1787-1799.

51. S. Grimme, J. Antony, S. Ehrlich and H. Krieg, *Journal of Chemical Physics*, 2010, 132, 154104-154101-154119.

52. S. Grimme, S. Ehrlich and L. Goerigk, *Journal of Computational Chemistry*, 2011, 32, 1456-1465.

53. K. Lee, E. D. Murray, L. Z. Kong, B. I. Lundqvist and D. C. Langreth, *Phys Rev B*, 2010, 82, 081101-081101-081104.

54. Y. Zhao and D. G. Truhlar, *Journal of Chemical Physics*, 2006, 125, 194101-194101-194117.

55. R. L. Martin, B. Smit and M. Haranczyk, *J Chem Inf Model*, 2012, 52, 308-318.

56. T. F. Willems, C. Rycroft, M. Kazi, J. C. Meza and M. Haranczyk, *Microporous and Mesoporous Materials*, 2012, 149, 134-141.

57. M. Pinheiro, R. L. Martin, C. H. Rycroft and M. Haranczyk, *CrystEngComm*, 2013, 15, 7531-7538.

58. Y. Le Page and P. Saxe, *Phys Rev B*, 2002, 65, 104104-104101-104114.

59. T. A. Manz and D. S. Sholl, *Abstracts of Papers of the American Chemical Society*, 2010, 240.

60. J. C. Tan and A. K. Cheetham, *Chemical Society Reviews*, 2011, 40, 1059-1080.

61. P. Ganesh, J. Kim, C. Park, M. Yoon, F. A. Reboredo and P. R. C. Kent, *Journal of Chemical Theory and Computation*, 2014, 10, 5318-5323.

The content of this chapter has been published: D. Nazarian, P. Ganesh and D. S. Sholl, J Mater Chem A, 2015, 3, 22432-22440

CHAPTER 4

A COMPREHENSIVE SET OF HIGH QUALITY POINT CHARGES FOR SIMULATIONS OF METAL-ORGANIC FRAMEWORKS

4.1 Introduction

Computer simulations are an indispensable tool for studying characteristics that emerge from interactions between adsorbates and MOF frameworks. Electronic structure calculations such as DFT and other quantum chemistry methods have been shown to reliably match experimental measurements of properties of MOFs such as adsorbate interaction energies.[1] It is computationally infeasible, however, to use electronic structure methods to simulate phenomenon such as adsorbate diffusion occurring in timescales of nanoseconds or longer. Similarly, grand canonical Monte Carlo (GCMC) simulations of adsorption within nanopores require thousands or millions of computational iterations to converge and thus cannot be directly simulated with electronic structure methods. For these reasons, simulations of MOFs often rely on classical force fields (FFs), especially in efforts to examine large numbers of materials.[2-6] In many cases, calculations of this sort are based on generic ("off the shelf") FFs with increasing progress in developing more reliable FFs for specific classes of materials using extensive data derived from electronic structure calculations.[5, 7-9] This parameterization approach has been successful in reproducing experimental adsorbate diffusion coefficients and adsorption isotherms in MOFs.[9]

In essentially all FF calculations with MOFs, Coulombic interactions between atoms in a MOF and also between those atoms and adsorbate molecules are modeled by

The content of this chapter has been published: D. Nazarian, J. S. Camp and D. S. Sholl, Chem Mater, 2016, 28, 785-793.

assigning point charges to each atom of the framework. The assignment of point charges to MOF atoms is therefore a necessary step in enabling computational screening of large libraries of MOFs. Because there is no unique solution to the task of assigning point charges to represent the full three dimensional distribution of charge in a material,[10] multiple methods have been explored for assigning charges in MOFs. Semi-empirical methods such as charge equilibration have been used because they can be applied without performing an electronic structure calculation.[11, 12] When possible, it is preferable to use atomic charges derived from the electron density calculated from an electronic structure calculation for either discrete clusters cleaved from MOF structures or from fully periodic representations of MOF crystals.[13] Methods for assigning charges based on partitioning the electron density of MOF clusters include ChelpG[14] and more recent charge model techniques.[15] Cluster techniques have been used to screen small numbers (~ 20 MOFs) of experimentally synthesized MOF for CO_2 storage.[16, 17] Fully periodic methods for partitioning the electron density such as DDEC,[10] fitting the local electrostatic field around atoms such as REPEAT,[18] or periodic populations analysis such as CM5[15] avoid the problem of ambiguous bond termination inherent in cluster based methods.[13, 19] Both the DDEC and REPEAT methods were designed in part to accurately reproduce the electrostatic potential energy surface for locations outside the van der Waals radius of atoms in the material, a property that is desirable in modeling adsorption in MOFs. Other methods that have been widely used to assign point charges to periodic materials such as Bader charges, do not have this property.[10, 20] Unlike the Bader method, DDEC incorporates spherical averaging and uses reference ion densities to enhance the transferability and chemical meaning of the charges. In one example of using charge

The content of this chapter has been published: D. Nazarian, J. S. Camp and D. S. Sholl, Chem Mater, 2016, 28, 785-793.

assignments from electronic structure calculations, the DDEC method was used to assign charges to 359 experimentally synthesized MOFs to screen for application in CO_2/N_2 separation.[21] This represented a significant computational investment because DDEC requires a DFT calculation for each periodic MOF structure. The study showed that DDEC charges minimize the Bader overestimation of atomic multipole moments.[22]

It is important to note that classical simulations of MOFs do not have to rely on point charges assigned to framework atoms. If calculations are performed in which the MOF framework is assumed to be rigid, the electrostatic potential due to the MOF can be more accurately represented by directly tabulating the electrostatic potential energy surface as computed from an electronic structure calculation inside the material's pores and interpolating among these tabulated values during classical simulations.[23] Although this approach is conceptually appealing, it cannot be used easily in any simulation where flexibility in the MOF framework is included. Polarizable forcefields are a promising alternative to fitting to an effective potential. There are ongoing efforts to develop transferable polarizable forcefields, but currently such forcefields have been used mostly for zeolitic imidazolate frameworks and are not readily implemented in standard classical simulations codes.[24] Therefore, the approach of assigning point charges to framework atoms is very likely to remain the standard approach in essentially all classical calculations.

The central result of this chapter is to report atomic point charge assignments for 2,932 experimentally synthesized MOF structures using plane wave DFT calculations and the DDEC charge partitioning method. The great majority of these experimentally reported MOF structures were gathered from the Computation-Ready Experimental MOF (CoRE MOF) database of Chung et al.[25] The CoRE MOFs are a large set of experimentally refined

The content of this chapter has been published: D. Nazarian, J. S. Camp and D. S. Sholl, Chem Mater, 2016, 28, 785-793.

MOF structures from the Cambridge Structural Database[26] (CSD) that were prepared for molecular simulations by removing solvent molecules and selecting a single representation of any disordered atoms in the reported structures. The atomic point charges calculated in this work are publicly available as a supplement to the CoRE MOF database. To date, the CoRE MOF database has been used to screen MOFs in applications that do not require atomic point charges such as methane storage,[27] natural gas (including higher hydrocarbons) storage,[28] and geometric analysis of molecular infiltration.[29] Our dataset of DDEC derived atomic point charges will enable use of the CoRE MOF structures for a far broader range of applications where electrostatic interactions must be included such as simulations of the adsorption and diffusion of polar or quadrupolar adsorbates.

Excluding duplicate copies of MOF structures such as CuBTC that are represented more than once in the CoRE MOF database, we have performed periodic DFT calculations and assigned atomic point charges to framework atoms for over 2,000 unique experimentally synthesized MOFs. We have analyzed this dataset in two ways. First, we investigated whether atomic point charges on metal atoms can be inferred from their bonding connectivity. This has been proposed as a general approach for estimating framework charges in metal-organic frameworks.[30] Second, we compared our dataset to results from the extended charge equilibration method (EQeq)[12] to assess the accuracy of semi-empirical charge equilibration methods for MOFs. Semi-empirical methods such as EQeq and the periodic charge equilibration method (PQeq)[11, 31] are typically employed in literature because they are much less computationally expensive than charge assignments based on electronic structure calculations.[32]

The content of this chapter has been published: D. Nazarian, J. S. Camp and D. S. Sholl, Chem Mater, 2016, 28, 785-793.

4.2 Methods and Computational Details

4.2.1 Selection of MOF structures

Our starting dataset of MOF structures included each of the 4,519 computation-ready MOF structures distributed in the CoRE MOF database without mobile charge compensating ionic species.[25] To these CoRE MOF structures, we added 90 commonly studied MOFs distributed with the RASPA 1.0 molecular simulation code.[32] The CoRE MOF structures include duplicates for many of the most common MOFs deposited in the Cambridge Structural Database[16] such as CuBTC and MIL-53(Al).

For the purpose of analyzing patterns such as the distribution of charges on equivalent metal atoms, we identified duplicate representations of MOFs in our starting dataset. To find these duplicate structures, each structure was compared in a pairwise manner with each other structure using the Python Materials Genomics (Pymatgen) package.[33] First, the stoichiometry and number of atomic species in each P1 cell were compared. Structures with the same number and type of atoms were reduced to Niggli cells[34] (unique primitive unit cells with the shortest possible lattice vectors) and the root-mean-square deviation (RMSD) in atomic positions was calculated. Structures with a RMSD of less than 0.1 Å were considered equivalent. For MOF structures with multiple representations in our starting dataset, the structure with the lowest experimental R-value was chosen to represent the structure. The R-value quantifies the agreement of calculated and observed structure factors, with lower R-values indicating better structure data. The material with the largest number of structures in the CoRE MOF database is CuBTC (also known as HKUST-1), which is represented by 60 distinct CSD entries. This analysis shows

The content of this chapter has been published: D. Nazarian, J. S. Camp and D. S. Sholl, Chem Mater, 2016, 28, 785-793.

that among the 4,519 structures we examined from the CoRE MOF database, there are 3,852 distinct materials.

4.2.2 Atomic point charge assignment

A single self-consistent ionic step was attempted in the VASP 5.3.5 plane-wave DFT package for each MOF in our starting dataset to generate the electron and spin density distributions used as inputs for point charge assignment.[35] We have previously shown that there is negligible difference in the DDEC derived atomic point charges from electronic densities generated with the PBE, PW91, M06L or vdw-DF2 functionals for a diverse test set of MOF structures.[36] This is consistent with earlier results by Manz and Sholl for a broad range of materials.[10] The PBE functional was used throughout this work to minimize computational expense. Calculations on the same test set of MOFs mentioned above also indicated negligible differences in point charges between calculations using the experimental structures reported in the CoRE MOF database and structures that were fully geometrically optimized with DFT.[36] As a result, geometric relaxation of the MOFs was not employed for any of the calculations described below. For most structures, the Brillouin zone was sampled with a 1000 points per atom density Monkhorst-Pack grid. For about 200 structures, calculations with a Gamma grid was necessary for proper convergence (see table Table B.1).

Spin-polarization was included for all calculation, adopting a ferromagnetic high spin states for magnetic elements.[37, 38] While there are many structures in the database that exhibit antiferromagnetic spin ordering, it is difficult to efficiently identify these structures *a priori*. We have found that for Cu-BTC, which includes a copper dimer with a ground state antiferromagnetic spin state,[39, 40] a ferromagnetic calculation results in a Cu charge

The content of this chapter has been published: D. Nazarian, J. S. Camp and D. S. Sholl, Chem Mater, 2016, 28, 785-793.

that is different by less than 0.02 electrons than the antiferromagnetic structure (Table 5.1). This observation suggests that using ferromagnetic states is sufficient for assigning point charges.

Table 4.1: DDEC atomic point charges calculated for Cu-BTC using ferromagnetic and antiferromagnetic description of electron spin states.

Assuming Ferromagnetic Spin Ordering		**Assuming Antiferromagnetic Spin Ordering**	
DDEC Charges		**DDEC Charges**	
Element	Charge [electrons]	Element	Charge [electrons]
C1	0.694	C1	0.691
C2	-0.170	C2	-0.164
C3	0.034	C3	0.031
Cu1	0.938	Cu1	0.920
H1	0.115	H1	0.117
O1	-0.571	O1	-0.567

The electron density was successfully computed for about 75% of the structures in the starting dataset. Of the calculations that did not converge in VASP, about half exceeded the maximum virtual memory imposed by our computing resources, and most of these calculations were for the largest CoRE MOF structures, with primitive cells of several hundred atoms or more. The remaining calculations failed due to other VASP errors including issues with k-point grid density requirements and unresolved segmentation

The content of this chapter has been published: D. Nazarian, J. S. Camp and D. S. Sholl, Chem Mater, 2016, 28, 785-793.

faults. We intend to address the structures for which our calculations to date have been unsuccessful in ongoing work and will update information in the publically available CoRE MOF database as this happens.

The converged electron densities from VASP were used as inputs to the January 2014 version of the Density Derived Electrostatic and Chemical (DDEC) charge assignment code distributed by Manz et al.[10, 41, 42] Atomic point charges were successfully calculated for 2,932 structures. All charges below are reported in units of electron charge. A small number of these structures (14 MOFs, including 9 with silver atoms) were assigned unphysical negative charges to cationic metal centers. These MOFs were found to be missing bound solvent atoms in close proximity to metal centers that were removed in the construction of the CoRE MOF database. In these cases, restoring the bound solvent molecules to their crystallographically refined positions produces realistic positive charges for the cationic metal atoms. We have reported the charges for cationic metal atoms in these structures with and without the bound solvent (Table 4.2.) To remain consistent with the structures in the current CoRE MOF Database, we excluded these 14 structures from further analysis.

The content of this chapter has been published: D. Nazarian, J. S. Camp and D. S. Sholl, Chem Mater, 2016, 28, 785-793.

Table 4.2: charges for cationic metal atoms in these structures with and without the bound solvent.

CORE Ref Code	Metal	DDEC Charge (e)	EQEQ Charge (e)
AVEMOE_clean	Ag	-0.368926	0.37611
AVEMOE_clean	Ag	-0.103077	0.393983
FIMNIA_clean	Ag	-0.268466	0.279505
HIFTUM_clean	Fe	-0.506587	0.643316
INIQUR_clean	Fe	-0.473054	0.658835
INIRAY_clean	Co	-0.453642	0.774718
IPIFAP_clean	Ag	-0.189343	0.429748
JAVWUY_clean	Ag	-0.254777	0.463942
MIHBAG_clean	Mn	-0.487654	0.910316
NEGGOX_clean	Mn	-0.170156	0.315024
OFUSAL_clean	Ag	-0.289736	0.482407
OFUSEP_clean	Ag	-0.285048	0.392976
OFUSEP_clean	Ag	-0.172895	0.378415
OFUSEP_clean	Ag	-0.107346	0.451723
OMAWOP_clean	Ag	-0.205843	0.347537
VEDVUW_clean	Ag	-0.280406	0.3464
VIGNOQ_clean	Ag	-0.236074	0.0741267

The content of this chapter has been published: D. Nazarian, J. S. Camp and D. S. Sholl, Chem Mater, 2016, 28, 785-793.

4.3 Creating a Publically Available Database of Point Charges

Our dataset of structures with DDEC derived atomic point charges constitute a chemically diverse collection of organometallic MOFs featuring 10 different alkali and alkaline earth elements, 32 transition metals, and 15 rare earth metals. The modified cif files with associated DDEC point charges for the nearly 3,000 structures in our dataset can be found at http://dx.doi.org/10.11578/1118280. We anticipate that the publically available dataset of DDEC derived atomic point charges will extend the use of the CoRE MOF structures to answer a range of interesting questions concerning adsorption and diffusion of polar adsorbates in MOFs.

4.4 Group Coordination Point Charge Assignment

In the over 2,000 in the database of MOFs with multiple charges, some structural motifs are represented many times. For example, there are 109 structures with a zinc metal atom coordinated to 4 oxygen atoms. This affords the opportunity to investigate whether the point charge on a given metal can be accurately estimated from the metal's coordination environment. Good agreement between charges on metals of a given coordination environment could facilitate the development of a transferable set of charges applicable to any new MOF with known bonding connectivity. This approach was proposed by Xu et al., who called it the "connectivity-based atom contribution" (CBAC) method.[30] Xu and coworkers performed ab-initio charge assignment on clusters derived from a training set of 30 different MOF structures. From this sample, they suggested generalized charges for the 6 different metal types shown in Table 15.3and several non-metallic groups based on nearest neighbor connectivity. For example, CBAC assigns Zn atoms coordinated to 4 O

The content of this chapter has been published: D. Nazarian, J. S. Camp and D. S. Sholl, Chem Mater, 2016, 28, 785-793.

atoms a charge of 1.583 in any structure. Xu and coworkers found that the CBAC charges inferred from the training set of 30 MOFs agreed well with a test set of 13 other MOFs.[30]

To test the CBAC approach, we "typed" metal atoms by finding the chemically and electronically distinct atomic species within each of the 2,234 unique MOFs in our dataset. This procedure identifies situations in which slightly different charges were assigned to symmetry related, chemical identically copies of atoms within a given MOF structure. For example, our DDEC calculation assigned six chemically identical Zn atoms in ZIF-8 (CoRE MOF database: OFERUN02_clean) atomic point charges ranging from 0.7502 to 0.7622 electrons. The distinct types of metal atoms in each MOF were enumerated by grouping metals with the same bonding neighbors and charge differences of less than 0.05 electrons. Bonds between metals and other atoms were found using the Cambridge Structural Database covalent radii and skin distance parameters.[47] This algorithm returned a single metal atom type within ZIF-8, which we denote "ZnN_4" because the Zn atoms are coordinated to 4 N atoms with a DDEC charge of 0.765±0.008 electrons. To give one more example, in the MFU-4 structure, (CoRE MOF database: IGOCOX_clean) there are two distinct types of Zn atoms. MFU-4 contains ZnN_6 atoms with a Zn charge of 0.370±0.005 electrons and ZnN_3Cl atoms (zinc coordinated to 3 N and 1 Cl) with a Zn charge of 0.63±0.01 electrons.

After typing the metal atoms in this way, the charges on the same types of metals were compared across the 2,234 unique MOF in our dataset. Table 5.3 shows the mean and standard deviation of our DDEC derived atomic point charges on the six different metal types represented in the CBAC report by Xu et al.[30] Overall, the agreement between this work and the CBAC charges is at best moderate. The most numerous metal type in our

dataset was ZnO_4, which range in charge between 0.99 and 1.28 electrons compared to 1.583 in the CBAC dataset. The disagreement between DDEC derived charges on ZnO_4 and CBAC most likely results from the different charge assignment methods used in the two sets of calculations. The range of values observed in our results is more important, since it indicates that using a single value to represent this environment in all structures can potentially miss important information about the local charge arrangement. This difficulty is also seen in the other metal types described by CBAC, particularly CoN_4 and CrO_6, where our DDEC results show a range of 0.22-1.05 and 1.18-1.85 electrons, respectively.

Table 4.3 Distribution of DDEC derived atomic point charges for metals represented in the CBAC dataset.[1]

Metal type	CBAC charge	# in this dataset	Charges in this dataset	Range of charges
ZnO_4	1.583	109	1.09 ± 0.07	0.99 - 1.28
ZnN_4	0.787	19	0.81 ± 0.07	0.55 - 0.87
CuO_4	1.065	25	1.07 ± 0.09	0.88 - 1.37
CoN_4	0.700	15	0.71 ± 0.25	0.22 - 1.05
CoO_5	1.529	15	1.12 ± 0.07	0.99 - 1.23
CrO_6	2.310	8	1.61 ± 0.22	1.18 - 1.85

Figure 4.1 shows the distribution of charges on the 310 instances of Cu metal atoms in our dataset. These 310 Cu atoms have 62 distinct coordination environments (using the nearest neighbor definition given above), which demonstrates the great structural diversity found in MOFs. Many Cu atom types are represented only once, which would make

The content of this chapter has been published: D. Nazarian, J. S. Camp and D. S. Sholl, Chem Mater, 2016, 28, 785-793.

construction of a comprehensive set of transferrable charges difficult. The most numerous copper atom type in our dataset is CuO_6, with 52 instances in our dataset and charges with large variability (0.05 to 2.89). The CuO_4 metals range in charge range from 0.88 to 1.37.

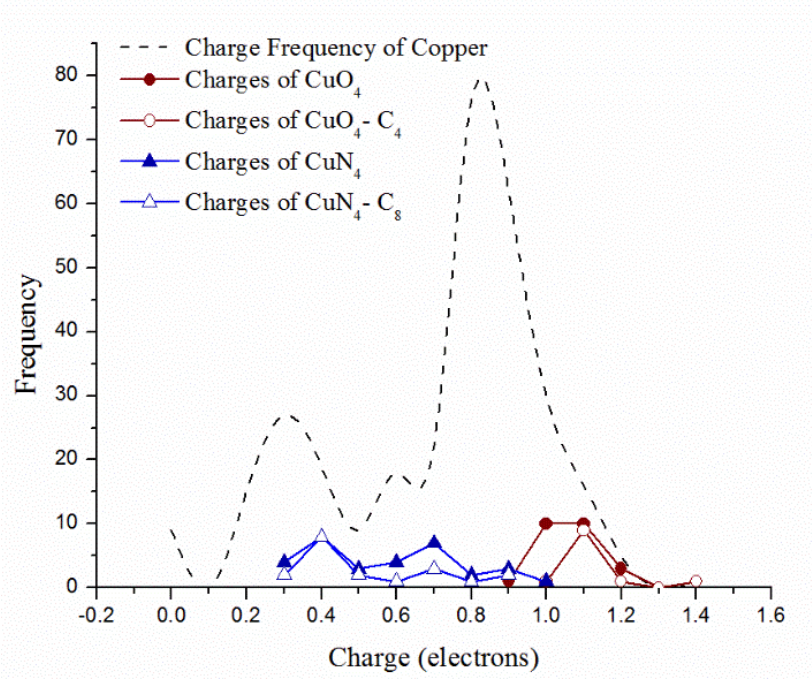

Figure 4.1: Frequency of charges for 310 Cu metal atoms with 62 distinct coordination environments. The distribution of charges the for CuO4 and CuN4 coordination environments are shown in blue and red, respectively.

The 25 instances of Cu atoms in the CuO_4 coordination environment may be subcategorized by the identity of their second nearest neighbor atoms. The most numerous of these is CuO_4-C_4, which denotes Cu atoms coordinated to 4 oxygen atoms, each of which

The content of this chapter has been published: D. Nazarian, J. S. Camp and D. S. Sholl, Chem Mater, 2016, 28, 785-793.

are bonded to 4 carbon atoms. A slightly narrower distribution of charges is observed the CuO_4-C_4 subtype relative to CuO_4, but there is still a wide range. Overall, our results indicate that CBAC-like approaches that define a single point charge for atoms based on the identity of their neighboring atoms are unlikely to be robust for screening of large MOF databases because of the wide range of possible coordination environments and the wide distribution of charges on metal atoms on a given coordination environment.

4.5 Comparison of DDEC to EQeq Point Charges

The extended charge equilibration (EQeq)[12] and periodic charge equilibration (PQeq)[31] methods are computationally efficient extensions of the semi-empirical charge equilibration (Qeq) method to periodic structures.[43] PQeq was previously used to assign point charges to hundreds of experimentally synthesized MOFs to screen for CO_2 adsorption properties.[11] The EQeq method has been used to assign point charges to a database of over 137,000 hypothetical MOFs.[44] To evaluate the accuracy of these methods, we compared the EQeq charges to DDEC charges for each MOF in our dataset. EQeq charges were computed with the standalone code distributed by NuMat Technologies using default metallic oxidation states.[12] This standalone code was found produce charges consistent with the EQeq equilibration method implemented in RASPA 1.0.[32]

Figure 5.2 shows the comparison between DDEC and EQeq for each of the over 10,000 distinct metal atoms in our dataset. A small number of neodymium and uranium metals with unrealistically large (greater than 4) EQeq charges are excluded from this plot.

The content of this chapter has been published: D. Nazarian, J. S. Camp and D. S. Sholl, Chem Mater, 2016, 28, 785-793.

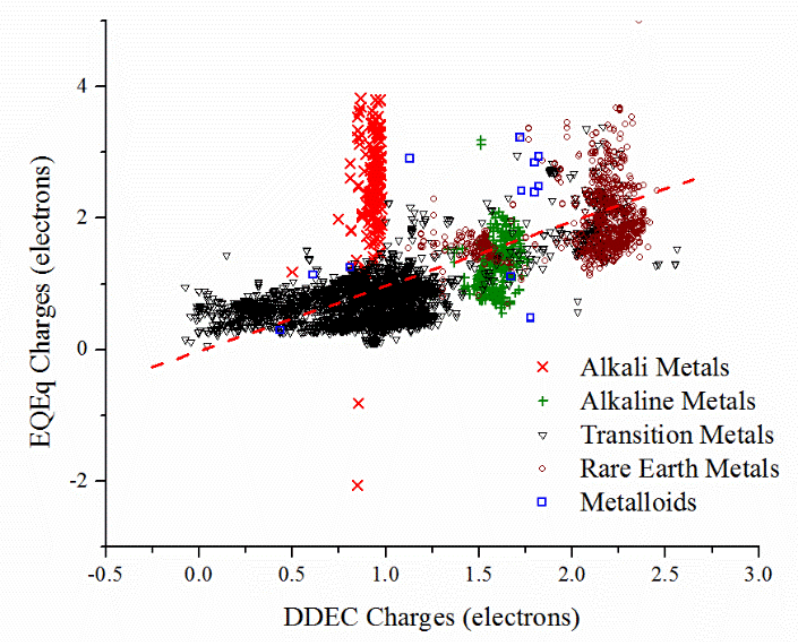

Figure 4.2: Charges from EQeq charge equilibration com-pared to DDEC derived charges for over 10,000 distinct metal atoms in MOFs. Rare earth metals include lanthanides and actinides.

Figure 5.2 shows that EQeq predicts higher charges for metals than DDEC on average. This observation has previously been made by Haldoupis et al.[11] EQeq predicts highly unrealistic charges for many structures containing alkali metals. While DDEC charges for alkali metals cluster around the +1 oxidation expected from their position on the periodic table, EQeq predicts a range of alkali charges from -2 to +4 electrons. Table 4.4 lists a number of statistics assessing charge differences between EQeq and DDEC.

The content of this chapter has been published: D. Nazarian, J. S. Camp and D. S. Sholl, Chem Mater, 2016, 28, 785-793.

Table 4. 1: Statistics assessing charge differences between EQeq and DDEC.

	Mean Absolute Deviation	**Maximum Absolute Deviation**
Alkali	1.67	2.96
Alkaline	0.37	1.67
Transition	0.35	1.45
Rare earth	0.41	1.6
Metalloid	0.67	1.77

In Chapter 5 we will discuss using DDEC point charges to calculate adsorption properties of tert-butyl mercaptan (TBM) and methane in a high-throughput screening study. When used for studying selectivity of TBM, we found that using EQeq charges instead of DDEC charges can have a significant influence on the results of GCMC simulation of adsorption. In many cases EQeq charges give significantly different selectivities of the larger and polar TBM over CH_4 in the Henry's regime compared to DDEC charges. This is both true for alkali metals (Figure 4.3) and for randomly selected MOFs with selectivity of varying order of magnitude (Figure 4.4).

The content of this chapter has been published: D. Nazarian, J. S. Camp and D. S. Sholl, Chem Mater, 2016, 28, 785-793.

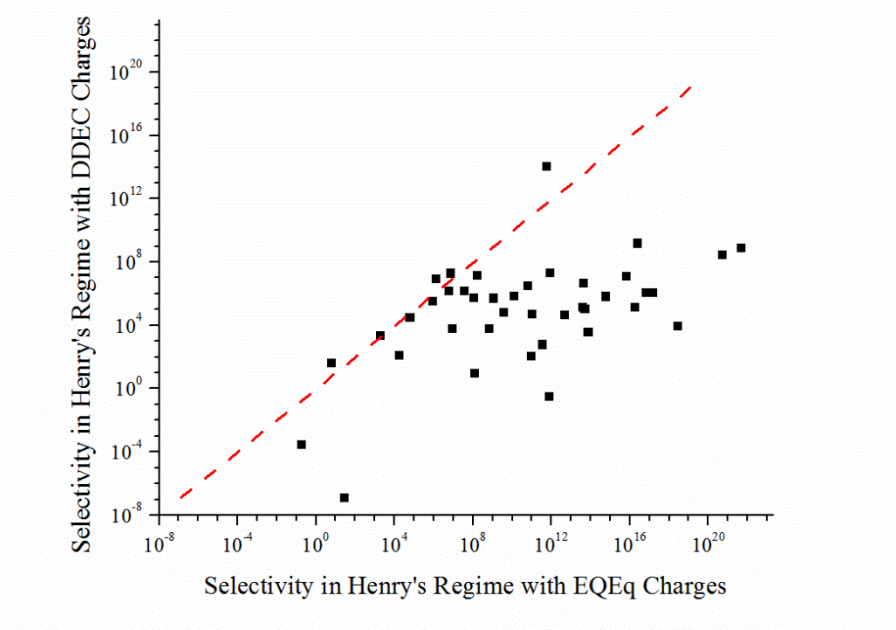

Figure 4.3: Henry's regime selectivity of TBM over methane predicted using DDEC charges vs EQEq charges for MOFs with alkali metal centers

These differences, however, are less pronounced for binary GCMC at the TBM and CH_4 concentrations found in natural gas. Calculation of selectivity for TBM and CH_4 will be discussed in more detail in Chapter 6.

The content of this chapter has been published: D. Nazarian, J. S. Camp and D. S. Sholl, Chem Mater, 2016, 28, 785-793.

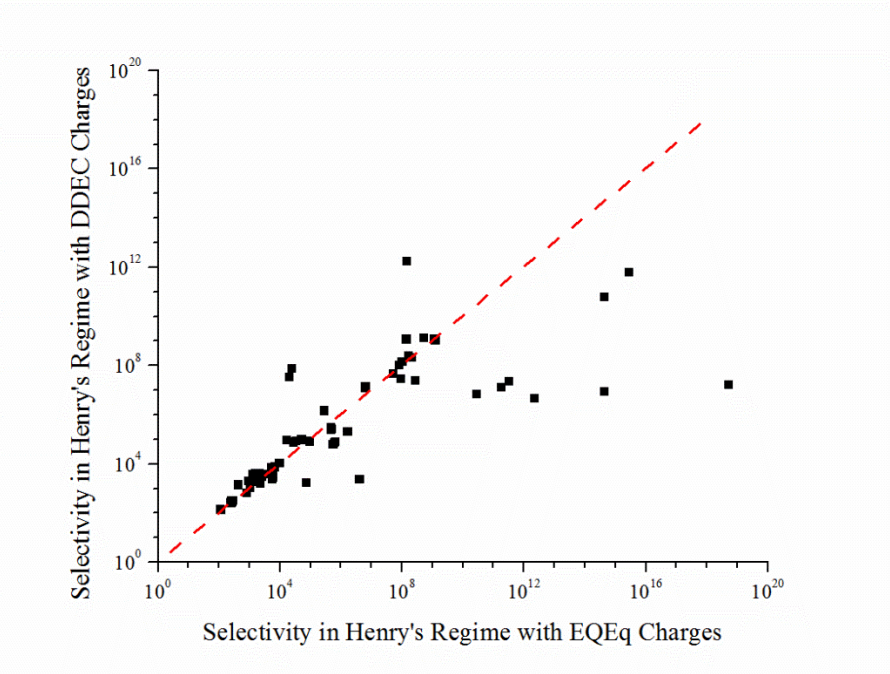

Figure 4.4: Henry's regime selectivity of TBM over methane predicted using DDEC charges vs EQEq charges for randomly selected MOFs with selectivity of varying order of magnitude.

4.6 Conclusions

In this chapter, we have produced a set of high quality point charges for nearly 3,000 experimentally synthesized MOF structures using plane wave DFT calculations and the DDEC charge partitioning method. By using a periodic representation of each MOF, these charges avoid problem of ambiguous bond termination inherent in cluster based methods. Because the DDEC method was designed in part to accurately reproduce the electrostatic potential energy surface for locations outside the van der Waals radius of

The content of this chapter has been published: D. Nazarian, J. S. Camp and D. S. Sholl, Chem Mater, 2016, 28, 785-793.

atoms in the material, our dataset of charges is well suited for modeling adsorption in MOFs.

We have compared the CBAC charge assignment approach, which was developed and tested for approximately 30 MOFs, to thousands of point charges predicted based on structure specific DFT calculations. Our results indicate that CBAC charges may not be robust for screening a large MOF database. We have also demonstrated that charges assigned by the semi-empirical EQeq method can differ drastically from charges calculated with the DDEC method. These discrepancies in point charges can impact the calculated adsorption selectivities for the sample adsorbate, making the case that whenever possible using charges directly determined from electronic structure calculations such as the ones we have used is preferable to semi-empirical approaches.

In all of the calculations we have reported here, charges have been assigned using electronic structure calculations with the experimentally reported crystal structures. Previous calculations have shown that the variation in point charges associated with relaxing crystal structures using DFT[39] or including MOF flexibility using ab initio MD is small[21]. These observations suggest that the charges we have reported will be useful in a wide range of calculations, not only those that assume that the crystal structure of a MOF is fixed in its reported crystal structure.

The content of this chapter has been published: D. Nazarian, J. S. Camp and D. S. Sholl, Chem Mater, 2016, 28, 785-793.

4.7 References

1. L. Grajciar, A. D. Wiersum, P. L. Llewellyn, J. S. Chang and P. Nachtigall, *Journal of Physical Chemistry C*, 2011, 115, 17925-17933.

2. R. Krishna and J. M. van Baten, *Physical Chemistry Chemical Physics*, 2011, 13, 10593-10616.

3. L. C. Lin, A. H. Berger, R. L. Martin, J. Kim, J. A. Swisher, K. Jariwala, C. H. Rycroft, A. S. Bhown, M. W. Deem, M. Haranczyk and B. Smit, *Nat Mater*, 2012, 11, 633-641.

4. A. O. Yazaydin, R. Q. Snurr, T. H. Park, K. Koh, J. Liu, M. D. LeVan, A. I. Benin, P. Jakubczak, M. Lanuza, D. B. Galloway, J. J. Low and R. R. Willis, *Journal of the American Chemical Society*, 2009, 131, 18198–18199.

5. J. G. McDaniel, S. Li, E. Tylianakis, R. Q. Snurr and J. R. Schmidt, *Journal of Physical Chemistry C*, 2015, 119, 3143-3152.

6. T. Van Heest, S. Teich-McGoldrick, J. Greathouse, M. Allendorf and D. Sholl, *Journal of Physical Chemistry C*, 2012, 116, 13183-13195.

7. E. Haldoupis, J. Borycz, H. Shi, K. D. Vogiatzis, P. Bai, W. L. Queen, L. Gagliardi and J. I. Siepmann, *The Journal of Physical Chemistry C*, 2015, 119, 16058-16071.

8. A. Kulkarni and D. S. Sholl, *Langmuir*, 2015.

9. H. Fang, H. Demir, P. Kamakoti and D. S. Sholl, *Journal of Materials Chemistry A*, 2014, 2, 274-291.

10. T. A. Manz and D. S. Sholl, *Abstracts of Papers of the American Chemical Society*, 2010, 240.

The content of this chapter has been published: D. Nazarian, J. S. Camp and D. S. Sholl, Chem Mater, 2016, 28, 785-793.

11. E. Haldoupis, S. Nair and D. Sholl, *Journal of the American Chemical Society*, 2012, 134, 4313-4323.

12. C. E. Wilmer, K. C. Kim and R. Q. Snurr, *J Phys Chem Lett*, 2012, 3, 2506-2511.

13. S. Hamad, S. R. G. Balestra, R. Bueno-Perez, S. Calero and A. R. Ruiz-Salvador, *J Solid State Chem*, 2015, 223, 144-151.

14. C. M. Breneman and K. B. Wiberg, *Journal of Computational Chemistry*, 1990, 11, 361-373.

15. A. V. Marenich, S. V. Jerome, C. J. Cramer and D. G. Truhlar, *Journal of Chemical Theory and Computation*, 2012, 8, 527-541.

16. R. Babarao and J. W. Jiang, *Energy & Environmental Science*, 2008, 1, 139-143.

17. C. Zheng, D. Liu, Q. Yang, C. Zhong and J. Mi, *Industrial & Engineering Chemistry Research*, 2009, 48, 10479-10484.

18. C. Campana, B. Mussard and T. K. Woo, *Journal of Chemical Theory and Computation*, 2009, 5, 2866-2878.

19. S. Keskin, J. Liu, R. B. Rankin, J. K. Johnson and D. S. Sholl, *Industrial & Engineering Chemistry Research*, 2009, 48, 2355-2371.

20. T. A. Manz and D. S. Sholl, *Journal of Chemical Theory and Computation*, 2012, 8, 2844-2867.

21. T. Watanabe and D. S. Sholl, *Langmuir*, 2012, 28, 14114-14128.

22. J. G. McDaniel, K. Yu and J. Schmidt, *The Journal of Physical Chemistry C*, 2012, 116, 1892-1903.

23. T. Watanabe, T. A. Manz and D. S. Sholl, *The Journal of Physical Chemistry C*, 2011, 115, 4824-4836.

The content of this chapter has been published: D. Nazarian, J. S. Camp and D. S. Sholl, Chem Mater, 2016, 28, 785-793.

24. J. G. McDaniel and J. Schmidt, *The Journal of Physical Chemistry C*, 2012, 116, 14031-14039.

25. Y. G. Chung, J. Camp, M. Haranczyk, B. J. Sikora, W. Bury, V. Krungleviciute, T. Yildirim, O. K. Farha, D. S. Sholl and R. Q. Snurr, *Chem Mater*, 2014, 26, 6185-6192.

26. F. H. Allen, *Acta Crystallogr B*, 2002, 58, 380-388.

27. C. M. Simon, J. Kim, D. A. Gomez-Gualdron, J. S. Camp, Y. G. Chung, R. L. Martin, R. Mercado, M. W. Deem, D. Gunter and M. Haranczyk, *Energy & Environmental Science*, 2015, 8, 1190-1199.

28. H. Zhang, P. Deria, O. K. Farha, J. T. Hupp and R. Q. Snurr, *Energy & Environmental Science*, 2015, 8, 1501-1510.

29. X. Nie, A. Kulkarni and D. S. Sholl, *The Journal of Physical Chemistry Letters*, 2015, 6, 1586-1591.

30. Q. Xu and C. Zhong, *Journal of Physical Chemistry C*, 2010, 114, 5035-5042.

31. S. Ramachandran, T. Lenz, W. Skiff and A. Rappe, *Journal of Physical Chemistry*, 1996, 100, 5898-5907.

32. D. Dubbeldam, S. Calero, D. E. Ellis and R. Q. Snurr, *Molecular Simulation*, 2015, DOI: 10.1080/08927022.2015.1010082, 1-21.

33. S. P. Ong, W. D. Richards, A. Jain, G. Hautier, M. Kocher, S. Cholia, D. Gunter, V. L. Chevrier, K. A. Persson and G. Ceder, *Computational Materials Science*, 2013, 68, 314-319.

34. P. JONES, *Chemical Society Reviews*, 1984, 13, 157-172.

35. G. Kresse and J. Furthmuller, *Phys Rev B*, 1996, 54, 11169-11186.

36. D. Nazarian, P. Ganesh and D. S. Sholl, *J Mater Chem A*, 2015, 3, 22432-22440.

The content of this chapter has been published: D. Nazarian, J. S. Camp and D. S. Sholl, Chem Mater, 2016, 28, 785-793.

37. A. Jain, G. Hautier, C. J. Moore, S. P. Ong, C. C. Fischer, T. Mueller, K. A. Persson and G. Ceder, *Computational Materials Science*, 2011, 50, 2295-2310.

38. Y. Cai, A. R. Kulkarni, Y. G. Huang, D. S. Sholl and K. S. Walton, *Cryst Growth Des*, 2014, 14, 6122-6128.

39. T. Watanabe, S. Keskin, S. Nair and D. S. Sholl, *Physical Chemistry Chemical Physics*, 2009, 11, 11389-11394.

40. L. Grajciar, O. Bludsky and P. Nachtigall, *J Phys Chem Lett*, 2010, 1, 3354-3359.

41. T. Manz and D. Sholl, *Journal of Chemical Theory and Computation*, 2012, 8, 2844-2867.

42. T. Watanabe, T. A. Manz and D. S. Sholl, *Journal of Physical Chemistry C*, 2011, 115, 4824-4836.

43. A. K. Rappe and W. A. Goddard, *Journal of Physical Chemistry*, 1991, 95, 3358-3363.

44. C. Wilmer, O. Farha, Y. Bae, J. Hupp and R. Snurr, *Energy & Environmental Science*, 2012, 5, 9849-9856.

The content of this chapter has been published: D. Nazarian, J. S. Camp and D. S. Sholl, Chem Mater, 2016, 28, 785-793.

CHAPTER 5

METAL-ORGANIC FRAMEWORKS FOR REMOVAL OF TERT-BUTYL MERCAPTAN FROM NATURAL GAS

5.1 Introduction

Tert-butyl mercaptan (TBM) is one of the principal gaseous sulfur odorants used in pipeline natural gas for leak detection. Regulations specify that the gas must be detectable at one-fifth of the lower explosive limit of natural gas in air such that the average person can detect odorized natural gas at a maximum of 1% in air.[1] While mercaptans are highly useful for safety reasons, combustion of TBM in natural gas in turbines produces undesirable corrosive compounds. The sulfur present in the natural gas reacts with alkali material in blades of turbines used to generate electricity. This combustion product is a molten reactive residue containing alkaline sulfates which accumulates over turbine rotor blades, nozzle guide vanes, and other hot-section components[2]. Therefore, removing the TBM prior to electricity generation is desirable. Removal of TBM from natural gas fuel streams is traditionally accomplished by a two-step catalytic hydrodesulfurization process.[3] This process is efficient and effective for treating large volumes of gas with long cycle times.[1] However, this process is energy intensive and expensive[5]. Another common method to remove mercaptans is use of activated carbon catalysts to selectively oxidize organosulfur compounds.[6] Unfortunately, the formation of poisonous byproducts such as SO_2 and COS and the need for their removal is a problem.[4,7] A third method for removal mercaptans from natural gas involves selective adsorption on solid adsorbents such as

The content of this chapter has been published: D. Nazarian, J. S. Camp and D. S. Sholl, Chem Mater, 2016, 28, 785-793.

metal oxides, metal-containing zeolites, and metal-containing aluminum oxides. In this method, the sulfur compounds are adsorbed onto the surface by its attraction to the basic surface sites of the adsorbent.[5,8] Selective adsorption can be performed either by a temperature swing or pressure swing adsorption process. Selective adsorption is a promising method for this application but a challenge is determining the appropriate sorbent material with high sulfur capacity and selectivity. Metal Organic Frameworks (MOFs) have high surface areas, pore volumes, and tunability, making them potential sorbents for trace sulfur removal from natural gas. Recently, three common MOFs and zeolite NaY were experimentally tested for use in the selective adsorption of TBM from natural gas.[9] UiO-66(Zr) was found to have promising properties that make it a good candidate material for this application. Below, we use a hierarchical high-throughput screening approach based on grand-canonical Monte Carlo (GCMC) simulations to identify additional MOF materials with high selectivity for TBM over CH_4 and a high saturation capacity for TBM.

As described in Chapter 4, simulations of MOFs often rely on classical force fields (FFs), especially in efforts to examine large numbers of materials.[10-14] In many cases, calculations of this sort are based on generic ("off the shelf") FFs, although increasing progress is being made in developing more reliable FFs for specific classes of materials using data derived from electronic structure calculations.[13,15-17] This parameterization approach has been successful in reproducing experimental adsorbate diffusion coefficients and adsorption isotherms in MOFs.[17] When performing GCMC calculations for non-polar molecules, describing the vdW interactions with generic force fields is sufficient. There exist numerous computational high-throughput screening studies in MOFs for simple,

The content of this chapter has been published: D. Nazarian, J. S. Camp and D. S. Sholl, Chem Mater, 2016, 28, 785-793.

nonpolar adsorbates such as methane[18] and hydrocarbons.[19] However, for more complicated adsorbates, such as TBM, we must describe both the vdW and electrostatic interactions of adsorbate and adsorbent. In essentially all FF calculations with MOFs, Coulombic interactions between atoms in a MOF and also between those atoms and adsorbate molecules are modeled by assigning point charges to each atom of the framework. Haldoupis et al. used the semi-empirical method to assign partial charges to approximately 500 MOFs which were then screened for CO_2/N_2 selectivity.[20] Li et al. used the group coordination CBAC method to assign partial charges to 151 diverse MOFs to calculate CO_2/CH_4 selectivity.[21] McDaniel et al. used DFT calculations along with distributed multipole analysis and charge fragmentation on MOF clusters to assign partial charges to 424 MOFs to ultimately compute CO_2 and CH_4 isotherms.[22]

The MOF DDEC Point Charge database described in Chapter 4 provides point charges calculated using the Density Derived Electrostatic Chemical (DDEC) charges for almost 3,000 MOFs.[23] This is the largest database of partial charges for MOFs to date. This database can be seamlessly used for high-throughput computational screening to study adsorption of TBM in MOFs. As mentioned above, TBM is ubiquitous in pipeline natural gas at ppm levels as an odorant. We know of no previous simulations of TBM adsorption in MOFs. Below, we report on the predicted adsorption properties of TBM and methane in the MOF DDEC Point Charge database. Though there are 2,234 unique MOFs in the dataset, we performed adsorption calculations on all 2,932 MOFs, so these calculations include multiple experimental structures for a number of MOFs.

The content of this chapter has been published: D. Nazarian, J. S. Camp and D. S. Sholl, Chem Mater, 2016, 28, 785-793.

5.2 Methods and Computational Details

A hierarchical high-throughput screening approach using grand-canonical Monte Carlo simulations was used to identify candidate MOF structures for selective adsorption of trace TBM from methane (CH_4). MOFs were evaluated on the basis of selectivity for TBM in the Henry's regime, saturation capacity of TBM, binary selectivity for trace TBM over CH_4, and synthetic and structural properties.

All GCMC simulations of adsorption were performed in the RASPA 1.0 molecular simulation package.[24] The configurational-bias Monte Carlo (CBMC) method was used to model the internal flexibility of TBM molecules as described by the TraPPE force field[25], while CH_4 was modeled a single TraPPE united atom. Dispersion forces between adsorbates and the MOF framework were described by combining Lennard Jones parameters from the Universal Force Field[26] (MOF framework atoms) and TraPPE (adsorbates) with the Lorentz-Berthelot mixing rule. Electrostatic interactions were modeled by using our DDEC derived atomic point charges for MOF framework atoms and TraPPE charges for TBM and CH_4 molecules. All Lennard-Jones interactions were truncated at 16 Å, while all electrostatic interactions were computed pairwise to 16 Å and a long range Ewald summation scheme was used thereafter.

The Henry's constants of TBM and CH_4 were calculated from 5×10^5 Widom particle insertions.[27] The adsorption selectivity in the Henry's regime was defined as the ratio of the single component TBM and CH_4 Henry's constants.[28] The single component saturation capacity of each MOF structure for TBM was calculated by performing GCMC at very high fugacity (5×10^4 bar) using 3×10^4 initialization and 4×10^5 production Monte Carlo cycles. The binary selectivity for TBM over CH_4 was calculated at a composition

The content of this chapter has been published: D. Nazarian, J. S. Camp and D. S. Sholl, Chem Mater, 2016, 28, 785-793.

representative of a natural gas pipeline composition (10 ppm TBM in CH_4) and pressure (18.1 atm) using 2×10^5 initialization cycles and 5×10^5 production cycles. The binary selectivity was defined as

$$\frac{x_{TBM}}{x_{CH_4}}\frac{y_{CH_4}}{y_{TBM}} \tag{5.1}$$

where *x* and *y* are the concentrations in the adsorbed phase and vapor phase, respectively.[9] Pipeline natural gas can contain a range of other species at low concentrations[19], including low molecular weight hydrocarbons and CO_2; these components have not been considered in our screening calculations.

In this work we have not considered reactive dissociation of TBM or similar thiols. While there are a significant number of structures with methanol solvent molecules (33 instances) and bound methoxide solvents (19 instances) in the CoRE MOF database, there are no structures with free methanethiol and only one structure with a methanethiolate anion (CSD: EMEGEJ). One of the structures with a methoxide bound solvent (CSD: BIJDUV) was reported by Zhu et al. for use in sulfoxidation reactions, but this example does not involve a dissociation reaction.[29] DFT studies of adsorptive dissociation of methanethiol in MOFs are possible but are beyond the scope of this work.[30]

The content of this chapter has been published: D. Nazarian, J. S. Camp and D. S. Sholl, Chem Mater, 2016, 28, 785-793.

5.3 Results and Discussion

5.3.1 Selectivity and Heat of Adsorption in Henry's Regime

First, we calculated the Henry's constant and isosteric heats of adsorption of CH_4 and TBM in each structure in the dataset. These quantities are computationally inexpensive to compute for large numbers of materials using Widom insertions in RASPA. The Henry's regime selectivity in each MOF was defined as the ratio of the TBM and CH_4 Henry constants, where values above 1 indicate preferential adsorption of TBM in the Henry regime. About a quarter of structures exhibited very low Henry regime selectivities (less than 10^{-12}) and were excluded from further analysis. Most of these structures have largest cavity diameter (LCD) less than 4.5 Å, indicating nanopores too small to accommodate a TBM molecule. Even excluding these structures, our results have MOFs than span an enormous range of selectivities. Figure 5.1 shows the Henry regime selectivities for the remaining structures plotted as a function of the largest cavity diameter and TBM isosteric heat of adsorption.

The content of this chapter has been published: D. Nazarian, J. S. Camp and D. S. Sholl, Chem Mater, 2016, 28, 785-793.

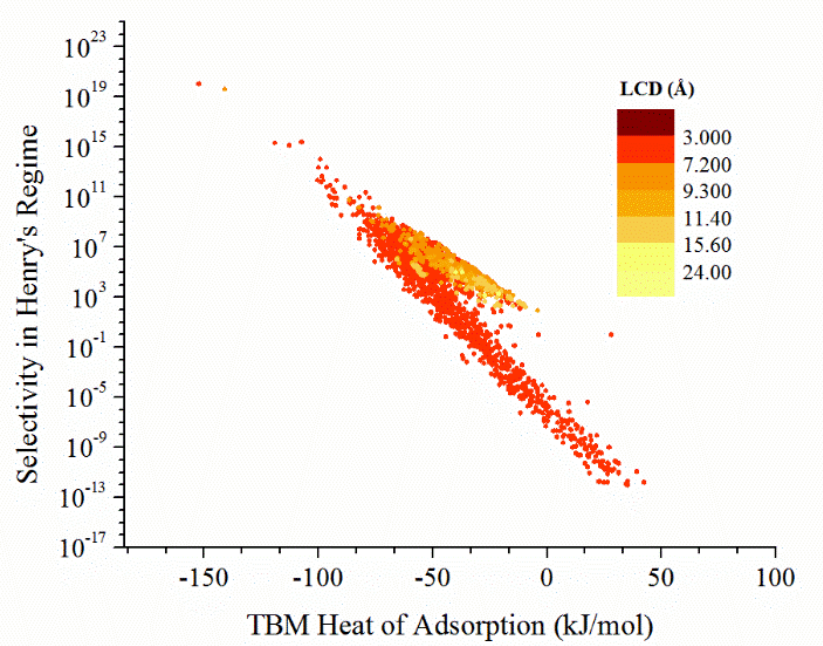

Figure 5.1: Henry's regime selectivity versus TBM heat of adsorption, where negative heats indicate energetically favorable adsorption. Lighter colored data points are associated with structures with larger LCDs.

The results in Figure 5.1 allow a relatively simple description of the competing effects that control selective adsorption of TBM relative to CH_4. Structures with very small pores cannot easily accommodate TBM molecules but readily adsorb CH_4, leading to Henry's regime selectivities less than 1 and positive TBM heats of adsorption. For materials with slightly larger pores (LCD ~5-6 Å), steric repulsive forces become less important relative to energetically favorable electrostatic and dispersive forces. This regime is associated with negative heats of adsorption for TBM and high Henry's regime selectivities for TBM over CH_4. The lowest TBM heats of adsorption (less than -70 kJ/mol) are associated with LCDs of 6-6.5 Å. In structures with LCDs in this range, the TBM

The content of this chapter has been published: D. Nazarian, J. S. Camp and D. S. Sholl, Chem Mater, 2016, 28, 785-793.

molecules fit readily into the largest pore within each MOF. Although these MOFs exhibit very high Henry's regime selectivities ($> 10^8$), the adsorption of TBM is likely irreversible within these materials and access of TBM into the pores may be subject to severe kinetic limitations. At LCDs over 8 Å, TBM molecules experience somewhat weaker energetic interactions with nearby MOF framework atoms, although these interactions are still typically considerably stronger than for CH_4. The structures with the largest LCDs (over 20 Å) have relatively modest Henry's regime selectivities ($< 10^4$).

5.3.2 Henry's regime vs. pipeline conditions

The correlation between these Henry's regime selectivities and selectivities computed from binary GCMC calculations at a representative pipeline composition of natural gas (10 ppm TBM in CH_4, 18.1 atm total pressure)[32] was evaluated. Binary GCMC simulations simulate competitive adsorption effects at finite loadings that single component Henry's regime calculations cannot capture. However, these simulations are considerably more computationally expensive than calculations in the Henry's regime. We first performed these binary calculations for a subset of around 100 MOFs with Henry's regime selectivities ranging from 1 to 10^{10}. The 100 MOFs were chosen to represent a range of selectivities for TBM and produced well converged results within 5×10^5 Monte Carlo cycles. Figure 5.2 shows the binary selectivity (Eq. 5.1) as a function of the Henry's regime selectivity for these 100 materials. With the bulk phase condition we considered a binary selectivity of 10^5 corresponds to an equimolar adsorbed mixture of TBM and CH_4.

The content of this chapter has been published: D. Nazarian, J. S. Camp and D. S. Sholl, Chem Mater, 2016, 28, 785-793.

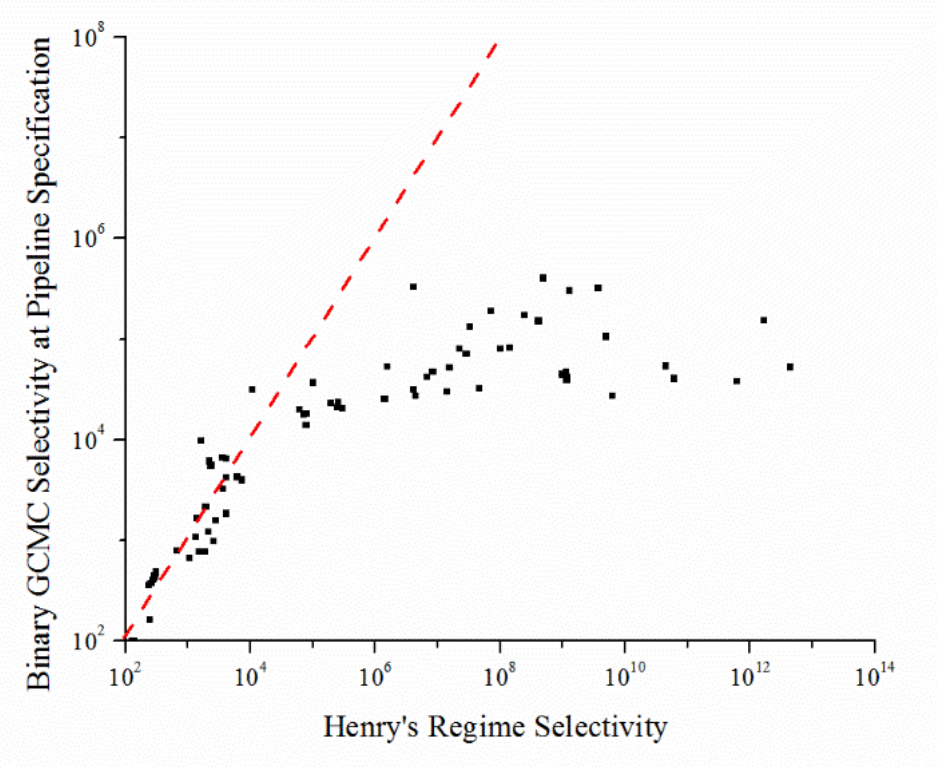

Figure 5.2: Binary GCMC selectivity at a representative pipeline composition of natural gas (10 ppm TBM in CH_4, 18.1 atm) compared to Henry's regime selectivity for 100 MOFs. At values above 10^4, selectivities from binary GCMC deviate significantly from the Henry's regime.

Figure 5.2 shows that when the Henry's regime selectivity is less than ~10^4, the Henry's regime selectivity is strongly correlated with the binary selectivity. For Henry's regime selectivities above ~10^4, the Henry's regime prediction tends to strongly overestimate the binary selectivity. It is challenging to achieve complete numerical convergence in binary GCMC for the most selective materials, and we observed relatively large fluctuations in the observed GCMC selectivity for some structures because of the very small amounts of CH_4 observed. Nevertheless, the uncertainties associated with this effect are small enough to allow us to conclude that the trend shown in Figure 5.2 for high selectivity materials is a physical effect. This effect arises because the TBM adsorption is

The content of this chapter has been published: D. Nazarian, J. S. Camp and D. S. Sholl, Chem Mater, 2016, 28, 785-793.

not accurately described by Henry's law in these highly selective materials under the bulk phase conditions we examined, meaning that the adsorbed amount of TBM is overestimated by using the Henry's regime results. Although this means that using binary GCMC calculations is necessary to quantitatively describe TBM/CH_4 mixture adsorption in the most selective materials we have considered, Figure 5.2 shows that using the Henry's regime selectivity is a useful way to order materials using computationally efficient methods.

5.3.3 Binary GCMC and Saturation Loading

Based on the results above, we narrowed our attention to materials with Henry's regime selectivity higher than 10^3. While MOFs with high selectivity for TBM are desired, MOFs with large TBM heat of adsorption are likely to irreversibly adsorb TBM. To include the feature in our calculations in a simple way, we also eliminated MOFs with a Henry's regime heat of adsorption for TBM more favorable than -70 kJ/mol. We also removed all MOFs containing lanthanide metals from further consideration. For the remaining 1,497 distinct MOFs, we performed calculations to evaluate each material's capacity for TBM and the binary selectivity at the natural gas pipeline conditions defined above. The TBM saturation capacity was calculated using single component GCMC at a fugacity (50 kPa) above the vapor pressure of TBM at 25 °C.[31] As expected, these results correlate strongly with the MOF pore volume. Figure 5.3 shows the saturation TBM loading of each MOF as a function of selectivity at the natural gas pipeline composition calculated using binary GCMC.

We anticipate that top performing MOFs for TBM removal will have a saturation loading for TBM greater than 200 mg/g. We find 354 MOFs that meet this criteria. We

The content of this chapter has been published: D. Nazarian, J. S. Camp and D. S. Sholl, Chem Mater, 2016, 28, 785-793.

reiterate that by virtue of selecting these materials from the CoRE MOF database, every material has a previously reported synthesis and structure. Among these promising candidates are multiple representations of the commonly studied MOFs reported in different experimental reports. Among these common MOFs are MIL-53 and Cu-BTC, which were identified by Chen et al. as highly selective but structurally unstable during TBM adsorption.[9] ZIF-8, a commonly studied and readily available MOF that is stable under humid conditions, is predicted to have a binary selectivity of 1.17×10^4 and saturation loading of approximately 270 mg of TBM per gram of adsorbent. It has been shown in both experiments and using molecular modeling that ZIF-8 can adsorb molecules that are considerably larger than its nominal pore diameter due to flexibility in the small windows that control molecular diffusion in this material.[32-35] These observations lessen concerns that TBM adsorption in ZIF-8 would be limited by kinetic considerations. Other less studied but water stable and promising candidates include BIBXUH, a nickel based MOF with a 691 mg/g capacity for TBM, and MFU-4, a zinc and chlorine based MOF with 6.85×10^5 selectivity for TBM over methane.

The content of this chapter has been published: D. Nazarian, J. S. Camp and D. S. Sholl, Chem Mater, 2016, 28, 785-793.

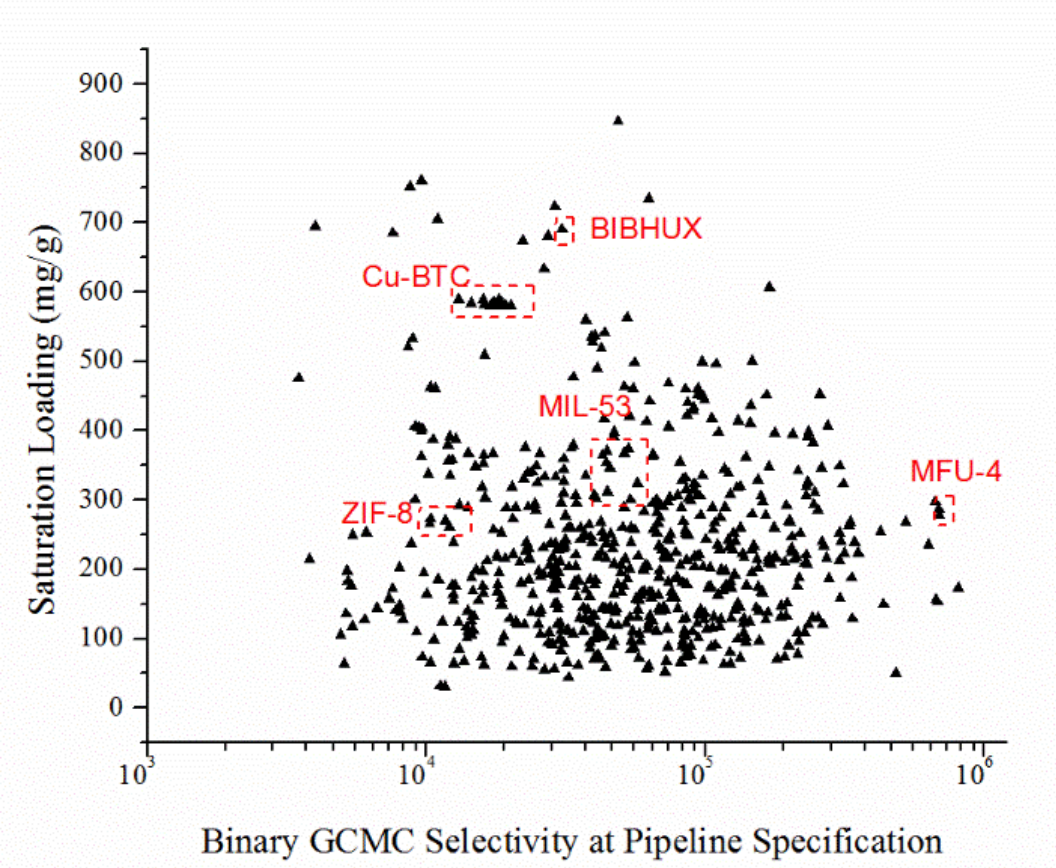

Figure 5.3: TBM/CH4 selectivity at the pipeline composition as a function of saturation loading of TBM in 1497 MOFs. Cu-BTC and MIL-53, two MOFs studied experimentally for TBM adsorption by Chen et al.[9] are highlighted. Three other promising and water stable MOFs are also highlighted.

5.4 Conclusions

We have screened each MOF in the DDEC Point Charge MOF database for potential use in the adsorptive removal of tert-butyl mercaptan from methane. Our efficient screening procedure has identified hundreds of MOFs with high selectivity and capacity for TBM. These results suggest multiple directions for future experimental efforts, including the identification of some well-known materials as potential candidates for this

The content of this chapter has been published: D. Nazarian, J. S. Camp and D. S. Sholl, Chem Mater, 2016, 28, 785-793.

separation. We have not attempted in these screening calculations to pick a single "winning" material for the challenge of selectively adsorbing TBM from CH_4. Finding appropriate materials for practical use must involve considerations that are beyond the scope of our current calculations, including the long term stability of materials, the cost and ease of synthesis of materials and so on. Nevertheless, the observation that our calculations have identified a large number of materials with appealing adsorption selectivities and adsorption capacities for TBM provides a strong basis for continued development of high performance materials for this application.

The high selectivities of MOFs in our study reveal a potential challenge with the application of MOFs for methane storage. In the original CoRE MOF report, MIL-53 was found to have among the highest capacities for methane storage.[36] In our study, we find that MIL-53 is highly selective for TBM and most likely for other polar components of natural gas. This selectivity may drastically reduce methane capacity during cyclic adsorption, especially if TBM accumulates over the many cycles in the life time of the material. Zhang et al. have studied the adsorption and shown the accumulation of ethane, propane and butane in some common MOFs[19], but there has yet to be a study on adsorption impact of trace components such as TBM and other polar species such as H_2O and CO_2 in natural gas.

The content of this chapter has been published: D. Nazarian, J. S. Camp and D. S. Sholl, Chem Mater, 2016, 28, 785-793.

5.5 References

1. Ivanov, I., J. Strmen, and L. Jones, *Pipeline & Gas Journal*, 2009. 236(11): p. 1-4.
2. Casanova, M., *Proceedings of the Second Turbomachinery Symposium*, 1973: p. 83-90.
3. Babich, I.; Moulijn, J., *Fuel* 2003, 82, (6), 607-631.
4. Ratnasamy, C., et al., *Catalysis Today*, 2012. 198(1): p. 233-238.
5. Kang, S.-H., et al., *Energy & Fuels*, 2007. 21(6): p. 3537-3540.
6. Gardner, T.H., et al., *Fuel*, 2002. 81(17): p. 2157-2166.
7. Wu, X.X., et al., *Carbon*, 2005. 43(5): p. 1087-1090.
8. Shen, Y., et al., *Rsc Advances*, 2012. 2(5): p. 1700-1711.
9. Chen, G.; Tan, S.; Koros, W. J.; Jones, C. W., *Energy & Fuels* 2015, 29, (5), 3312-3321.
10. Krishna, R.; van Baten, J. M., *Physical Chemistry Chemical Physics* 2011, 13, (22), 10593-10616.
11. Lin, L.-C.; Berger, A. H.; Martin, R. L.; Kim, J.; Swisher, J. A.; Jariwala, K.; Rycroft, C. H.; Bhown, A. S.; Deem, M. W.; Haranczyk, M., *Nature materials* 2012, 11, (7), 633-641.
12. Yazaydın, A. O; Snurr, R. Q.; Park, T.-H.; Koh, K.; Liu, J.; LeVan, M. D.; Benin, A. I.; Jakubczak, P.; Lanuza, M.; Galloway, D. B., *Journal of the American Chemical Society* 2009, 131, (51), 18198-18199.
13. McDaniel, J. G.; Li, S.; Tylianakis, E.; Snurr, R. Q.; Schmidt, J. R., *The Journal of Physical Chemistry C* 2015, 119, (6), 3143-3152.
14. Van Heest, T.; Teich-McGoldrick, S. L.; Greathouse, J. A.; Allendorf, M. D.; Sholl, D. S., *The Journal of Physical Chemistry C* 2012, 116, (24), 13183-13195.

The content of this chapter has been published: D. Nazarian, J. S. Camp and D. S. Sholl, Chem Mater, 2016, 28, 785-793.

15. Haldoupis, E.; Borycz, J.; Shi, H.; Vogiatzis, K. D.; Bai, P.; Queen, W. L.; Gagliardi, L.; Siepmann, J. I., *The Journal of Physical Chemistry C* 2015, 119, (28), 16058-16071.

16. Kulkarni, A.; Sholl, D. S. *Langmuir* 2015.

17. Fang, H.; Demir, H.; Kamakoti, P.; Sholl, D. S., *Journal of Materials Chemistry A* 2014, 2, (2), 274-291.

18. Simon, C. M.; Kim, J.; Gomez-Gualdron, D. A.; Camp, J. S.; Chung, Y. G.; Martin, R. L.; Mercado, R.; Deem, M. W.; Gunter, D.; Haranczyk, M., *Energy & Environmental Science* 2015, 8, (4), 1190-1199.

19. Zhang, H.; Deria, P.; Farha, O. K.; Hupp, J. T.; Snurr, R. Q., *Energy & Environmental Science* 2015, 8, (5), 1501-1510.

20. Haldoupis, E.; Nair, S.; Sholl, D., *Journal of the American Chemical Society* 2012, 134 (9), 4313-4323.

21. Li, Z. J.; Xiao, G.; Yang, Q. Y.; Xiao, Y. L.; Zhong, C. L., *Chemical Engineering Science* 2014, 120, 59-66;

22. McDaniel, J. G.; Li, S.; Tylianakis, E.; Snurr, R. Q.; Schmidt, J. R., *Journal of Physical Chemistry C* 2015, 119 (6), 3143-3152.

23. Nazarian, D.; Camp, J. S.; Sholl, D. S., *Chem Mater* 2016, 28 (3), 785-793.

24. Dubbeldam, D.; Calero, S.; Ellis, D. E.; Snurr, R. Q., *Molecular Simulation* 2015, 1-21.

25. Lubna, N.; Kamath, G.; Potoff, J. J.; Rai, N.; Siepmann, J. I., *The Journal of Physical Chemistry B* 2005, 109, (50), 24100-24107

26. Rappé, A. K.; Casewit, C. J.; Colwell, K.; Goddard Iii, W.; Skiff, W., *Journal of the American Chemical Society* 1992, 114, (25), 10024-10035.

27. Shing, K.; Gubbins, K., *Molecular Physics* 1981, 43, (3), 717-721.

The content of this chapter has been published: D. Nazarian, J. S. Camp and D. S. Sholl, Chem Mater, 2016, 28, 785-793.

28. Van Heest, T.; Teich-McGoldrick, S. L.; Greathouse, J. A.; Allendorf, M. D.; Sholl, D. S., *The Journal of Physical Chemistry C* 2012, 116, (24), 13183-13195.

29. Zhu, C. F.; Chen, X.; Yang, Z. W.; Du, X.; Liu, Y.; Cui, Y., *Chemical Communications* 2013, 49 (64), 7120-7122

30. Lustemberg, P. G.; Martiarena, M. L.; Martinez, A. E.; Busnengo, H. F., *Langmuir* 2008, 24 (7), 3274-3279.

31. Chen, G.; Lively, R. P.; Jones, C. W.; Koros, W. J., *Industrial & Engineering Chemistry Research* 2014, 53, (17), 7113-7120

32. Aldrich, S. Safety Data Sheet: 2-Methyl-2-propanethiol http://www.sigmaaldrich.com/catalog/product/aldrich/109207 (September 20th, 2015)

33. Verploegh, R.; Nair, S.; Sholl, D. S., *Journal of the American Chemical Society* 2015, Submitted.

34. Zhang, C.; Lively, R. P.; Zhang, K.; Johnson, J. R.; Karvan, O.; Koros, W. J., *The Journal of Physical Chemistry Letters* 2012, 3, (16), 2130-2134.

35. Zhang, K.; Lively, R. P.; Zhang, C.; Chance, R. R.; Koros, W. J.; Sholl, D. S.; Nair, S., *The Journal of Physical Chemistry Letters* 2013, 4, (21), 3618-3622.

36. Chung, Y. G.; Camp, J.; Haranczyk, M.; Sikora, B. J.; Bury, W.; Krungleviciute, V.; Yildirim, T.; Farha, O. K.; Sholl, D. S.; Snurr, R. Q., *Chemistry of Materials* 2014, 26, (21), 6185-6192.

37. Zhang, H.; Deria, P.; Farha, O. K.; Hupp, J. T.; Snurr, R. Q., *Energy & Environmental Science* 2015, 8, (5), 1501-1510.

The content of this chapter has been published: D. Nazarian, J. S. Camp and D. S. Sholl, Chem Mater, 2016, 28, 785-793.

CHAPTER 6

DENSITY FUNCTIONAL THEORY OPTIMIZED DATABASE OF EXPERIMENTALLY DERIVED METAL-ORGANIC FRAMEWORKS

6.1 Introduction

Computational models of metal-organic frameworks (MOFs), especially screening procedures, depend critically on access to accurate MOF structure data typically obtained using single crystal x-ray diffraction (XRD) or x-ray powder diffraction (XRPD). XRD is typically used to determine structure for crystal sizes larger than 5 micrometers and XRPD is used for smaller crystals.[1] More than 90% of the MOF structures found in the Cambridge Structural Database[2] (CSD) were resolved using XRD. These reported structures often include complications such as partially occupied or disordered atoms. This information is crystallographically meaningful but must be removed prior to computer simulations.[3] The Computation-Ready Experimental MOF (CoRE MOF) database of Chung et al.[3] constructed a large set of experimentally refined MOF structures from the CSD by removing solvent molecules and selecting a single representation of any disordered atoms in the reported structures. The CoRE MOF database eliminates an initial hurdle to high-throughput molecular simulations of MOFs and has already been used to screen MOFs in applications such as methane storage[4] and natural gas (including higher hydrocarbons) storage[5].

In their study of methane uptake in the CoRE MOFs, Chung et al. found that there are at least 13 different crystal structures of the commonly studied MIL-53(Al), with significant variation in their simulated methane uptake. The different MIL-53(Al) structures in the database, synthesized independently, have varying experimentally resolved lattice parameters and atomic coordinates (see Figure 6.1).

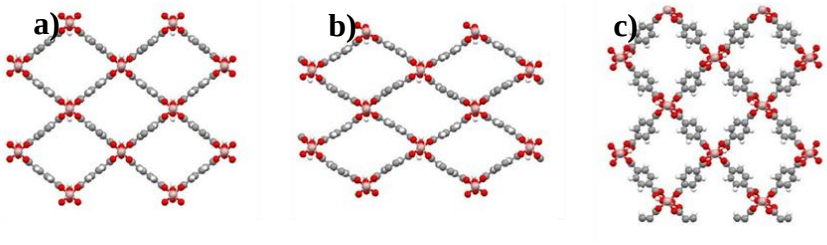

Figure 6.1: Cleaned versions of three MIL-53(Al) structures, (a) WAYMIU[6], (b) SABVOH[7], and (c) HAFQUC[8], found in the CoRE MOF database. The GCMC methane uptake at 65 bar and 298 K for WAYMIU, SABVOH, and HAFQUC are 250, 180, and 270 vol_{STP}/vol of adsorbate per framework, respectively.[3]

The differences in the 13 structures is in part related to the inconsistencies in methods used to obtain crystal structures. Crystal structures are often resolved before activation, with the presence of residual synthesis solvent molecules within the MOF pores. In some cases, the crystal structure data will include the solvent, but in other cases the solvent is not resolved during the structural refinement. Structures resolved with residual solvent within the pores or with solvent molecules bound to the metal centers may adopt a different geometry once solvent is removed. Each MOF in the CoRE MOF database is represented by a structure without solvent. Generating these structures assumed that the structure geometry remains the same after activation.[3]

The quality of diffraction tools and characterization conditions also play a role in the quality of the crystal data obtained experimentally. The choice of diffractometer may affect the data resolution of resulting crystal structures and structures obtained at higher temperatures will include the impact of thermal motion.[1] The uncertainties in crystal structures described may be resolved through systematic energy minimization of the initial geometry to obtain an optimized structure.[9] These efforts typically result in small changes relative to the initial experimental structure, and are defined by Catlow et al. as refinements, not predictions.[10] These authors reserve the phrase "structure prediction" for methods that do not depend on any empirical information about the atom positions of the structure. In a recent review, Catlow et al. provide a comprehensive summary of the current state of the art methods used for crystal structure prediction.[10] In a recent review of computational methods for MOFs, Coudert et al. also summarize such methods.[11] The result of such methods include the database of hypothetical zeolites generated by Deem et al.[12] While such predictive methods are valuable tools for genomic and material discovery efforts, experimental synthesis of many of the predicted materials still remains a challenge.

In this work we are concerned with the CoRE MOF database, which includes only structures with a known and published synthesis procedure. Given an initial experimental structure, we use plane wave Density Functional Theory (DFT) refinement methods to minimize each structure's energy and generate a more accurate structure. DFT calculations are routinely used to determine the ground state structure of MOFs before adsorption and diffusion predictions. Recently we have benchmarked commonly used DFT functionals and demonstrated that DFT methods reliably predict MOF lattice parameters and atomic coordinates (see Chapter 3).[13]

A range of studies have used DFT based calculations to refine and analyze large sets of crystal structures. Sharma et al. conducted a search for novel dielectric polymeric materials by screening 1D repeat units for high dielectric constants using DFT.[14] Chandrasekhar et al. used DFT methods to predict solubility, diffusivity, and permeability of hydrogen in intermetallic membrane materials.[15] Armiento et al. performed a large-scale DFT study of the ABO_3 chemical space in the perovskite crystal structure to identify promising piezoelectric materials.[16] Yan et al. screened hundreds of transition metal oxides for photocatalytic materials for water splitting.[17] Nicholson et al. used DFT-based methods to assess this stability of metal hydride systems by predicting thermodynamic properties.[18] The Materials Project has applied DFT+U methods, using a combination of sophisticated high-throughput infrastructure and crowd-sourcing, to energy minimize thousands of structures obtained from the Inorganic Crystal Structure Database and predict a range of material properties.[19, 20]

Due to the relatively high computational cost of such calculations, DFT based structure refinements of MOFs have previously only been applied when considering only a small number of structures. To date, all high-throughput screening studies of MOFs have used the experimentally observed crystal structures or collections of hypothetical structures generated *in silico*. There have been no systematic attempts to refine the structures of a large and diverse set of MOF structures and study the impact of refinement on predicted properties. The central aim of this work is to produce a large and diverse set of DFT optimized MOF structures, to use this data to evaluate the correctness of the experimentally refined structures currently available, and assess the impact of optimization on adsorption properties of the MOFs. The DFT energy minimized structures in this work are publicly

available at http://dx.doi.org/10.11578/1118280 as a supplement to the CoRE MOF database. As discussed earlier, methane uptake studies of the CoRE MOFs has shown that variations in atomic positions can impact methane uptake.[3] We anticipate that with the availability of DDEC charges for a large database of materials, as discussed in Chapter 4, there will be a shift to screening MOFs for adsorption properties of larger polar molecules.[21] It seems likely that the impact of structure refinement will be more pronounced for adsorption of polar molecules than for simple species like CH_4.

In our previous benchmarking study of DFT functionals for MOFs, we have shown that small changes in MOF structure do not impact DDEC point charges.[13] In this work, we have used our refinement results to consider the impact of large structural changes on predicted DDEC charges.

6.2 Methods and Computational Details

6.2.1 Structure Refinement

All DFT calculations were carried out using the Gaussian plane-wave (GPW) computational package CP2K 2.6[22] on the Argonne National Laboratories supercomputer MIRA. Based on the results of our previous benchmarking study, we chose to use the Gordecker, Teter, Hutter dual-space pseudopotentials (GTH)[23] with the PBE-D3[24, 25] functional. PBE-D3 introduces empirical dispersion corrections to the generalized gradient PBE functional. As described in Chapter 3, the dispersion coefficient used in PBE-D3 are geometry dependent and are adjusted on the basis of the local coordination number around the atoms of interest. After a series of convergence tests, a plane-wave energy cutoff of 800 Ry was chosen. We have used the double-zeta valance polarized (DZVP)[26] basis sets

for all elements except Lanthanum (La). The basis set used for La is provided in Appendix D. Spin polarization was considered for all calculations. Geometry optimization of the system was performed using a BFGS optimizer, allowing for full atomic and cell relaxation, until the largest force on atoms reached less than 0.0003 Hartree/Bohr.

Optimization was attempted for 3,000 MOFs in the CORE MOF database. These structures were chosen based on basis-set availability in the CP2K package. Of the 3,000 structures, calculations for 879 structures converged successfully within a reasonable computation time.

6.2.2 Structure Analysis

The changes in geometry associated with energy minimization were analyzed for each successfully optimized structure. Structural parameters considered include unit cell parameters (a, b, c, α, β, and γ), unit cell volume, helium void fraction, largest cavity diameter (LCD), and pore limiting diameter (PLD). The void fraction was computed using the RASPA 2.0 classical simulation package.[27] The LCD, PLD, and pore size distributions were calculated using the Zeo++ geometry analysis package.[28] Structures were considered significantly different than the original experimental structure if pore descriptors changed by more than 1 Å or volume was changed by more than 10% after refinement.

6.2.3 Methane and CO_2 Adsorption

Classical grand canonical Monte Carlo (GCMC) simulations of methane adsorption were conducted on all optimized structures using the RASPA 2.0 code[29]. Methane adsorption was simulated at 65 bar and 298 K. The Peng Robinson equation of state[30] was used to calculate the fugacity values necessary to impose equilibrium between the system

and the external gas reservoir. Methane-methane and methane-framework interactions were modeled with a Lennard-Jones (LJ) 12-6 potential using the Lorentz-Berthelot mixing rules. The LJ parameters for all framework atoms were obtained from the Universal Force-Field (UFF).[31] The LJ parameters for methane (ε/k_B = 148.0 K; σ = 3.73 Å) were obtained from the TraPPE force-field, modeled as a single sphere with one LJ interaction site.[32] All LJ interaction potentials were truncated at 12.8 Å. To satisfy the minimum image convention all simulation cells were replicated to at least 25.6 Å along each axis. All GCMC simulations included a 2,500-cycle equilibration period followed by a 2,500- cycle production period.[33] GCMC simulations included random insertion, deletion, translation, and re-insertion moves with equal probabilities.

GCMC calculation of CO_2 adsorption were conducted for structures with available charges in the MOF DDEC charge database discussed in Chapter 4. Simulations were performed for 502 structures at 1 bar and 298 K in a similar manner to our methane adsorption calculations. DDEC charges from the experimentally observed structures were directly mapped onto the optimized structures. The LJ parameters for CO_2 were obtained from the TraPPE force-field, modeled as a 3-site molecule as described in Appendix D.[32]

6.2.4 Calculating DDEC Charges After Structural Optimization

For each MOF with significant structural change and available DDEC charges in the MOF DDEC Point Charge database (87 MOFs), a single self-consistent ionic step was attempted in the VASP 5.3.5 plane-wave DFT package[34] to generate the electron and spin density distributions used as inputs for point charge assignment. The Brillouin zone was sampled with a 1000 points per atom density Monkhorst-Pack grid. Spin-polarization was included for all calculation, adopting a ferromagnetic high spin states for magnetic

elements.[19, 35] Point charges were assigned for each atom type in a structure. Atom types were assigned based on the atom's neighboring environment and charges for each atom type are averaged to obtain a net neutral system.

6.3 Results and Discussion

6.3.1 Structure Refinement

To compare the extent and type of geometry change in each MOF structure after energy minimization, we considered charges in four structural parameters: unit cell volume, helium void fraction, unit cell angles, and LCD. As shown in Figure 6.2, a majority of structures show a less than 10% change in unit cell volume and void fraction and 2° change in unit cell angles (α, β, and γ considered) after energy minimization. We also find that most structures experience small changes in pore diameter; more than 90% of structures experience less than 1 Å change in the LCD. We find little correlation between changes in volume and void fraction. While most of structures increase in volume and LCD, many structures decrease in void fraction. Figure 6.3 shows that most structures all in the upper left quadrant with an increase in volume but decrease in void fraction.

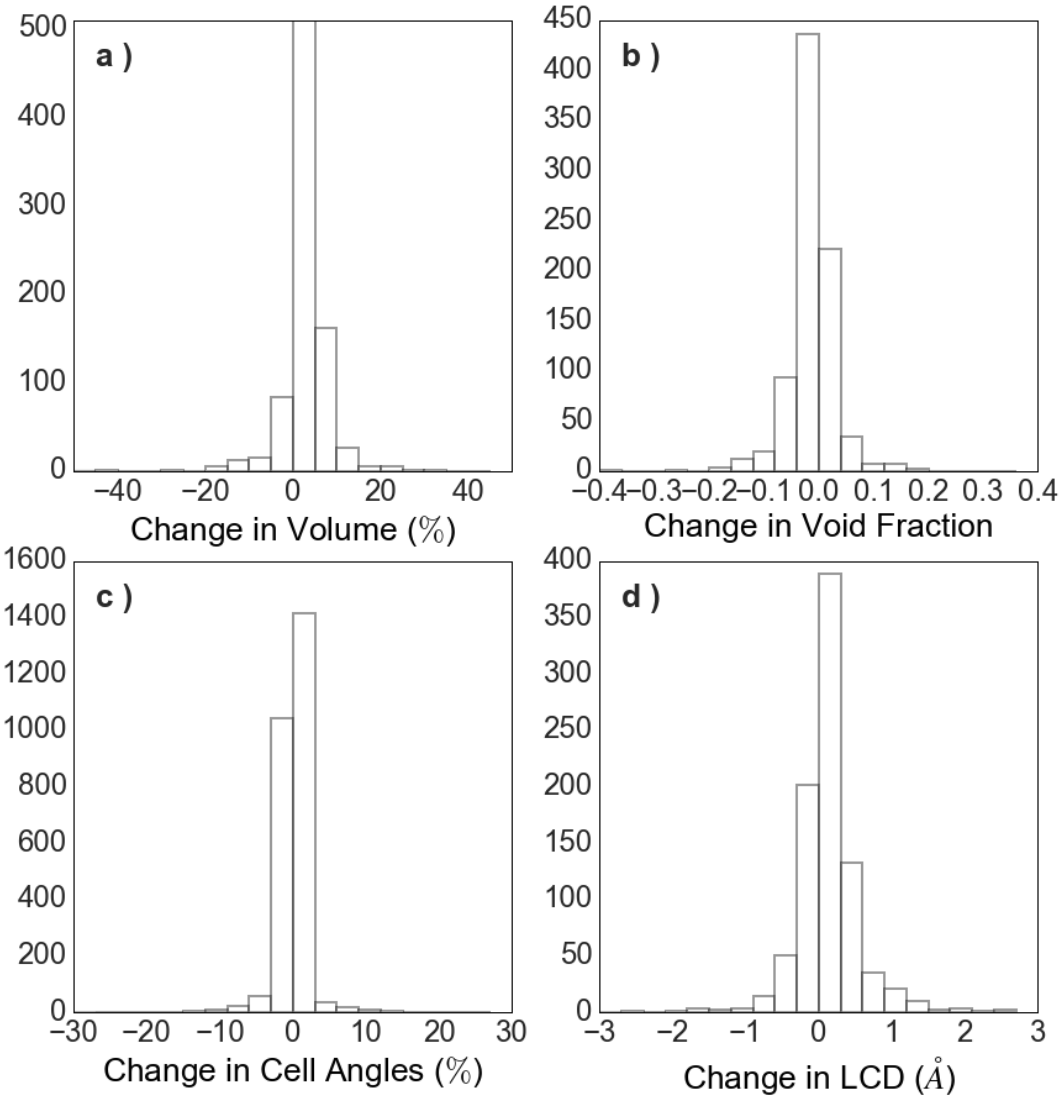

Figure 6.2: Histogram of changes in structural parameters upon DFT energy minimization for 879 structures. The vertical axis in each case is the number of structures. More than 90% of structures showed a less than (a) 10% change in cell volume after optimization, (b) 0.1 change in void fraction, (c) 5% or 2 degree change in cell angle after optimization, (d) 1 Å change in the LCD.

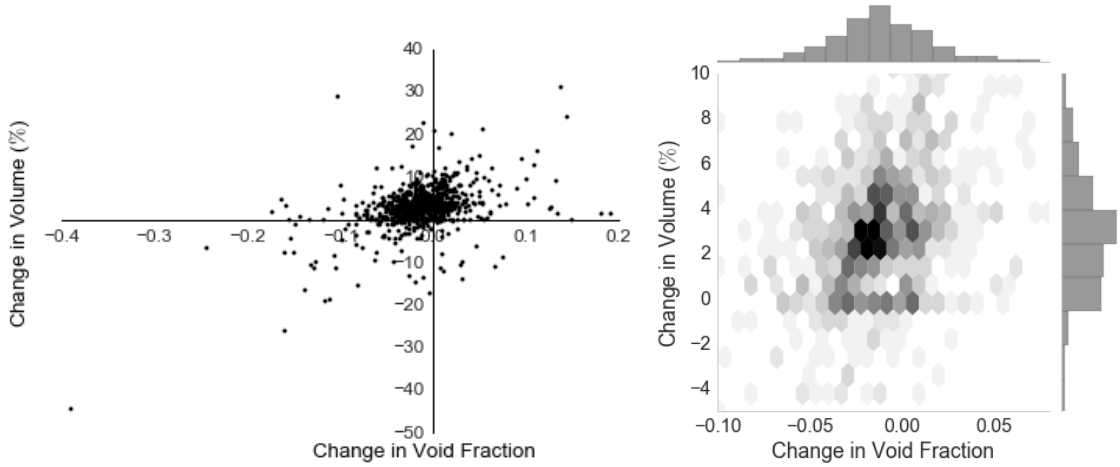

Figure 6.3: Comparison for percent change in cell volume and change in void fraction due to DFT refinement for 879 structures shows a weak correlation between these quantities. A majority of structures experience an increase in volume but a decrease in void fraction. The left figure shows all 879 structures, while the right figure focuses on structures with small change due to optimization.

6.3.2 Impact of Residual Solvent

While most MOFs in the CoRE MOF structures show only small structural changes between their experimental and energy minimized representations, a subset of MOFs exists with substantial changes in their structures after energy minimization. Examination of these materials indicates that this subset is comprised mainly of structures that contained residual solvent in the structure when the original XRD or XRPD was performed. In the process of constructing the CoRE MOF database, Chung et al. identified MOFs with solvent and without solvent in the crystallographic structure information provided in the CSD. We used this information to divide the 879 structures from our DFT calculations into these two categories. When the structural parameters discussed above (overall change in unit cell volume, helium void fraction, unit cell angles, and LCD) are analyzed for each group

separately, we find a stark difference among the groups on the impact of energy minimization on geometry. Figure 6.4 shows a box and whisker diagram for each structural parameter with and without solvent in the CSD version of the structure. Experimental MOF structures which included solvent during structural analysis display a larger number and magnitude of outliers.

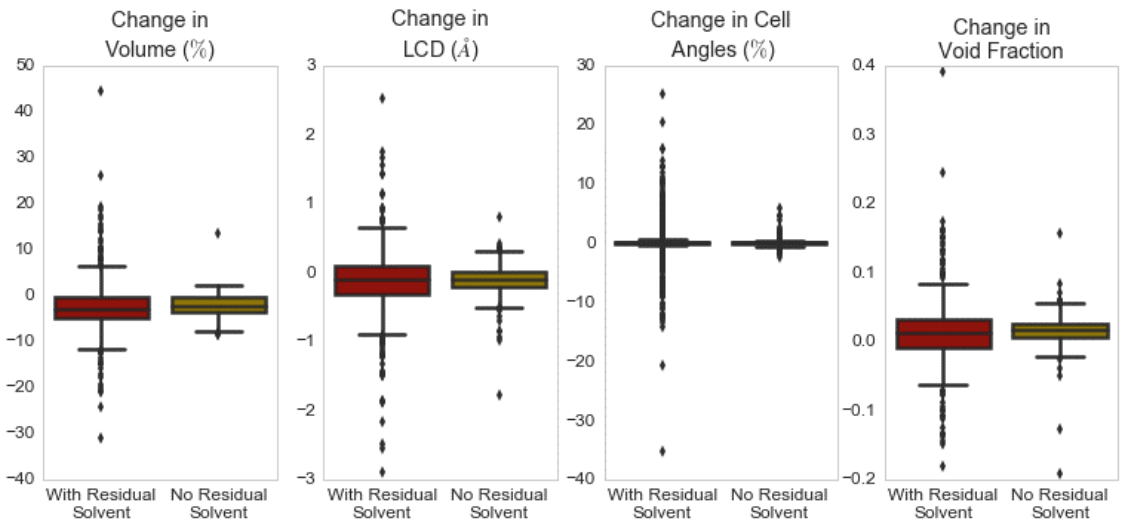

Figure 6.4: A box and whisker diagram for change in volume, change in LCD, change in cell angles, and change in void fraction for structures during DFT energy minimization with and without solvent in the CSD version of the structure. The markers represent the lowest 1.5 IQR, 1st quartile, median, 3rd quartile, and highest 1.5 IQR where IQR is the difference between the 3rd and 1st quartile.

MOF structures with solvent in the CSD representation can further be divided into two categories, those with at least one bound solvent and those with only free solvent. We find only small differences in the impact of solvent type on changes in structural parameters (see Figure 6.5).

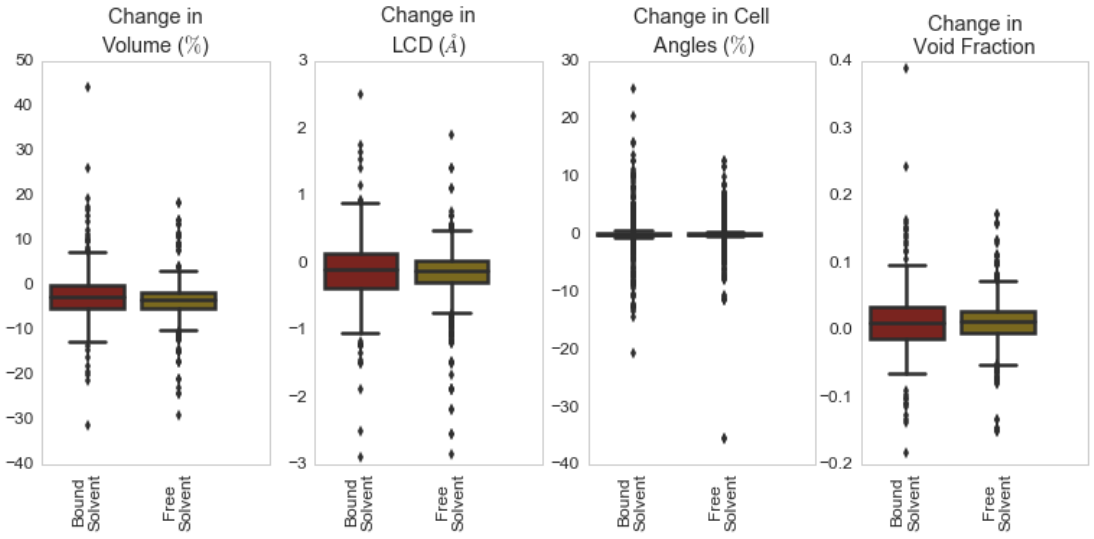

Figure 6.5: A box and whisker diagram for change in volume, change in LCD, change in cell angles, and change in void fraction for structures during energy minimization with at least one bound solvent and only free solvent in the CSD version of the structure. The markers represent the lowest 1.5 IQR, 1st quartile, median, 3rd quartile, and highest 1.5 IQR where IQR is the difference between the 3rd and 1st quartile.

The Cd based MOF JUC-63 (REFCODE: OFODAP)[36] is an example of MOF with substantial change in the structure after energy minimization. Figure 6.6(a) shows a representation of the MOF as found the CSD. This structure includes both types of solvent, freely suspended DMF molecules inside the MOF pores as well as DMF molecules bound to the Cd metal center. In the synthesis literature for JUC-63, Qiu et al. note that the structure was obtained with residual solvent and report structural parameters consistent with Figure 6.6(b), which is what can be found in the CoRE MOF database. When this structure is energy minimized, the structure deforms substantially and decreases in volume,

see Figure 6.6(c). This energy minimized structure is 44.4% smaller in volume than the original structure, with a 2 Å smaller LCD.

The observation that a MOF structure can change significantly upon solvent removal is not surprising. Indeed, one of the major advances in early work on MOFs was the discovery of materials which did not undergo pore collapse after solvent removal. Our results, have important implications for effort to use high-throughput computational methods to assess properties of MOFs because they represent an important refinement to the original CoRE MOF database, which ignored potential structural effects due to solvent removal.

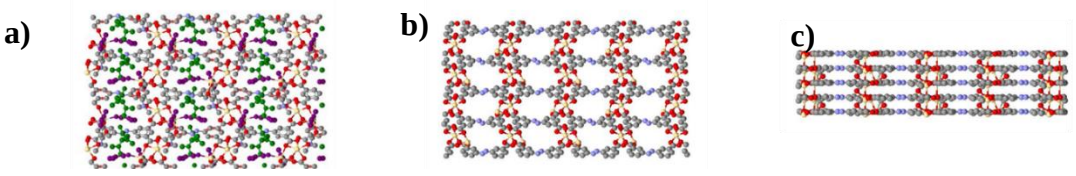

Figure 6.6: (a) Representation of JUC-63 as found in the CSD containing both bound (in purple) and free (in green) DMF molecules. (b)Representation of JUC-63 discussed in synthesis literature and found in the CoRE MOF database. (c) Representation of JUC-63 after DFT minimization, implying that the MOF changes drastically after activation.

6.3.3 Impact of Large Structural Changes on DDEC Point Charges

In Chapter 3, we showed that point charges assigned to MOFs using the DDEC method are insensitive to small structural changes. It is important, however, to reexamine this issue for materials that undergo significant structural change during DFT energy minimization. For the purpose of this study, we have identified structures with a large

change as those for which pore descriptors changed by more than 1 Å or volume changed by more than 10%. We only examined MOFs in the DDEC MOF Point Charge database. A total of 87 structures met both of these criteria (see Appendix D). For these MOFs we recalculated DDEC point charges for the energy minimized structures as explained in section 6.2.4. Point charges were assigned to each atom type based on coordination. Figure 6.7 shows a comparison of DDEC point change for each atom type for the experimental and energy minimized structure. Despite the significant structure changes that exist for these structures, we find similar results to those discussed in Chapter 3. The largest difference between charges for an energy minimized and experimental structures, 0.19 electrons, is seen in the Cd atom of MOF ICEGED[37]. Point changes show a mean absolute deviation (MAD) of 0.023 electrons where MAD is defined as

$$MAD = \sum_i \frac{x_{i_{orig}} - x_{i_{DFT}}}{N} \tag{3.2}$$

where i is atom type. $x_{i_{orig}}$ is the point charge for atom type i predicted for the original experimental structures, $x_{i_{DFT}}$ is the point charge for atom type i predicted for the energy minimized structures, and N is the number of atom types for all MOFs. These observations suggest that using point charges for any of the structures linked in the DDEC MOF point charge database without change in a reasonable approximation for any of the ~900 DFT relaxed structure we have reported is acceptable.

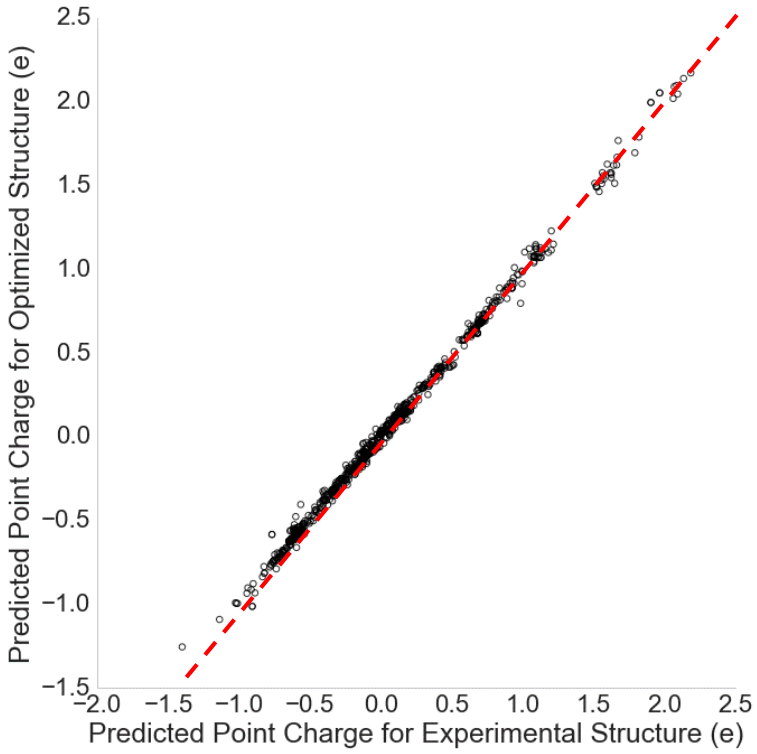

Figure 6.7: Direct comparison of DDEC charges predicted for each atom type of a MOF structure before and after energy minimization.

6.3.4 Adsorption Properties

GCMC predictions of methane uptake at 65 bar and CO_2 update at 1 bar were calculated for the experimentally observed and energy minimized representations of the 502 structures with DDEC point charges. For consistency, all charges, including charges for MOFs with significant structural changes, were assigned based on the MOF DDEC Point Charge database. We emphasize that in all GCMC calculations the structure of the adsorbent was assumed to be rigid.

As shown in Figure 6.9, there is a less than 25% change in methane uptake for 78% of the structures and less than 25% change in CO_2 uptake for 46% of the structures after energy minimization of the structure, respectively. We find that the degree of change in uptake is not correlated with magnitude of uptake. That is, structures that have higher or lower uptake are not necessarily more sensitive to structure changes. For simulations, a 5% difference between the initial and refined structures considered acceptable. We find that CO_2 changes more than the acceptable 5% for approximately 90% of the structures. This is a significant observation, specifically for the high-throughput screening community, and indicates the importance of structure precision.

As expected, we find that the change in uptake for structures with significant change in geometry correlates strongly with change in void fraction. However, we find only a weak correlation between change in void fraction and uptake for structures with minor changes in geometry. As shown in Figure 6.9, some structures experience a change in void fraction of less than 0.05 but more than 100% increase in CO_2 uptake or 200% increase in methane uptake. For example, MOF HUHJAW[38], a Cd and Cl based MOF, shows a 3% increase in volume and a 0.047 change in void fraction after energy minimization. Even with this apparently small change in geometry, the computed methane uptake increases from 8.48 to 25.97 cm^3 of adsorbate (STP)/cm^3 of MOF. MOF NASCIV[39], a Cd based MOF, shows an 8% change in volume and 0.04 change in void fraction after energy minimization but an increase in CO_2 uptake of 9.28 to 18.26 cm^3 of adsorbate (STP)/cm^3 of MOF.

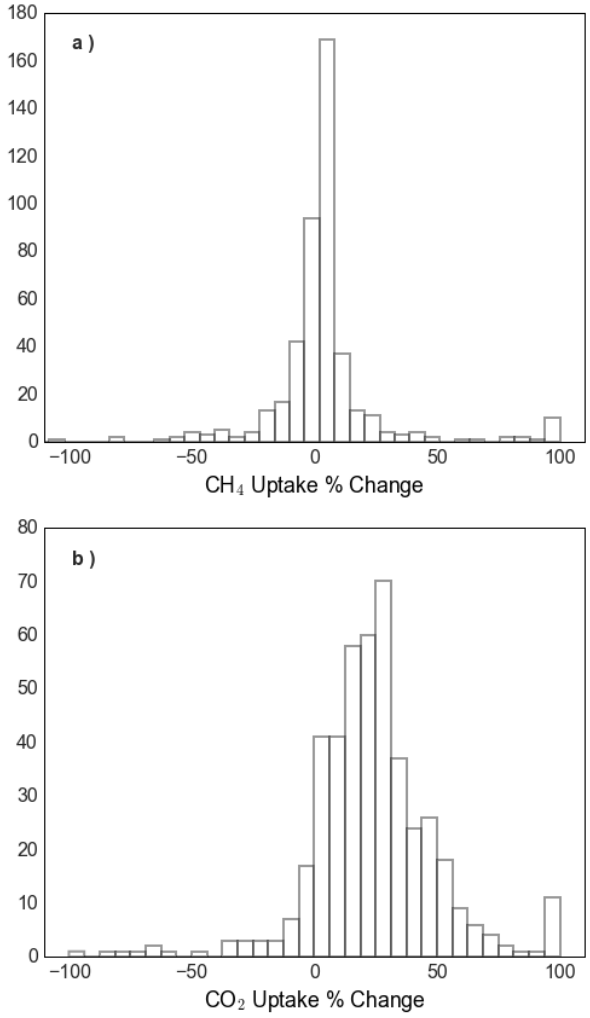

Figure 6.8: Histogram of percent difference in computed uptake between the original experimental and the DFT energy minimized structures for 502 MOFs. The vertical axis in each case is the number of structures. A less than 25% difference is observed for (a) methane uptake for 78% of the structures and (b) CO_2 uptake for 46% of the structures.

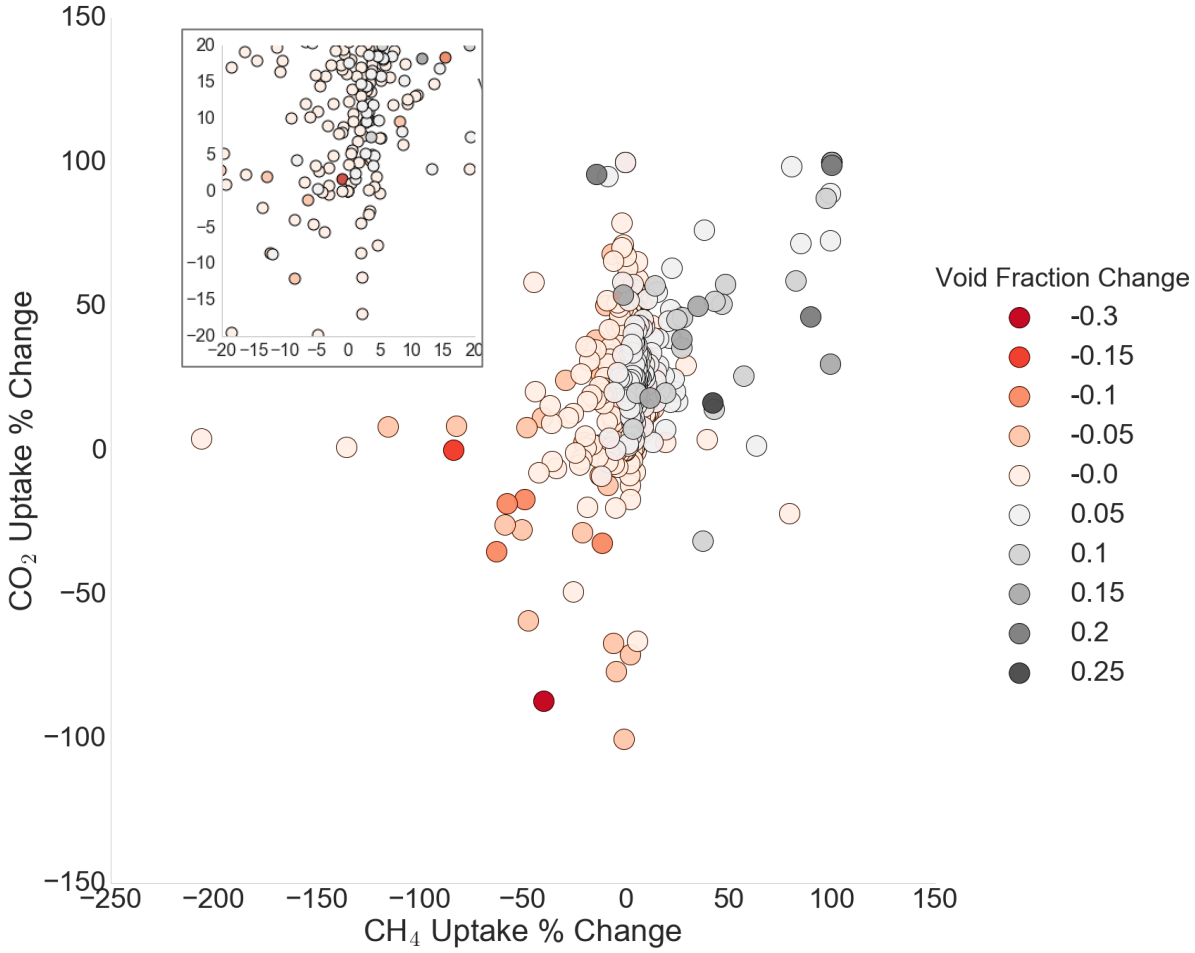

Figure 6.9: Percent difference in CO_2 (1 bar and 298 K) and CH_4 (65 bar and 298 K) uptake and void fraction between structures found in the CoRE MOF database and energy minimized structure.

Our results show that adsorption properties can be dependent in a complex manner on the potential energy landscape of the adsorbate molecule within the structure. Figure 6.10 shows the relationship between change in adsorbate uptake and pore diameters of the original structure. The results show that almost all structures with a significant difference in uptake have pore sizes less than 5 Å, indicating a larger degree of

adsorbate interaction with the pore walls. It is important to note, however, that not all MOFs with a LCD of less than 5 Å behave this way. Of the 165 structures with an LCD less than 5 Å, 108 and 120 structures showed a difference in computed CO_2 and CH_4 uptake of less than 25% after DFT energy minimization of the structure, respectively. Figure 6.10 shows that for structures with 6 Å or larger LCDs, CH_4 uptake is less sensitive to structural change. This is not true for CO_2 uptake, where structures with LCD of 12 Å can still undergo up to 100% change in uptake.

For some MOFs, we find that structural relaxation leads to an increase in methane uptake but a decrease in CO_2 uptake. One such example is MOF CICYIX[40], a Cd based MOF shown in Figure 6.11. During minimization, the unit cell of CICYIX transitions from an orthorhombic structure into a triclinic structure. The LCD of the structure increases by 5% and framework density increases by 3%. This results in an increase from 0.22 to 15.87 cm^3 (STP)/cm^3 increase in methane uptake. While methane uptake goes from almost no uptake to a noticeable amount, CO_2 uptake drops from a relatively high uptake of 154.40 cm^3 (STP)/cm^3 to almost no uptake of 3.29 cm^3 (STP)/cm^3. As shown in Figure 6.11, in the experimental structure, CO_2 adsorbs systematically in a single location in every pore. That is, there are specific pockets within the MOF pore that are ideal for CO_2 adsorption. In the energy minimized structure, the GCMC results show only one CO_2 molecule adsorbed in the supercell considered. This adsorption is not statistically relevant and can be considered the higher limit of CO_2 uptake for the MOF.

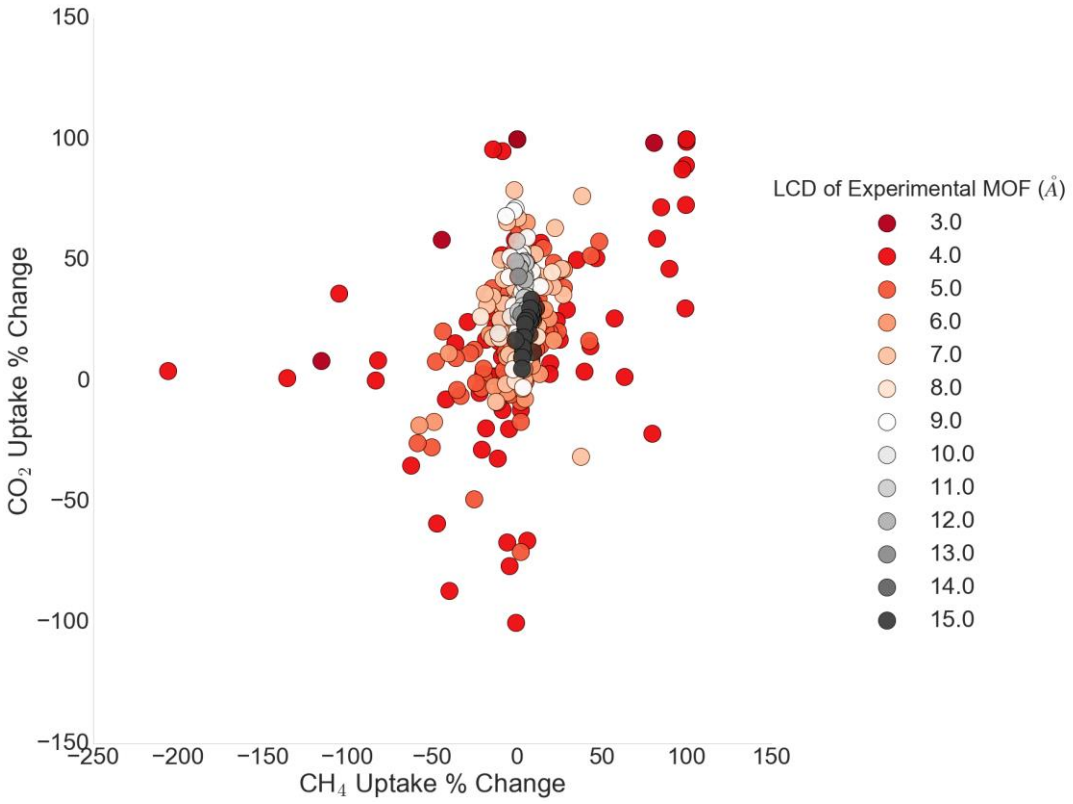

Figure 6.10: Percent difference in CO_2 (1 bar and 298 K) and CH_4 (65 bar and 298 K) uptake between structure found in the CoRE MOF database and energy minimized structure as a function of the original structure's LCD.

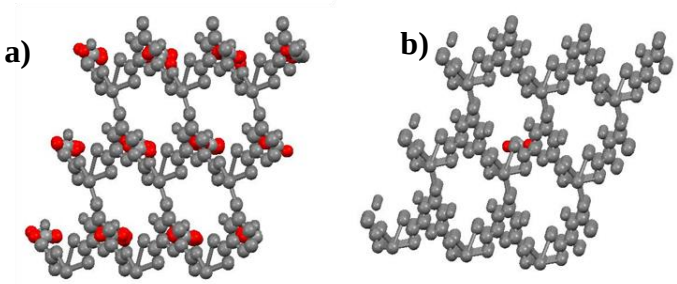

Figure 6.11 The framework of CICYIX shown in grey and CO_2 molecules adsorbed during GCMC calculations at 1 bar and 298 K shown in red for (a) the structure of CICYIX found in the CoRE MOF database and (b) after energy minimization.

To further probe the sensitivity of CO_2 uptake in CICYIX, small structure changes were introduced to the DFT minimized structure through a 400 fs dynamics calculation using ab initio molecular dynamics (AIMD), which does not require specification of a force field for the MOF degrees of freedom. Further details on AIMD calculations are given in Appendix D. GCMC calculations for CO_2 adsorption were performed for four snapshots taken from the AIMD simulations, at 2 fs, 269 fs, 320 fs, and 369 fs. The snapshot at 2 fs represents a minor change in atomic positions of the structure. We find that even with this small change in atomic positions, CO_2 uptake can increase to 110.32 cm^3 (STP) /cm^3, see Figure 6.11. To evaluate more random displacement in atomic positions and changes in the unit cell, three snapshots were obtained at random intervals starting at the randomly chosen 269 fs AIMD step. All reported uptakes and heats of adsorption for CICYIX were calculated by averaging and calculating the standard error among 10 GCMC calculations of uptake at 1 bar and 298 K. Adsorption studies in these snapshots show uptakes ranging from 70 to 90 cm^3 (STP) /cm^3. These changes in uptake at 50 fs intervals correspond to less than 1° change in the unit cell angles and 0.5 Å change in unit cell lengths.

As shown in Figure 6.12 (d), the DFT energy minimization of the structure results in a shift in pore size distribution. After 2 fs of AIMD in the energy minimized structure, we find a 40% increase in the number of 3.3 Å pores and a 25% decrease in the number of 3.4 Å pores. Along with this structural change, we find a 10 kJ/mol increase in heat of adsorption. It is possible that the smaller pores result in an increased pore wall and adsorbate interaction and ultimately a favorable CO_2 adsorption environment. We did not expect such a large difference in adsorption properties after 2 fs of AIMD. This observation highlights the high sensitivity of CICYIX to changes in atomic position. After 269 fs of

AIMD, we find a larger and wider range of pore sizes. In these structures, the most prevalent pore sizes are 3.7- 4.2 Å, resulting in a CO_2 heat of adsorption that is an average of 4.4 kJ/mol less than at 2 fs (Figure 6.12 (a)).Upon visualization of adsorption, see Figure 6.12 (c), we find that CO_2 is adsorbed in fewer of the larger pores than the smaller pores. Using snapshots also allows us to consider the flexibility of the framework and its impact on adsorption properties. However, using snapshots from AIMD of the empty framework assumes that the framework flexibility is decoupled from the adsorbate.

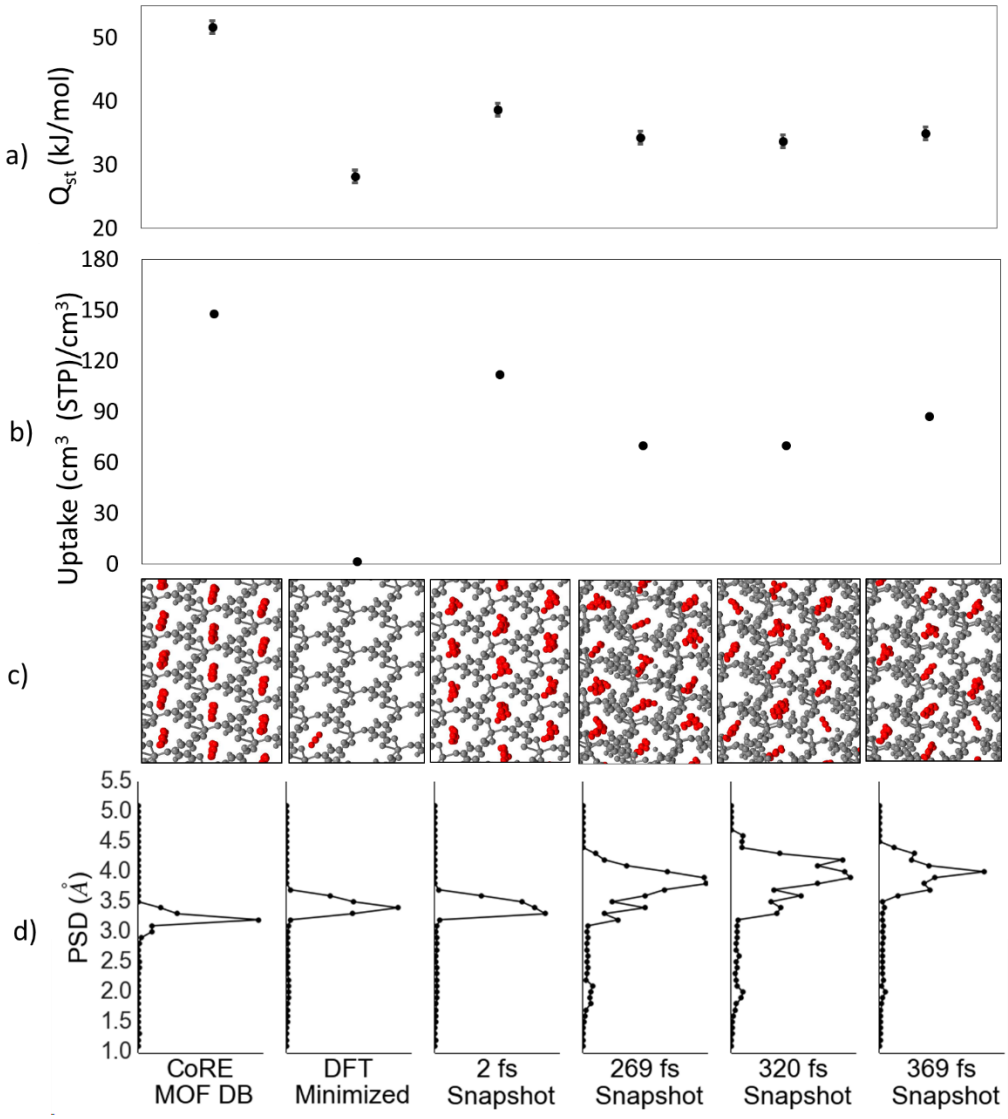

Figure 6.12: (a) Heat of adsorption calculated at 1 bar and 289 K. (b) Uptake of CO_2 at 1 bar and 298 K shows that choice of framework can drastically affect calculated results. (c) The framework of CICYIX shown in grey and CO_2 molecules adsorbed during GCMC calculations at 1 bar and 298 K shown in red. (d) Pore size distribution of each framework shows a large range of possible pore sizes for CICYIX.

To understand the framework response to the presence of CO_2 within the pores and to better understand the high uptake of the original experimental structure, we DFT energy minimized the structure with adsorbed CO_2 at 154.40 cm^3 (STP)/cm^3. Figure 6.13 shows

the pore size distribution of four cases: (1) Structure after DFT energy minimization of empty framework, (2) Structure from CoRE MOF database, (3) Structure from CoRE MOF database after energy minimization with CO_2 adsorbed in pores at 154.40 cm^3 (STP)/cm^3, (4) Structure after DFT energy minimization of empty framework after 2 fs of AIMD. The pore size distribution of case 3 is closely related to that of case 4. Next we removed the CO_2 from the pores of case 4 and recomputed a CO_2 uptake. The new CO_2 heat of adsorption (36.1 kJ/mol) is also closely related to that of the 2 fs snapshot (38.7 kJ/mol). As discussed earlier, 3.3 Å pores seem to be more favorable for CO_2 adsorption. This new structure, case 3, has 30% more 3.3 Å pores than the 2 fs snapshot which may account for its increased uptake of 130.37 cm^3 (STP)/cm^3 (see Appendix D).

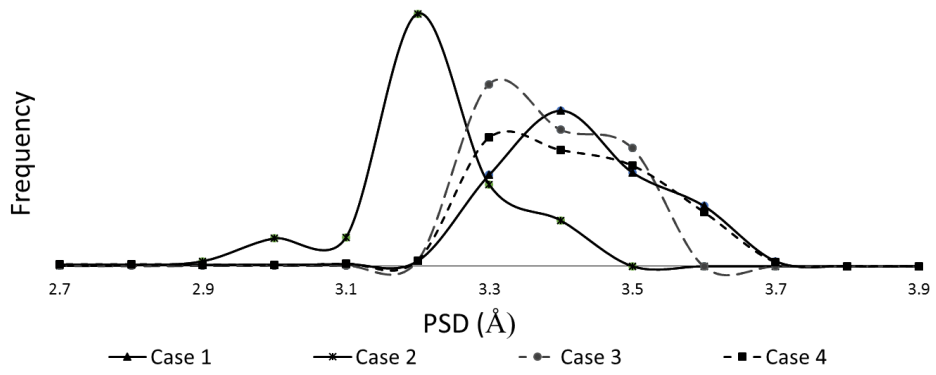

Figure 6.13: Pore size distribution (PSD) of structures in Case 1-4. The vertical axis represents normalized frequency.

In this chapter, we have identified MOFs like CICYIX where the high levels of pore wall and adsorbate interaction make the computed adsorption properties of CO_2 highly

sensitive to the precision of the framework structure. These results indicate that for MOFs with pore sizes close to that of the adsorbate in question, framework dynamics during adsorption studies can significantly impact the computationally calculated adsorption properties. While such structures require more care during simulation, they also present new opportunities in tuning pore structures to design highly CO_2 selective MOFs[41-43].

6.4 Conclusions

We have produced a diverse set of 900 DFT optimized MOF structures which is publicly available at http://dx.doi.org/10.11578/1118280 as a supplement to the CoRE MOF database. We have also assessed the change to the experimentally refined structures upon DFT energy minimization and shown that a majority of the structures undergo less than 10% change in structural parameters such as pore size, unit cell length, unit cell angles, unit cell volume, and void fraction. For MOFs with large changes upon energy minimization, we have highlighted the correlation between large structural change and presence of solvent during structural analysis. Previous high-throughput computational methods for assessing properties of MOFs have relied on the experimentally derived MOF structure. Such studies have ignored potential structural effects due to solvent removal. We anticipate our database of refined structures will have important implications for such high-throughput MOF screening efforts.

We have used the large set of DFT optimized structures to assess the effect of structural changes on adsorption properties of the MOFs. By studying uptake of CH_4 and CO_2 before and after optimization, we have shown that, for a majority of MOFs, methane uptake is not sensitive to small structural changes. However, we find that, for 56% of MOFs, CO_2 uptake changed by more than 25% upon minimization of the structure. We

found a weak correlation between change in structure and change in uptake. These results indicate that adsorption properties can be dependent in a complex manner on the potential energy landscape of the adsorbate molecule within the structure. We have also shown that almost all structures with a significant difference in uptake have small pore sizes, signifying the importance of adsorbate interaction with the pore walls. The CICYIX MOF, which has a pore size comparable to CO_2, was studied further to demonstrate the significance of small structural difference on computed adsorption properties. Specifically, this highlights the drastic difference including framework dynamics can have on computed adsorption properties of some MOFs.

Our results have significant implications for the MOF community. Structure precision is typically ignored in simulation of adsorption in MOFs. We have identified two types of precision which should be considered why performing adsorption calculations. First, great care should be given to the starting structure. If the MOF structure if obtained with residual solvent present in the pores, the structure should be energy minimized and validated. Even if the structure does not change significantly after energy minimization, GCMC calculations in the new energy minimized structure may result in a significantly different uptake value, especially for polar molecules where electrostatic interactions play an important role. Second, for MOFs with pore sizes comparable to the adsorbate, small fluctuations in the pore size can drastically change uptake properties. For such situations, consideration of framework flexibility is essential for a reliable predication of adsorption. To more reliably study adsorption properties, especially in a high-throughput manner, the MOF community must development a range of inexpensive methods to incorporate framework flexibility in adsorption calculations.

6.5 References

1. J. Su, E. Kapaca, L. F. Liu, V. Georgieva, W. Wan, J. L. Sun, V. Valtchev, S. Hovmoller and X. D. Zou, *Microporous and Mesoporous Materials*, 2014, 189, 115-125.

2. F. H. Allen, *Acta Crystallogr B*, 2002, 58, 380-388.

3. Y. G. Chung, J. Camp, M. Haranczyk, B. J. Sikora, W. Bury, V. Krungleviciute, T. Yildirim, O. K. Farha, D. S. Sholl and R. Q. Snurr, *Chem Mater*, 2014, 26, 6185-6192.

4. C. M. Simon, J. Kim, D. A. Gomez-Gualdron, J. S. Camp, Y. G. Chung, R. L. Martin, R. Mercado, M. W. Deem, D. Gunter and M. Haranczyk, *Energy & Environmental Science*, 2015, 8, 1190-1199.

5. H. Zhang, P. Deria, O. K. Farha, J. T. Hupp and R. Q. Snurr, *Energy & Environmental Science*, 2015, 8, 1501-1510.

6. M. Meilikhov, K. Yusenko and R. A. Fischer, *Dalton Transactions*, 2010, 39, 10990-10999.

7. T. Loiseau, C. Serre, C. Huguenard, G. Fink, F. Taulelle, M. Henry, T. Bataille and G. Ferey, *Chemistry-a European Journal*, 2004, 10, 1373-1382.

8. S. V. Potts, L. J. Barbour, D. A. Haynes, J. M. Rawson and G. O. Lloyd, *Journal of the American Chemical Society*, 2011, 133, 12948-12951.

9. S. Odoh, C. Cramer, D. Truhlar and L. Gagliardi, *Chemical Reviews*, 2015, 115, 6051-6111.

10. S. M. Woodley and R. Catlow, *Nat Mater*, 2008, 7, 937-946.

11. F. X. Coudert and A. H. Fuchs, *Coordination Chemistry Reviews*, 2016, 307, 211-236.

12. D. J. Earl and M. W. Deem, *Industrial & Engineering Chemistry Research*, 2006, 45, 5449-5454.

13. D. Nazarian, Ganesh P. ; Sholl, David S. , *J. Mater. Chem. A*, 2015, 3, 22432-22440.

14. V. Sharma, C. C. Wang, R. G. Lorenzini, R. Ma, Q. Zhu, D. W. Sinkovits, G. Pilania, A. R. Oganov, S. Kumar, G. A. Sotzing, S. A. Boggs and R. Ramprasad, *Nat Commun*, 2014, 5.

15. N. Chandrasekhar and D. S. Sholl, *Journal of Physical Chemistry C*, 2015, 119, 26319-26326.

16. R. Armiento, B. Kozinsky, M. Fornari and G. Ceder, *Phys Rev B*, 2011, 84.

17. F. Yan, X. W. Zhang, Y. G. Yu, L. P. Yu, A. Nagaraja, T. O. Mason and A. Zunger, *Nat Commun*, 2015, 6.

18. K. M. Nicholson, N. Chandrasekhar and D. S. Sholl, *Accounts of Chemical Research*, 2014, 47, 3275-3283.

19. A. Jain, G. Hautier, C. J. Moore, S. P. Ong, C. C. Fischer, T. Mueller, K. A. Persson and G. Ceder, *Computational Materials Science*, 2011, 50, 2295-2310.

20. A. Jain, S. P. Ong, G. Hautier, W. Chen, W. D. Richards, S. Dacek, S. Cholia, D. Gunter, D. Skinner, G. Ceder and K. A. Persson, *Apl Mater*, 2013, 1.

21. D. Nazarian, J. S. Camp and D. S. Sholl, *Chem Mater*, 2016, 28, 785-793.

22. J. Hutter, M. Iannuzzi, F. Schiffmann and J. VandeVondele, *Wires Comput Mol Sci*, 2014, 4, 15-25.

23. S. Goedecker, M. Teter and J. Hutter, *Phys Rev B*, 1996, 54, 1703-1710.

24. S. Grimme, *Journal of Computational Chemistry*, 2006, 27, 1787-1799.

25. S. Grimme, J. Antony, S. Ehrlich and H. Krieg, *Journal of Chemical Physics*, 2010, 132, 154104-154101-154119.

26. J. VandeVondele and J. Hutter, *Journal of Chemical Physics*, 2007, 127.

27. D. Dubbeldam, S. Calero, D. E. Ellis and R. Q. Snurr, *Molecular Simulation*, 2015, DOI: 10.1080/08927022.2015.1010082, 1-21.

28. T. F. Willems, C. Rycroft, M. Kazi, J. C. Meza and M. Haranczyk, *Microporous and Mesoporous Materials*, 2012, 149, 134-141.

29. D. Dubbeldam, S. Calero, D. Ellis and R. Snurr, unpublished work.

30. D. Peng and D. B. Robinson, *Ind Eng Chem Fund*, 1976, 15, 59-64.

31. A. K. Rappé, C. J. Casewit, K. Colwell, W. Goddard and W. Skiff, *Journal of the American Chemical Society*, 1992, 114, 10024-10035.

32. M. Martin and J. Siepmann, *Journal of Physical Chemistry B*, 1998, 102, 2569-2577.

33. C. Wilmer, O. Farha, Y. Bae, J. Hupp and R. Snurr, *Energy & Environmental Science*, 2012, 5, 9849-9856.

34. G. Kresse and J. Furthmuller, *Phys Rev B*, 1996, 54, 11169-11186.

35. Y. Cai, A. R. Kulkarni, Y. G. Huang, D. S. Sholl and K. S. Walton, *Cryst Growth Des*, 2014, 14, 6122-6128.

36. M. Xue, G. S. Zhu, Y. X. Li, X. J. Zhao, Z. Jin, E. Kang and S. L. Qiu, *Cryst Growth Des*, 2008, 8, 2478-2483.

37. J. Tao, Z. J. Ma, R. B. Huang and L. S. Zheng, *Inorganic Chemistry*, 2004, 43, 6133-6135.

38. X. L. Tong, D. Z. Wang, T. L. Hu, W. C. Song, Y. Tao and X. H. Bu, *Cryst Growth Des*, 2009, 9, 2280-2286.

39. D. C. Zhong, M. Meng, J. H. Deng, X. Z. Luo and Y. R. Xie, *Inorg Chem Commun*, 2011, 14, 1952-1956.

40. V. Yasodha, S. Govinclarajan, J. N. Low and C. Glidewell, *Acta Crystallogr C*, 2007, 63, M207-M215.

41. P. Deria, S. Li, H. D. Zhang, R. Q. Snurr, J. T. Hupp and O. K. Farha, *Chemical Communications*, 2015, 51, 12478-12481.

42. J. R. Li, J. M. Yu, W. G. Lu, L. B. Sun, J. Sculley, P. B. Balbuena and H. C. Zhou, *Nat Commun*, 2013, 4.

43. P. L. Llewellyn, S. Bourrelly, C. Serre, A. Vimont, M. Daturi, L. Hamon, G. De Weireld, J. S. Chang, D. Y. Hong, Y. K. Hwang, S. H. Jhung and G. Ferey, *Langmuir*, 2008, 24, 7245-7250.

CHAPTER 7

IMPACT OF FRAMEWORK FLEXIBILITY ON PREDICTED ADSORPTION PROPERTIES

7.1 Introduction

Computational modeling of Metal-Organic Framework (MOFs) properties have contributed greatly to the understanding of MOFs and their potential applications. Specifically, modeling gas adsorption with grand canonical Monte Carlo (GCMC) simulations has played an important role in the development of adsorbents for gas storage and separations.[1-5] As discussed in Chapter 4-6, GCMC simulations are used increasingly used to screen databases of MOFs for application in separations and storage. Such screening studies are accessible given the assumption that the MOF framework can be treated as rigid during the GCMC simulation.

As with any material, MOFs are not perfectly rigid. Multiple studies of gas diffusion in MOFs have demonstrated the importance of small fluctuations in the MOF framework on the predicted adsorption property.[6-9] Until recently, with the exception of breathing[6, 7, 10] and gate-opening[8] MOFs, the impact of flexibility was considered negligible for adsorption simulations. Recently methods have been developed to account for framework flexibility during GCMC simulations, but these methods are computationally expensive and not yet commonly used.[11-13] While there are numerous examples of computational studies which have successfully reproduced experimental adsorption results,[14, 15] there is currently no consensus on the importance of flexibility on predicting

adsorption. However, it is clear that there are cases where flexibility can play an important role. Our work in Chapter 6 demonstrates that small fluctuations in atomic positions and pore sizes can significantly change the predicted CO_2 adsorption properties. Forster et al. have also shown that predicted adsorption properties of Ar, Kr, and Xe are sensitive to the precision of the HKUST-1 structure.[16] Gee et al. have demonstrated that framework flexibility is crucial for predicting selectivity for o-xylene/ethylbenzene(oX/eb) in MIL-47.[13] In their study, Gee et al. showed that GCMC with a rigid DFT energy minimized structure for MIL-47 predicts a selectivity that is an order of magnitude larger than the experimentally predicted value. However, using a "snapshot method", they captured flexibility in MIL-47, predicting a more accurate selectivity, closer in magnitude to the experimental result. In this snapshot method, Gee et al. obtained structures from a molecular dynamics simulation of the empty framework. They used the snapshots as input to a GCMC simulation of adsorption where the framework is treated as rigid. This method is useful for considering the flexibility of the framework and its impact on adsorption properties. However, using snapshots from molecular dynamics of the empty framework assumes that the framework flexibility is decoupled from the adsorbate.[17, 18]

The aim of this project is to further quantify the extent to which flexibility of the MOF framework may impact adsorption. We have chosen three commonly studied MOFs (UiO66[19], HKUST-1[20], IRMOF-1[21]) with a moderate pore size (5-10 Å) and, using the snapshot method, investigated prediction of adsorption of methane, CO_2, and oX/eb. Methane represents a control adsorbate, CO_2 was chosen due to the intriguing results in Chapter 6, and oX/eb was chosen to extend upon work done by Gee et al. We emphasize that we have not considered examples where the overall crystal structure changes upon

adsoption, such as breathing or deformations of the framework induced by the adsorbate, such as swelling or gate-opening.

7.2 Methods and Computational Details

7.2.1 AIMD Simulations

Prior to AIMD simulations, each MOF structure was energy minimized. All energy minimizations were performed using the plane-wave DFT computational package VASP5.2.12.[22] We have previously shown that funcitonals PBE[23], PBE-D2[24], and PBE-D3[25, 26], PW91[27-29], M06L[30] or vdw-DF2[31] all reliably predict MOF structure and that dispersion corrected functionals, on average, tend to perform best.[32] Given our findings, the PBE-D2 functional was used. The Brillouin zone was sampled with a 1000 points per atom density Monkhorst-Pack grid. An energy cut off of 520 eV was used for all calculations without spin polarization. Simulations were performed in two parts. First, we performed energy minimization for only ionic positions based on a conjugate gradient algorithm. A subsequent minimization used the final positions of the first minimization, introduced the cell shape and volume as degrees of freedom and switched to a quasi-Newton minimization algorithm. Cartesian coordinate convergence criteria of a maximum change in system energy of 5×10^{-4} eV per atom and a maximum change in force of 3×10^{-3} eV $Å^{-1}$ were applied to all energy minimization calculations.

All dynamics calculations were performed using ab initio molecular dynamics (AIMD), which does not require specification of a force field for the MOF degrees of freedom. AIMD calculations were carried out on the empty framework using the Gaussian plane-wave (GPW) computational package CP2K 2.6[33] on the Argonne National

Laboratories supercomputer MIRA. The Goedecker, Teter, Hutter dual-space pseudopotentials (GTH)[34] with the PBE functional, 650 Ry cutoff, and double-zeta valance polarized (DZVP)[35] basis sets were used. Simulations were performed in the NPT ensemble at 300 K (Nose thermostat) and 1 bar, using a 1 fs timestep.

To analyze changes in structure throughout the AIMD simulation, we have calculated unit cell volume, unit cell angles, unit cell lengths, and pore descriptors. Pore descriptors were measured using the Zeo++ geometry analysis package.[36]

7.2.2 GCMC Simulations of Uptake and Selectivity

GCMC simulations of methane adsorption were conducted using the RASPA 2.0 code.[37, 38] Methane adsorption was simulated at 65 bar and 298 K. The Peng Robinson equation of state[39] was used to calculate the fugacity values necessary to impose equilibrium between the system and the external gas reservoir. Methane-methane and methane-framework interactions were modeled with a Lennard-Jones (LJ) 12-6 potential using the Lorentz-Berthelot mixing rules. The LJ parameters for all framework atoms were obtained from the Universal Force-Field (UFF).[37] The LJ parameters for methane (ε/k_B = 148.0 K; σ = 3.73 Å) were obtained from the TraPPE force-field, modeled as a single sphere with one LJ interaction site.[40] All LJ interaction potentials were truncated at 13.0 Å. To satisfy the minimum image convention all simulation cells were replicated to at least 26.0 Å along each axis. All GCMC simulations included a 200,000-cycle equilibration period followed by a 200,000- cycle production period.[22] GCMC simulations included random insertion, deletion, translation, and re-insertion moves with equal probabilities.

GCMC calculation of CO_2 adsorption were performed at 65 bar and 298 K in a similar manner to methane adsorption calculations. Point charges used for each structure

can be found in Appendix E. All GCMC simulations included a 500,000-cycle equilibration period followed by a 500,000- cycle production period. The LJ parameters for CO_2 were obtained from the TraPPE force-field, modeled as a 3-site molecule as described in Appendix D.[40]

Binary GCMC calculations of ethylbenzene and o-xylene were calculated at 0.05 bar and 298 K. Simulations included a 500,000-cycle equilibration period followed by a 500,000- cycle production period. The LJ parameters and charges for ethylbenzene and o-xylene were adopted from the work by Gee et al.[13] In this work, selectivity is defined as

$$\frac{x_{oX}}{x_{eb}}\frac{y_{eb}}{y_{oX}}$$

where x and y are the concentrations in the adsorbed phase and equimolar vapor phase, respectively.

7.3 Results and Discussion

7.3.1 Analyzing Extent of Flexibility

Each AIMD simulation was allowed 2 ps of equilibration. Although this is a short time scale it appears to be sufficient for adequate exploration of the energy and lattice parameters for each material. For UiO66 and HKUST-1, unit cell lattice angles (α, β, γ) fluctuate within 4° and unit cell lengths (a, b, c) fluctuate within 2 Å. For IRMOF-1, the fluctuations are slightly larger, with angles fluctuating within 6° and lengths fluctuations within 4 Å. We have successfully computed AIMD calculations for 14 ps in UiO66, 5.8 ps

for HKUST-1, and 19 ps for IRMOF-1. We have isolated four snapshots from the UiO66 simulation at 0.5 ps intervals, seven snapshots from the HKUST-1 simulation at 0.25 ps intervals, and six snapshots from the IRMOF-1 simulation at 2 ps intervals. The number of snapshots was arbitrarily chosen. For these snapshots, we have also calculated the pore size distribution.

UiO66 and IRMOF-1 show a larger range of pore distributions, noticeably different than that of their DFT minimized structure. However, the pore size distribution of HKUST-1 fluctuates less and does not deviate drastically from the DFT minimized structure. This is expected as HKUST-1 is typically considered a "rigid" MOF, with each organic linker secured into position through bonds with 3 different metal centers. This allows for less flexibility in the linker relative to the 2-node linker connections found in UiO66 and IRMOF-1. Pore size distributions are shown and discussed in more detail in section 7.3.2.

7.3.2 Impact on Adsorption

Figure 7.1 shows methane uptake at 65 bar and 298 K for all the snapshots considered in each MOF. We find that while the predicted uptake is different among snapshots, the magnitude of the difference is less than 5%, a typically acceptable amount of imprecision for GCMC calculations. For UiO66, we find an average of 110.62 cm^3(STP)/cm^3 methane uptake with a standard deviation of 0.93 compared to 111.27 cm^3(STP)/cm^3 methane uptake in the DFT energy minimized structure. For HKUST-1, we find an average of 161.89 cm^3(STP)/cm^3 methane uptake with a standard deviation of 2.51 compared to 166.39 cm^3(STP)/cm^3 methane uptake in the DFT energy minimized structure. For IRMOF-1, we find an average of 129.13 cm^3(STP)/cm^3 methane uptake with a standard

deviation of 2.32 compared to 125.09 cm^3(STP)/cm^3 methane uptake in the DFT energy minimized structure.

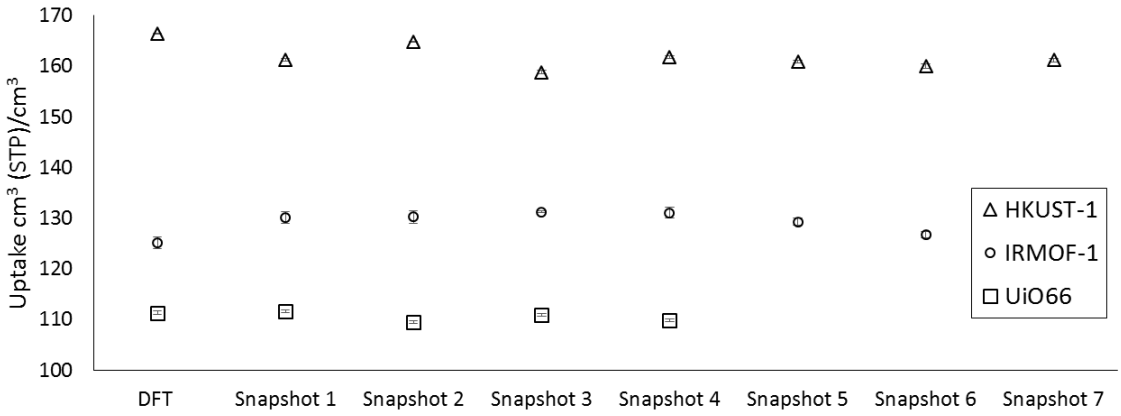

Figure 7.1: GCMC-simulated methane uptake in HKUST-1, IRMOF-1, and UIO66 at 65 bar and 298 K using the DFT energy minimized structure and the snapshots obtained from AIMD simulations. Error bars represent the standard error derived from block averaging during GCMC simulations.

To consider a more complicated case, we have simulated the adsorption of CO_2, where electrostatic interactions with the MOF framework play a role in adsorption. Figure 7.2 (a) shows the uptake and heat of adsorption (Q_s) of CO_2 in the energy minimized UiO66 and the four AIMD snapshots. Figure 7.2 (c) shows the corresponding pore size distribution of each UiO66 structure. When comparing results from the snapshots to the DFT method, we find at most a 2 cm^3 (STP)/cm^3 increase in predicted CO_2 uptake and 1 kJ/mol increase in heat of adsorption. While there is a statistically significant different between the properties predicted for the DFT minimized structure and the snapshots, the magnitude of this difference is relatively small, less than 5%. This is unexpected given the noticeable

difference in pore size distribution. Structures obtained from the AIMD snapshots have a third smaller pore size, around 6.5 Å, which is not present in original UiO66 structure.

Figure 7.2 (b) shows how such structure precision and flexibility may impact prediction of binary adsorption for a system with larger molecules, eb and oX. We find that selectivity for oX over eb from an equimolar mixture can be as different as 30% if a snapshot structure instead of the DFT energy minimized structure is used for GCMC calculations. However, as shown in Figure 7.2(b), the calculated selectivities are within error and no conclusions can be drawn from the following simulations without more converged data.

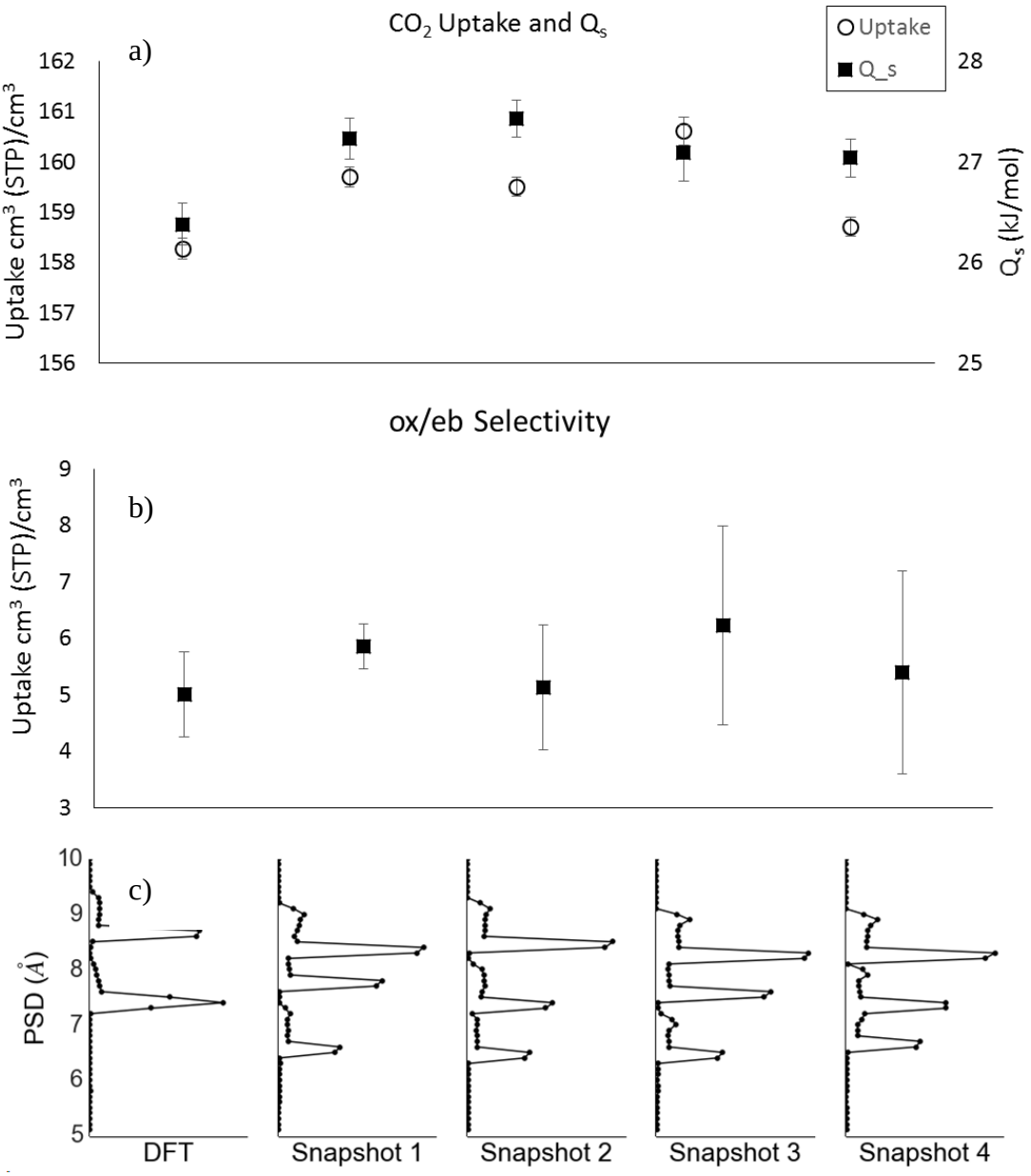

Figure 7.2: (a) GCMC-simulated CO_2 uptake and heat of adsorption, (b) GCMC-simulated oX/eb selectivity (c) pore size distribution (PSD) of the UiO66 framework DFT energy minimized and obtained from AIMD simulations.

Similarly, we have studied CO_2 uptake and oX/eb selectivity in HKUST-1. Figure 7.3 (a) shows the uptake and Q_s of CO_2 in the energy minimized HKUST-1 and the seven

AIMD snapshots. Figure 7.3 (c) shows the corresponding pore size distribution of each HKUST-1 structure. There is a less than 1% difference in predicted uptake and heat of adsorption for CO_2 among structures. For the case of HKUST-1, we find that snapshot method and the conventional method (using the DFT minimized structure) predict similar results. This holds true for prediction of oX/eb selectivity (see Figure 7.3 (b)). However, this is not true for the individual loading of oX and eb during the binary GCMC simulations. We find that while selectivity is unaffected, loading of eb fluctuates between 37-53 cm^3 (STP)/cm^3 and can be up to 15% different from the uptake predicted for the DFT minimized structure. Similarly, loading of oX fluctuates between 53-58 cm^3 (STP)/cm^3 and can be up to 8% different from the uptake predicted for the DFT minimized (See Appendix E). This is a significant observation given the nuance changes in pore size distribution for the considered snapshots of HKUST-1. It suggests that depending on the system and the specific adsorption property considered, flexibility may play an important factor or the results. Table 7.1 shows the average value and standard deviation among GCMC simulations of snapshots compared to the property predicted in DFT energy minimized structure.

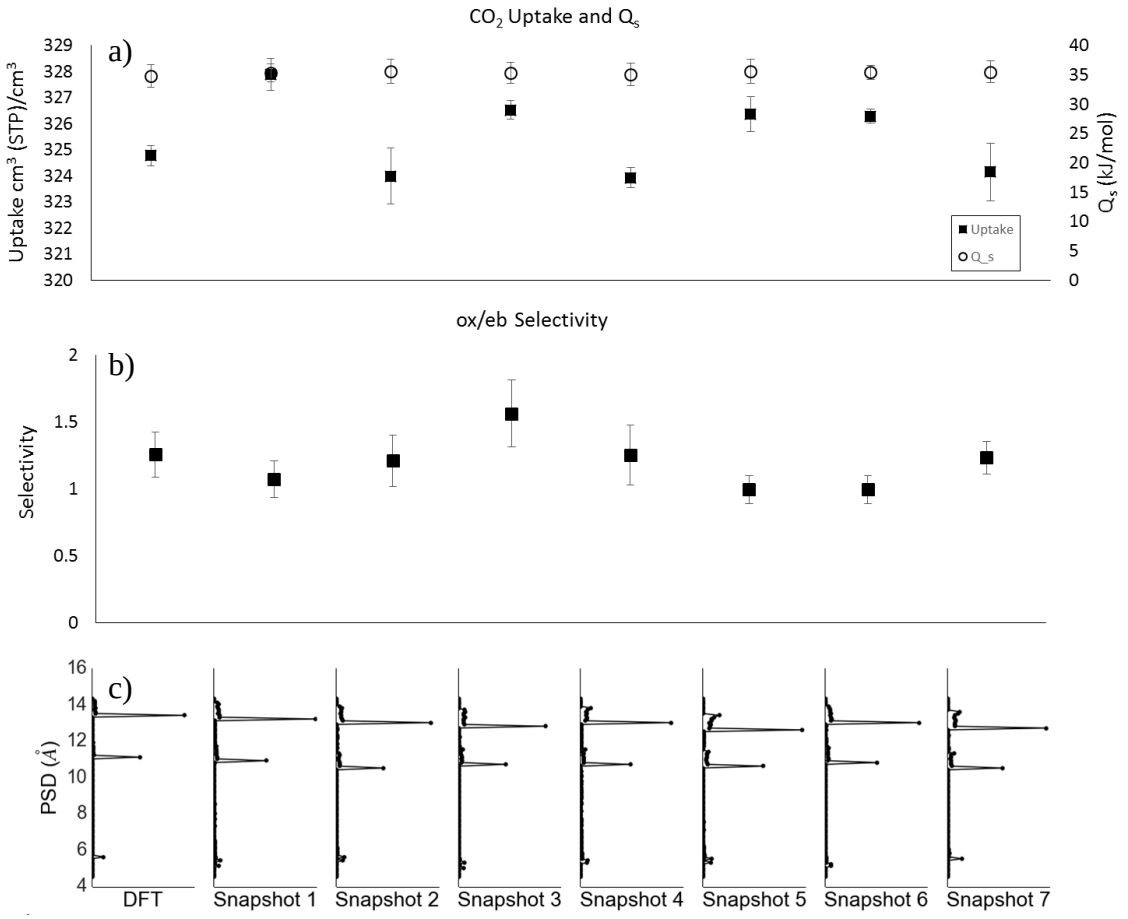

Figure 7.3: (a) GCMC-simulated CO_2 uptake and heat of adsorption, (b) GCMC-simulated oX/eb selectivity (c) pore size distribution (PSD) of the HKUST-1 framework DFT energy minimized and obtained from AIMD simulations.

Finally, we have considered CO_2 uptake and oX/eb selectivity in IRMOF-1. Figure 7.4 (a) shows the uptake and Q_s of CO_2 in the energy minimized IRMOF-1 and the six AIMD snapshots. Figure 7.4 (c) shows the corresponding pore size distribution of each IRMOF-1 structure. The snapshot methods predicts a higher CO_2 uptake, but there is a less than 5% difference in predicted uptake and Q_s among structures. This holds true for

prediction of oX/eb selectivity (see Figure 7.4 (b)). Similarly we see minor differences in the pore size distributions calculated for all IRMOF-1 structures.

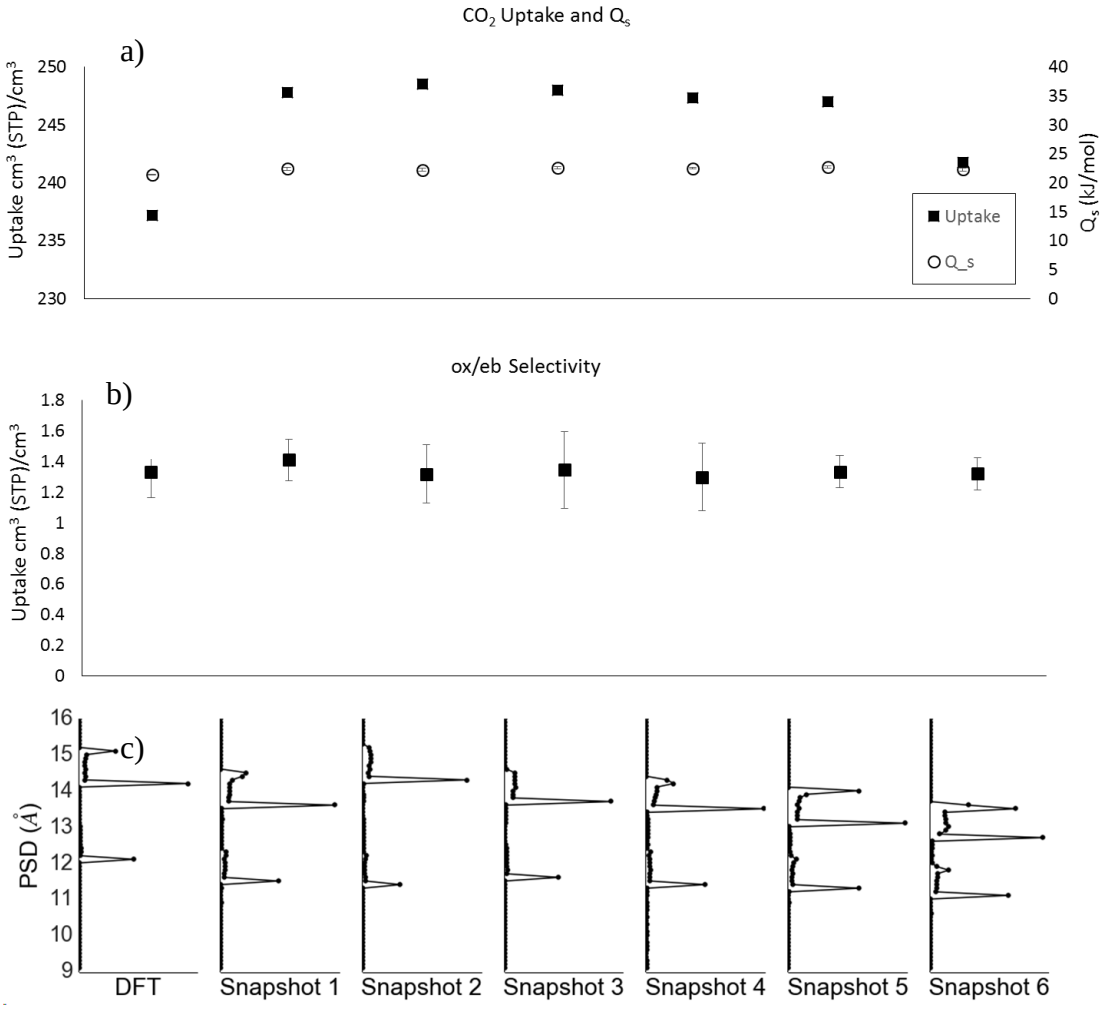

Figure 7.4: (a) GCMC-simulated CO_2 uptake and heat of adsorption, (b) GCMC-simulated oX/eb selectivity (c) pore size distribution (PSD) of the IRMOF-1 framework DFT energy minimized and obtained from AIMD simulations.

Table 7.1: GCMC simulated adsorption properties for UiO66, HKUST-1, and IRMOF-1. Reasonable agreement between average property values from snapshots to the DFT structure properties.

	UiO66			**HKUST-1**			**IRMOF**		
	DFT	Snapshot Avg.	Std. Dev.	DFT	Snapshot Avg.	Std. Dev.	DFT	Snapshot Avg.	Std. Dev.
Co_2 uptake [cm^3 (STP)/cm^3]	158.28	159.64	0.78	324.77	325.60	1.56	237.23	246.74	2.50
Co_2 Q_s [kJ/mol]	26.38	27.20	0.18	34.79	35.43	0.21	21.45	22.48	0.17
Ox/eb [cm^3 (STP)/cm^3]	5.00	5.65	0.49	1.26	1.19	0.20	1.33	1.34	0.04

7.4 Conclusions

In this work we have expanded upon our findings in Chapter 6 and further investigated the impact of framework flexibility on molecular simulations of adsorption in MOFs with moderate size pores. We have considered adsorption of methane, CO_2, and binary oX/eb in three commonly studied MOFs: UiO66, HKUST-1, and IRMOF-1. Our results show that flexibility of the framework does not significantly impact CO_2 or methane uptake in these MOFs. However, including flexibility can noticeably impact the predicted loading of xylenes as in the case of HKUST-1. Throughout this work we have utilized the snapshot method which uses structures from molecular dynamics of the empty framework.[13] This is an efficient method which we believe can be used to quickly gauge the sensitivity of predicted adsorption properties to incorporation of framework selectivity. However, this methods assumes that the framework flexibility is decoupled from the

adsorbate. It will be important in the future to consider a coupled interaction between the framework and adsorbate to better understand the important of MOF flexibility on prediction of adsorption behavior.

7.5 References

1. P. Ryan, O. K. Farha, L. J. Broadbelt and R. Q. Snurr, *Aiche Journal*, 2011, 57, 1759-1766.

2. M. P. Suh, H. J. Park, T. K. Prasad and D. W. Lim, *Chemical Reviews*, 2012, 112, 782-835.

3. H. Wu, Q. Gong, D. Olson and J. Li, *Chemical Reviews*, 2012, 112, 836-868.

4. T. Watanabe, S. Keskin, S. Nair and D. S. Sholl, *Physical Chemistry Chemical Physics*, 2009, 11, 11389-11394.

5. C. M. Simon, J. Kim, D. A. Gomez-Gualdron, J. S. Camp, Y. G. Chung, R. L. Martin, R. Mercado, M. W. Deem, D. Gunter, M. Haranczyk, D. S. Sholl, R. Q. Snurr and B. Smit, *Energy & Environmental Science*, 2015, 8, 1190-1199.

6. N. Ramsahye, G. Maurin, S. Bourrelly, P. Llewellyn, T. Loiseau, C. Serre and G. Ferey, *Chemical Communications*, 2007, DOI: 10.1039/b702986a, 3261-3263.

7. A. M. Walker, B. Civalleri, B. Slater, C. Mellot-Draznieks, F. Corà, C. M. Zicovich-Wilson, G. Román-Pérez, J. M. Soler and J. D. Gale, *Angewandte Chemie International Edition*, 2010, 49, 7501--7503.

8. D. Fairen-Jimenez, S. Moggach, M. Wharmby, P. Wright, S. Parsons and T. Duren, *Journal of the American Chemical Society*, 2011, 133, 8900-8902.

9. B. Zheng, Y. Pan, Z. Lai and K. Huang, *Langmuir*, 2013, 29, 8865-8872.

10. F. Coudert, M. Jeffroy, A. Fuchs, A. Boutin and C. Mellot-Draznieks, *Journal of the American Chemical Society*, 2008, 130, 14294-14302.

11. D. Dubbeldam, R. Krishna and R. Q. Snurr, *Journal of Physical Chemistry C*, 2009, 113, 19317-19327.

12. F. Coudert, A. Boutin, M. Jeffroy, C. Mellot-Draznieks and A. Fuchs, *Chemphyschem*, 2011, 12, 247-258.

13. J. A. Gee and D. S. Sholl, *Journal of Physical Chemistry C*, 2016, 120, 370-376.

14. S. Keskin, J. Liu, R. B. Rankin, J. K. Johnson and D. S. Sholl, *Industrial & Engineering Chemistry Research*, 2009, 48, 2355-2371.

15. E. Haldoupis, S. Nair and D. Sholl, *Journal of the American Chemical Society*, 2012, 134, 4313-4323.

16. K. V. Lawler, Z. Hulvey and P. M. Forster, *Physical Chemistry Chemical Physics*, 2015, 17, 18904-18907.

17. R. V. Awati, P. I. Ravikovitch and D. S. Sholl, *Journal of Physical Chemistry C*, 2013, 117, 13462-13473.

18. S. E. Boulfelfel, P. I. Ravikovitch and D. S. Sholl, *Journal of Physical Chemistry C*, 2015, 119, 15643-15653.

19. J. H. Cavka, S. Jakobsen, U. Olsbye, N. Guillou, C. Lamberti, S. Bordiga and K. P. Lillerud, *Journal of the American Chemical Society*, 2008, 130, 13850-13851.

20. S. S. Y. Chui, S. M. F. Lo, J. P. H. Charmant, A. G. Orpen and I. D. Williams, *Science*, 1999, 283, 1148-1150.

21. H. Li, M. Eddaoudi, M. O'Keeffe and O. Yaghi, *Nature*, 1999, 402, 276-279.

22. G. Kresse and J. Furthmuller, *Phys Rev B*, 1996, 54, 11169-11186.

23. J. P. Perdew, K. Burke and Y. Wang, *Phys Rev B*, 1996, 54, 16533-16539.

24. S. Grimme, *Journal of Computational Chemistry*, 2006, 27, 1787-1799.

25. S. Grimme, J. Antony, S. Ehrlich and H. Krieg, *Journal of Chemical Physics*, 2010, 132, 154104-154101-154119.

26. S. Grimme, S. Ehrlich and L. Goerigk, *Journal of Computational Chemistry*, 2011, 32, 1456-1465.

27. J. P. Perdew, J. A. Chevary, S. H. Vosko, K. A. Jackson, M. R. Pederson, D. J. Singh and C. Fiolhais, *Phys Rev B*, 1993, 48, 4978-4978.

28. J. P. Perdew, J. A. Chevary, S. H. Vosko, K. A. Jackson, M. R. Pederson, D. J. Singh and C. Fiolhais, *Phys Rev B*, 1992, 46, 6671-6687.

29. J. P. Perdew and Y. Wang, *Phys Rev B*, 1992, 45, 13244-13249.

30. Y. Zhao and D. Truhlar, *Accounts of Chemical Research*, 2008, 41, 157-167.

31. K. Lee, E. D. Murray, L. Z. Kong, B. I. Lundqvist and D. C. Langreth, *Phys Rev B*, 2010, 82, 081101-081101-081104.

32. D. Nazarian, P. Ganesh and D. S. Sholl, *J Mater Chem A*, 2015, 3, 22432-22440.

33. J. Hutter, M. Iannuzzi, F. Schiffmann and J. VandeVondele, *Wires Comput Mol Sci*, 2014, 4, 15-25.

34. S. Goedecker, M. Teter and J. Hutter, *Phys Rev B*, 1996, 54, 1703-1710.

35. J. VandeVondele and J. Hutter, *Journal of Chemical Physics*, 2007, 127.

36. T. F. Willems, C. Rycroft, M. Kazi, J. C. Meza and M. Haranczyk, *Microporous and Mesoporous Materials*, 2012, 149, 134-141.

37. A. K. Rappé, C. J. Casewit, K. Colwell, W. Goddard and W. Skiff, *Journal of the American Chemical Society*, 1992, 114, 10024-10035.

38. D. Dubbeldam, S. Calero, D. Ellis and R. Snurr, unpublished work.

39. M. Martin and J. Siepmann, *Journal of Physical Chemistry B*, 1998, 102, 2569-2577.

40. C. Wilmer, O. Farha, Y. Bae, J. Hupp and R. Snurr, *Energy & Environmental Science*, 2012, 5, 9849-9856.

CHAPTER 8

OUTLOOK

In this work we have performed a comprehensive assessment of several key assumptions associated with high-throughput computational screening for metal-organic frameworks (MOFs) for separation applications using selective adsorption. We have benchmarked performance of DFT functionals. We have assessed the different point charge assignment methods for MOFs and the state of the experimentally derived MOF structures in the CoRE MOF database. We have quantitatively studied the impact of structure precision on prediction of adsorption properties and began investigating the importance of MOF framework flexibility for adsorption properties. A novel aspect of this work is the data driven approach, considering thousands of diverse materials to better understand the landscape of MOF properties.

8.1 Benchmarking Density Functional Theory Functionals for MOFs

We compiled a test set of chemically diverse MOFs with high accuracy experimentally derived crystallographic structure data. The test set contains MOFs with a range of topologies and elastic properties. We anticipate that this test set will prove useful in a range of benchmarking studies relevant to MOFs. In this work, we have also demonstrated the significance of our test set by assessing the variance in performance of DFT functional for properties where accurate experimental values are available (structure) and unavailable (point charges and elastic properties).

Our results indicate that there is no “one size fits all” functional suitable for accurately predicting the structure and other properties of MOFs. Although the choice of specific functional may be justified in some limited instances, it appears that the choice of functional for efforts aimed at screening large numbers of MOFs can justifiably be made based on computational convenience and availability.

8.2 A Comprehensive Set of High Quality Point Charges for MOFs

We produced a set of high quality point charges for nearly 3,000 experimentally synthesized MOF structures using plane wave DFT calculations and the DDEC charge partitioning method. We have made these charges, the DDEC Point Charge MOF database, publically available. These charges are well suited for modeling adsorption in MOFs. We have compared the CBAC charge assignment approach to thousands of point charges predicted based on structure specific DFT calculations and demonstrated that CBAC charges may not be robust for screening a large MOF database.

We have also demonstrated that charges assigned by the semi-empirical EQeq method can differ drastically from charges calculated with the DDEC method. These discrepancies in point charges can impact the calculated adsorption selectivities for the sample adsorbates we have examined, making the case that whenever possible using charges directly determined from electronic structure calculations such as the ones we have used is preferable to semi-empirical approaches. We anticipate that the publically available dataset of DDEC derived atomic point charges will extend the use of the CoRE MOF structures to answer a range of interesting questions concerning adsorption and diffusion of polar adsorbates in MOFs.

While attempting to assign point charges to the entire CoRE MOF database, we encountered MOF structures that we believe should be reevaluated. Some of these structures have atoms that were too close to one another and resulted in a high initial energy. This could be due to an incorrect initial structure. Other structures resulted in unphysical charges. We believe this is due to incorrect removal of bound solvents during generation of the CoRE MOF database.

We have also demonstrated that point charges are not sensitive to small or large structural changes, given no change in atom coordination. Therefore, we believe it is a worthwhile endeavor to continue to calculate point charges for the remaining MOFs in the CoRE MOF database and further expand the DDEC Point Charge database.

8.3 High-Throughput Computational Screening of MOFs for trace contaminant removal

We have screened each MOF in the DDEC Point Charge MOF database for potential use in the adsorptive removal of tert-butyl mercaptan (TBM) from methane. Our efficient screening procedure has identified hundreds of MOFs with high selectivity and capacity for TBM. These results suggest multiple directions for future experimental efforts, including the identification of some well-known materials as potential candidates for this separation. The observation that our calculations have identified a large number of materials with appealing adsorption selectivities and adsorption capacities for TBM provides a strong basis for continued development of high performance materials for this application.

The high selectivities of MOFs in our study reveal a potential challenge with the application of MOFs for methane storage. In our study, we find that MIL-53 is highly

selective for TBM and most likely for other polar components of natural gas. This selectivity may drastically reduce methane capacity during cyclic adsorption, especially if TBM accumulates over the many cycles in the life time of the material. Zhang et al. have studied the adsorption and shown the accumulation of ethane, propane and butane in some common MOFs[1], but there has yet to be a study on adsorption impact of trace components such as TBM and other polar species such as H_2O and CO_2 in natural gas.

8.4 DFT Optimized Database of Experimentally Derived MOFs

We have produced a diverse set of over 800 DFT optimized MOF structures which is publicly available as a supplement to the CoRE MOF database. We have also assessed the change to the experimentally refined structures upon DFT energy minimization and found a strong correlation between large structural change and presence of solvent during structural analysis. Previous high-throughput computational methods for assessing properties of MOFs have relied on the experimentally derived MOF structure. Such studies have ignored potential structural effects due to solvent removal. We have used a large set of DFT optimized structures to assess the effect of structural changes on adsorption properties of the MOFs. By studying uptake of CH_4 and CO_2 before and after optimization, we have shown that for a majority of MOFs methane uptake is not sensitive to small structural changes. However, we find that for 56% of MOFs CO_2 uptake changed by more than 25% upon minimization of the structure. We found a weak correlation between change in structure and change in uptake. These results indicate that adsorption properties can be dependent in a complex manner on the potential energy landscape of the adsorbate molecule within the structure. We have also shown that almost all structures with a

significant difference in uptake have small pore sizes, signifying the importance of adsorbate interaction with the pore walls.

These results have significant implications for the MOF community. Structure precision is typically ignored in simulation of adsorption in MOFs. Great care should be given to the starting structure. If the MOF structure if obtained with residual solvent present in the pores, the structure should be energy minimized with DFT (if possible) and validated. Therefore, we believe it is worthwhile endeavor to continue energy minimization of the remaining MOF structures in the CoRE MOF database. In our work we have applied the BFGS optimization algorithm for efficiency reasons. We believe that using the conjugate gradient optimizer will increase the convergence success rate for energy minimization of the remaining MOF structures.

We have also found that even if the structure does not change significantly after energy minimization, GCMC calculations in the new energy minimized structure may result in a significantly different uptake values, especially for polar molecules where electrostatic interactions play an important role. For MOFs with pore sizes comparable to the adsorbate, small fluctuations in the pore size can drastically change uptake properties. For such situations, consideration of framework flexibility is essential for a reliable predication of adsorption.

8.5 Impact of Framework Flexibility on Predicted Adsorption Properties of MOFs

We have considered adsorption of methane, CO_2, and binary o-xylene and ethylbenzene in three commonly studied MOFs: UiO66, HKUST-1, and IRMOF-1. Our results indicate that flexibility of the framework does not impact CO_2 or methane uptake in

these MOFs. However, including flexibility can noticeably impact the predicted loading of xylenes as in the case of HKUST-1. Throughout this work we have utilized the snapshot method which uses structures from molecular dynamics of the empty framework.[2] This is an efficient method which we believe can be used to quickly gauge the sensitivity of predicted adsorption properties to incorporation of framework selectivity. However, assumes that the framework flexibility is decoupled from the adsorbate. It is also important to consider a coupled interaction between the framework and adsorbate to better understand the important of MOF flexibility on prediction of adsorption behavior. To more reliably study adsorption properties, especially in a high-throughput manner, the MOF community must development a range of computationally inexpensive methods to incorporate framework flexibility in adsorption calculations.

8.6 References

1. J. A. Gee and D. S. Sholl, Journal of Physical Chemistry C, 2016, 120, 370-376.
2. Zhang, H.; Deria, P.; Farha, O. K.; Hupp, J. T.; Snurr, R. Q., *Energy & Environmental Science* 2015, 8, (5), 1501-1510.

APPENDIX A

DETAILED RESULTS FOR BENCHMARKING OF DFT FUNCTIONALS FOR MOFS

A.1 Additional Computational Details and Results

Our studies show that results for the mechanical properties for DEMLIR are sensitive to the number of processors used for the calculations. Each calculation for DEMLIR has been tested along four differently compiled versions of VASP, using version 5.2.12 and 5.3.5 and two different computing environments. We've found that result are reproducible as long as the same number of processors are used. Energy and geometry optimization calculations are not effected by parallelization. For our study, DEMLIR mechanical properties were calculated using 32 processors.

Table A. 1: MOF primitive unit cell size and computational parameter setup. An energy cut off of 520 eV was used for all calculations.

REFCODE	Chemical Formula	Experimental Lattice Parameters (Å)			Kpoints	Comments
		a	b	c		
QEJZUB01[1]	$Cu_3H_4C_{10}O_{10}$	6.77	6.89	12.36	4 x 4 x 2	
HOGWAB[2]	$Fe_4H_4C_4O_{12}$	5.54	5.93	7.27	4 x 4 x 4	
HAWVOQ01[3]	$Co_2C_8N_{12}$	5.97	7.06	7.41	4 x 4 x 4	
RORQOE[4]	$Ag_4C_{12}Cl_4O_8$	5.29	6.34	11.40	6 x 4 x 2	
OFUWIV01[5]	$Zn_1H_4C_4O_4$	4.83	4.83	6.25	6 x 6 x 4	
MURCEH[6]	$Cu_8H_8C_8N_{12}Cl_8$	5.02	5.81	19.25	4 x 4 x 2	Antiferromagnetic: see below for spin states f
WAJJAU[7]	$Li_{32}Zn_{32}H_{24}C_{72}O_{96}$	11.28	16.34	16.34	2 x 2 x 2	For PBE-D2 (Li: C6 = 31.47 $\frac{Jnm^6}{mol}$ Ro = 2.077 Å)
PIJGEV[8]	$Cd_2H_{10}C_{16}N_4O_{10}$	7.55	7.64	8.47	4 x 4 x 4	
KOMJEC[9]	$Sm_2H_{12}C_{10}O_{14}$	6.76	7.67	8.05	4 x 4 x 4	For PBE-D2 (Sm: C6 =33.98 $\frac{Jnm^6}{mol}$ Ro = 2.226 Å)
YORSII[10]	$Dy_2H_{12}C_{12}N_2O_{16}$	6.74	7.81	9.17	4 x 4 x 2	
DEMLIR[11]	$Fe_4P_4H_{16}C_8O_{24}$	6.61	8.36	9.62	4 x 4 x 2	Antiferromagnetic: see below for spin states

Fractional coordinates of Cu atoms and corresponding initial spin state in MURCEH

0.000000000	0.500000000	0.500000000	-2
0.000000000	0.500000000	0.000000000	-2
0.812179983	0.957530022	0.437770009	2
0.812179983	0.957530022	0.937770009	2
0.187820002	0.042470001	0.062229998	-2
0.187820002	0.042470001	0.562229991	2

Fractional coordinates of Fe atoms and corresponding initial spin state in DEMLIR

0.023400	0.511260	0.402520	2
0.476600	0.488740	0.902520	-2
0.976600	0.011260	0.097480	-2
0.523400	0.988740	0.597480	2

The following results (A.2 – A.7) represent the mean absolute deviation (MAD) of structural properties calculated for the DFT minimized structure from the experimental structure. Averaging is performed per structure. MAD is defined as

$$MAD_f = \sum_i^N \frac{abs(x_{exp,i} - x_i)}{N} \quad \text{(A.1)}$$

where f is the functional of interest, N is the total number of bond length, angles, or torsions considered for a MOF, $x_{exp,i}$ is the measured value for the experimental structure and x_i is the measured value for the DFT predicted structure.

Table A. 2: MAD of Δ in lattice parameters (Å) by MOF

	M06L	PBE	PW91	PBE-D2	PBE-D3	vdw-DF2
RORQOE (Ag)	**0.59**	**0.58**	**0.57**	**0.27**	**0.02**	**0.20**
PIJGEV (Cd)	**0.25**	**0.25**	**0.20**	**0.03**	**0.07**	**0.16**
HAWVOQ01 (Co)	**0.37**	**0.41**	**0.42**	**0.21**	**0.18**	**0.09**
QEJZUB01 (Cu I)	**0.24**	**0.24**	**0.24**	**0.11**	**0.16**	**0.16**
MURCEH (Cu II)	**0.16**	**0.17**	**0.16**	**0.05**	**0.07**	**0.21**
YORSII (Dy)	**0.12**	**0.15**	**0.11**	**0.04**	**0.05**	**0.11**
HOGWAB (Fe)	**0.17**	**0.17**	**0.18**	**0.08**	**0.06**	**0.23**
DEMLIR (Fe)	**0.15**	**0.12**	**0.13**	**0.21**	**0.21**	**0.06**
KOMJEC (Sm)	**0.18**	**0.18**	**0.18**	**0.09**	**0.06**	**0.12**
OFUWIV01 (Zn)	**0.16**	**0.16**	**0.16**	**0.03**	**0.09**	**0.10**
GUPCUQ01 (Cd)	**0.30**	**0.30**	**0.28**	**0.10**	**0.14**	**0.32**
WAJJAU (Li Zn)	**0.14**	**0.16**	**0.16**	**0.07**	**0.06**	**0.40**

Table A. 3: MAD of Δ in bond length (Å) by MOF

	M06L	PBE	PW91	PBE-D2	PBE-D3	vdw-DF2
RORQOE (Ag)	**0.076**	**0.074**	**0.064**	**0.028**	**0.015**	**0.078**
PIJGEV (Cd)	**0.062**	**0.062**	**0.055**	**0.022**	**0.033**	**0.077**
HAWVOQ01 (Co)	**0.213**	**0.208**	**0.203**	**0.186**	**0.198**	**0.182**
QEJZUB01 (Cu I)	**0.112**	**0.112**	**0.109**	**0.051**	**0.050**	**0.064**
MURCEH (Cu II)	**0.032**	**0.028**	**0.035**	**0.009**	**0.014**	**0.064**
YORSII (Dy)	**0.024**	**0.035**	**0.023**	**0.022**	**0.025**	**0.045**
HOGWAB (Fe)	**0.085**	**0.085**	**0.083**	**0.052**	**0.051**	**0.030**
DEMLIR (Fe)	**0.033**	**0.065**	**0.068**	**0.075**	**0.076**	**0.036**
KOMJEC (Sm)	**0.026**	**0.027**	**0.026**	**0.011**	**0.015**	**0.056**
OFUWIV01 (Zn)	**0.038**	**0.038**	**0.034**	**0.023**	**0.041**	**0.054**
GUPCUQ01 (Cd)	**0.051**	**0.053**	**0.047**	**0.023**	**0.032**	**0.080**
WAJJAU (Li Zn)	**0.029**	**0.024**	**0.028**	**0.023**	**0.021**	**0.073**

Table A. 4: MAD of Δ in bond angle (°) by MOF

	M06L	PBE	PW91	PBE-D2	PBE-D3	vdw-DF2
RORQOE (Ag)	**4.76**	**4.72**	**4.78**	**3.67**	**0.55**	**1.48**
PIJGEV (Cd)	**2.14**	**2.08**	**1.80**	**1.17**	**1.17**	**0.65**
HAWVOQ01 (Co)	**0.93**	**0.95**	**0.98**	**0.36**	**0.44**	**0.64**
QEJZUB01 (Cu I)	**2.95**	**2.96**	**2.88**	**0.77**	**0.53**	**2.60**
MURCEH (Cu II)	**1.82**	**1.85**	**2.39**	**1.06**	**0.91**	**1.37**
YORSII (Dy)	**1.95**	**2.07**	**2.01**	**2.15**	**1.37**	**1.20**
HOGWAB (Fe)	**1.88**	**1.88**	**2.14**	**3.43**	**3.13**	**5.17**
DEMLIR (Fe)	**1.09**	**1.62**	**1.73**	**1.97**	**1.94**	**1.74**
KOMJEC (Sm)	**2.40**	**2.34**	**2.40**	**1.32**	**1.17**	**1.50**
OFUWIV01 (Zn)	**2.24**	**2.24**	**2.35**	**0.86**	**1.01**	**0.97**
GUPCUQ01 (Cd)	**0.52**	**0.74**	**0.47**	**1.35**	**1.40**	**2.39**
WAJJAU (Li Zn)	**0.83**	**0.69**	**0.56**	**0.99**	**1.02**	**1.39**

Table A. 5: MAD of Δ in torsion angle (°) by MOF

	M06L	PBE	PW91	PBE-D2	PBE-D3	vdw-DF2
RORQOE (Ag)	**9.37**	**9.27**	**9.39**	**7.28**	**1.06**	**2.21**
PIJGEV (Cd)	**5.78**	**5.67**	**4.86**	**3.91**	**2.84**	**2.42**
HAWVOQ01 (Co)	**11.21**	**14.73**	**13.24**	**8.13**	**7.72**	**6.79**
QEJZUB01 (Cu I)	**6.18**	**3.95**	**5.83**	**7.87**	**7.55**	**5.94**
MURCEH (Cu II)	**12.90**	**11.38**	**6.73**	**12.93**	**8.11**	**11.63**
YORSII (Dy)	**8.54**	**8.58**	**8.85**	**6.57**	**7.14**	**5.09**
HOGWAB (Fe)	**2.15**	**2.15**	**2.80**	**4.78**	**4.30**	**7.92**
DEMLIR (Fe)	**3.43**	**8.78**	**8.79**	**11.48**	**10.74**	**8.98**
KOMJEC (Sm)	**10.87**	**10.83**	**10.87**	**4.17**	**3.95**	**5.62**
OFUWIV01 (Zn)	**5.05**	**5.05**	**4.92**	**2.78**	**2.83**	**4.20**
GUPCUQ01 (Cd)	**1.14**	**1.27**	**1.08**	**1.63**	**1.75**	**2.16**
WAJJAU (Li Zn)	**1.52**	**1.83**	**1.70**	**1.44**	**1.27**	**4.04**

Table A. 6: Δ in PLD (Å) by MOF

	M06L	PBE	PW91	PBE-D2	PBE-D3	vdw-DF2
RORQOE (Ag)	**0.20**	**0.20**	**0.20**	**-0.20**	**-0.01**	**0.13**
PIJGEV (Cd)	**0.13**	**0.13**	**0.06**	**0.01**	**-0.03**	**-0.01**
HAWVOQ01 (Co)	**0.33**	**0.20**	**0.36**	**-0.30**	**-0.28**	**-0.22**
QEJZUB01 (Cu I)	**0.11**	**0.11**	**0.10**	**-0.11**	**-0.10**	**-0.25**
MURCEH (Cu II)	**0.15**	**0.16**	**0.16**	**-0.03**	**0.02**	**0.08**
YORSII (Dy)	**0.14**	**0.15**	**0.15**	**-0.03**	**0.02**	**0.07**
HOGWAB (Fe)	**-0.17**	**-0.18**	**-0.17**	**-0.32**	**-0.32**	**-0.41**
DEMLIR (Fe)	**0.06**	**-0.10**	**-0.11**	**-0.23**	**-0.20**	**-0.13**
KOMJEC (Sm)	**0.09**	**0.09**	**0.09**	**-0.15**	**-0.13**	**-0.09**
OFUWIV01 (Zn)	**0.18**	**0.18**	**0.18**	**-0.11**	**-0.05**	**-0.05**
GUPCUQ01 (Cd)	**0.07**	**0.08**	**0.08**	**-0.02**	**-0.01**	**-0.01**
WAJJAU (Li Zn)	**0.04**	**0.01**	**0.03**	**-0.04**	**-0.08**	**0.22**

Table A. 7: Δ in LCD (Å) by MOF

	M06L	PBE	PW91	PBE-D2	PBE-D3	vdw-DF2
RORQOE (Ag)	**0.28**	**0.28**	**0.28**	**-0.03**	**0.00**	**0.09**
PIJGEV (Cd)	**-0.01**	**-0.02**	**-0.07**	**0.06**	**0.07**	**0.10**
HAWVOQ01 (Co)	**0.27**	**0.40**	**0.23**	**-0.24**	**-0.22**	**-0.11**
QEJZUB01 (Cu I)	**0.18**	**0.18**	**0.18**	**0.00**	**0.01**	**-0.10**
MURCEH (Cu II)	**0.15**	**0.14**	**0.14**	**-0.11**	**-0.09**	**0.06**
YORSII (Dy)	**0.01**	**-0.03**	**-0.04**	**-0.30**	**-0.24**	**-0.14**
HOGWAB (Fe)	**0.06**	**0.06**	**0.06**	**-0.06**	**-0.02**	**-0.10**
DEMLIR (Fe)	**0.11**	**-0.03**	**-0.04**	**-0.09**	**-0.09**	**-0.03**
KOMJEC (Sm)	**0.05**	**0.04**	**0.04**	**0.15**	**0.17**	**0.09**
OFUWIV01 (Zn)	**0.23**	**0.23**	**0.22**	**-0.17**	**-0.12**	**-0.12**
GUPCUQ01 (Cd)	**0.21**	**0.24**	**0.21**	**-0.05**	**-0.02**	**0.09**
WAJJAU (Li Zn)	**0.04**	**0.10**	**0.03**	**0.10**	**0.04**	**0.20**

Table A. 8: Angles of the experimental crystal structures considered for three example MOFs in the test set.

HOGWAB				RORQOE				HAWVOQ01			
O	Fe	O	78.47	Cl	Ag	O	68.37	N	Co	N	94.86
O	Fe	O	73.86	Cl	Ag	O	74.94	N	Co	N	85.14
O	Fe	O	88.31	Cl	Ag	O	135.63	N	Co	N	91.05
O	Fe	O	161.34	Cl	Ag	O	137.90	N	Co	N	88.95
O	Fe	O	87.09	O	Ag	O	110.23				
O	Fe	O	152.01	O	Ag	O	108.82				
O	Fe	O	93.86	O	Ag	O	139.57				
O	Fe	O	87.34	O	Ag	O	137.82				
O	Fe	O	88.92	O	Ag	O	65.96				
O	Fe	O	89.51	O	Ag	O	74.16				
O	Fe	O	120.59								
O	Fe	O	85.59								
O	Fe	O	80.54								
O	Fe	O	174.05								
O	Fe	O	104.87								

Table A. 9: Minimum Young's modulus for MOFs in the test set (GPa)

MOF	M06	PBE	PW91	PBE-D2	PBE-D3	vdw-DF2
RORQOE (Ag)	22.7	19.6	20.7	16.5	17.1	17.9
PIJGEV (Cd)	102.1	98.1	99.4	96.6	100.3	103.7
HAWVOQ01 (Co)	23.2	19.0	21.8	21.4	20.7	17.2
QEJZUB01 (Cu I)	46.1	36.3	36.5	35.0	33.9	40.8
MURCEH (Cu II)	48.1	48.2	48.6	48.3	48.2	47.1
YORSII (Dy)	143.9	141.4	141.5	140.5	140.8	150.2
HOGWAB (Fe)	67.0	67.7	67.9	64.8	66.4	81.2
DEMLIR (Fe)	184.9	185.1	168.3	184.2	184.2	179.6
KOMJEC (Sm)	146.0	145.0	145.0	141.1	144.4	156.4
OFUWIV01 (Zn)	111.4	110.2	110.7	110.4	111.4	110.4

Table A. 10: Maximum Young's modulus for MOFs in the test set (GPa)

MOF	M06	PBE	PW91	PBE-D2	PBE-D3	vdw-DF2
RORQOE (Ag)	284.9	281.4	284.5	282.5	283.4	285.3
PIJGEV (Cd)	406.7	403.5	403.2	401.7	404.7	405.4
HAWVOQ01 (Co)	482.1	461.2	466.8	464.9	468.6	461.4
QEJZUB01 (Cu I)	361.3	359.5	353.7	361.8	354.9	362.8
MURCEH (Cu II)	430.7	425.4	428.3	425.1	434.2	437.9
YORSII (Dy)	340.7	340.2	339.9	337.3	337.9	343.1
HOGWAB (Fe)	461.4	460.1	460.8	461.9	453.3	468.5
DEMLIR (Fe)	351.1	352.8	339.5	354.2	354.2	342.8
KOMJEC (Sm)	432.0	431.4	431.4	427.8	431.3	430.6
OFUWIV01 (Zn)	379.3	380.4	379.8	380.6	380.2	376.6

Table A. 11: Minimum linear compressibility for MOFs in the test set (TPa-1)

MOF	M06	PBE	PW91	PBE-D2	PBE-D3	vdw-DF2
RORQOE (Ag)	-20.6	-25.3	-23.4	-31.1	-29.9	-28.5
PIJGEV (Cd)	0.7	0.7	0.7	0.7	0.7	0.8
HAWVOQ01 (Co)	-3	-3.6	-3.4	-3.5	-3.5	-3.2
QEJZUB01 (Cu I)	1.1	1.2	1.3	1.2	1.4	1.1
MURCEH (Cu II)	0.9	1.1	0.9	1.1	0.9	0.9
YORSII (Dy)	1.1	1.1	1.1	1.1	1.1	1.1
HOGWAB (Fe)	1.0	1.0	1.0	0.9	1.0	1.1
DEMLIR (Fe)	0.9	0.8	1.027	0.8	0.8	0.9
KOMJEC (Sm)	0.8	0.7	0.7	0.7	0.8	0.8
OFUWIV01 (Zn)	1.0	1.0	1.0	1.0	1.0	1.0

Table A. 12: Maximum linear compressibility for MOFs in the test set (TPa^{-1})

MOF	M06	PBE	PW91	PBE-D2	PBE-D3	vdw-DF2
RORQOE (Ag)	**31.7**	**38**	**36.1**	**46**	**44.4**	**40.3**
PIJGEV (Cd)	**5.6**	**5.9**	**5.8**	**6**	**5.7**	**5.4**
HAWVOQ01 (Co)	**21.2**	**26.2**	**22.9**	**24.5**	**25**	**25**
QEJZUB01 (Cu I)	**11.1**	**14**	**13.2**	**15.1**	**15**	**10.8**
MURCEH (Cu II)	**3.6**	**3.5**	**3.6**	**3.6**	**3.7**	**3.4**
YORSII (Dy)	**4.3**	**4.4**	**4.4**	**4.4**	**4.4**	**4**
HOGWAB (Fe)	**10.8**	**10.4**	**10.4**	**11**	**10.8**	**8.6**
DEMLIR (Fe)	**2.6**	**2.5**	**3.1**	**2.6**	**2.6**	**2.8**
KOMJEC (Sm)	**3.6**	**3.6**	**3.6**	**3.7**	**3.6**	**3.3**
OFUWIV01 (Zn)	**4.4**	**4.5**	**4.5**	**4.4**	**4.4**	**4.4**

Table A. 13: Minimum shear modulus for MOFs in the test set (GPa)

MOF	M06	PBE	PW91	PBE-D2	PBE-D3	vdw-DF2
RORQOE (Ag)	7.5	6.4	6.9	5.4	5.6	5.7
PIJGEV (Cd)	43.4	42.3	42.7	41.7	43.0	44.6
HAWVOQ01 (Co)	8.6	7.3	8.2	8.3	8.0	6.1
QEJZUB01 (Cu I)	14.0	10.9	10.9	10.6	10.2	12.0
MURCEH (Cu II)	15.1	15.3	15.3	15.2	15.2	14.9
YORSII (Dy)	60.2	59.5	59.5	59.2	59.6	62.2
HOGWAB (Fe)	35.3	35.0	35.2	34.1	34.8	40.1
DEMLIR (Fe)	79.2	79.1	72.2	79.4	79.4	76.1
KOMJEC (Sm)	56.2	55.8	55.8	54.3	55.6	59.1
OFUWIV01 (Zn)	44.5	44.4	44.5	44.1	44.5	43.4

Table A. 14: Maximum shear modulus for MOFs in the test set (GPa)

MOF	M06	PBE	PW91	PBE-D2	PBE-D3	vdw-DF2
RORQOE (Ag)	**112.5**	**111.9**	**112.8**	**112.6**	**112.4**	**112.9**
PIJGEV (Cd)	**162.3**	**161.2**	**161.4**	**160.5**	**161.4**	**162.2**
HAWVOQ01 (Co)	**126.0**	**126.7**	**127.5**	**127.1**	**126.3**	**123.4**
QEJZUB01 (Cu I)	**149.4**	**147.8**	**147.5**	**149.3**	**148.0**	**149.2**
MURCEH (Cu II)	**172.1**	**171.2**	**170.2**	**171.9**	**173.1**	**176.0**
YORSII (Dy)	**137.9**	**137.6**	**137.6**	**137.0**	**138.1**	**141.3**
HOGWAB (Fe)	**136.8**	**127.1**	**127.4**	**129.0**	**127.0**	**132.9**
DEMLIR (Fe)	**144.5**	**144.3**	**143.1**	**144.8**	**144.8**	**142.6**
KOMJEC (Sm)	**155.8**	**155.1**	**155.1**	**153.2**	**154.3**	**160.0**
OFUWIV01 (Zn)	**157.0**	**156.7**	**156.6**	**156.5**	**157.7**	**156.1**

Table A. 15: Minimum Poisson ration for MOFs in the test set

MOF	M06	PBE	PW91	PBE-D2	PBE-D3	vdw-DF2
RORQOE (Ag)	-1.16	-1.30	-1.25	-1.46	-1.43	-1.40
PIJGEV (Cd)	-0.35	-0.36	-0.35	-0.37	-0.35	-0.32
HAWVOQ01 (Co)	-0.79	-0.89	-0.82	-0.81	-0.82	-1.03
QEJZUB01 (Cu I)	-0.39	-0.50	-0.48	-0.54	-0.54	-0.39
MURCEH (Cu II)	-0.82	-0.81	-0.81	-0.82	-0.83	-0.85
YORSII (Dy)	-0.09	-0.09	-0.09	-0.09	-0.08	-0.06
HOGWAB (Fe)	-0.43	-0.39	-0.39	-0.43	-0.40	-0.31
DEMLIR (Fe)	0.02	0.03	-0.04	0.02	0.02	-0.02
KOMJEC (Sm)	-0.03	-0.03	-0.03	-0.04	-0.03	-0.03
OFUWIV01 (Zn)	-0.04	-0.05	-0.05	-0.04	-0.04	-0.06

Table A. 16: Maximum Poisson ration for MOFs in the test set

MOF	M06	PBE	PW91	PBE-D2	PBE-D3	vdw-DF2
RORQOE (Ag)	1.70	1.83	1.78	2.01	1.97	1.94
PIJGEV (Cd)	0.78	0.79	0.78	0.78	0.78	0.77
HAWVOQ01 (Co)	1.74	2.04	1.84	1.85	1.88	2.18
QEJZUB01 (Cu I)	0.85	0.88	0.89	0.89	0.90	0.88
MURCEH (Cu II)	1.43	1.43	1.42	1.43	1.44	1.49
YORSII (Dy)	0.53	0.54	0.54	0.53	0.53	0.52
HOGWAB (Fe)	0.69	0.70	0.69	0.72	0.69	0.64
DEMLIR (Fe)	0.44	0.45	0.40	0.46	0.46	0.43
KOMJEC (Sm)	0.59	0.60	0.60	0.60	0.60	0.60
OFUWIV01 (Zn)	0.61	0.61	0.61	0.61	0.61	0.62

Table A. 17: The difference between MAD of vdw-DF2 and PBE-D2 for lattice parameters, bond lengths, Bond Angles and Torsion Angles. Negatives values are highlighted indicate that vdw-DF2 more accurately measured that property. Structures highlighted in red represent MOFs with little difference and highlighted in green represent MOFs with higher differences in predicted charges with vdw-DF2 and PBE and structures. We do not find a strong correlation between charge transfer predicted by vdw-DF2 and better prediction of structural parameters compared to PBE-D2

	Lattice	Bond Length	Bond Angle	Torsion Angle
RORQOE (Ag)	-0.07	0.036	0.63	2.11
PIJGEV (Cd)	0.13	0.033	0.62	0.95
HAWVOQ01 (Co)	-0.12	0.017	2.11	6.21
QEJZUB01 (Cu I)	0.05	0.058	1.02	-0.09
MURCEH (Cu II)	0.12	0.026	-0.14	2.21
YORSII (Dy)	0.07	0.001	-1.29	2.28
HOGWAB (Fe II)	0.15	0.031	-0.2	-1.98
DEMLIR (Fe III)	-0.01	0.013	0.62	-0.60
KOMJEC (Sm)	-0.01	0.015	1.49	6.7
OFUWIV01 (Zn)	0.07	0.011	-0.88	2.14
GUPCUQ01 (Cd)	0.04	0.024	-0.43	-0.55

A.2 References

1. W. Ouellette, A. V. Prosvirin, V. Chieffo, K. R. Dunbar, B. Hudson and J. Zubieta, *Inorganic Chemistry*, 2006, **45**, 9346-9366.
2. M. Molinier, D. J. Price, P. T. Wood and A. K. Powell, *J Chem Soc Dalton*, 1997, DOI: Doi 10.1039/A704400c, 4061-4068.
3. M. Kurmoo and C. J. Kepert, *New J Chem*, 1998, **22**, 1515-1524.
4. W. Frenzer, R. Wartchow and H. Bode, *Zeitschrift Fur Kristallographie*, 1997, **212**, 237-237.
5. T. A. Bowden, H. L. Milton, A. M. Z. Slawin and P. Lightfoot, *Dalton Transactions*, 2003, DOI: Doi 10.1039/B211181k, 936-939.
6. R. Cao, Q. Shi, D. F. Sun, M. C. Hong, W. H. Bi and Y. J. Zhao, *Inorganic Chemistry*, 2002, **41**, 6161-6168.
7. L. H. Xie, J. B. Lin, X. M. Liu, Y. Wang, W. X. Zhang, J. P. Zhang and X. M. Chen, *Inorganic Chemistry*, 2010, **49**, 1158-1165.
8. C. C. Wang, C. T. Kuo, J. C. Yang, G. H. Lee, W. J. Shih and H. S. Sheu, *Cryst Growth Des*, 2007, **7**, 1476-1482.
9. X. J. Zhang, Y. H. Xing, J. Han, X. Q. Zeng, M. F. Ge and S. Y. Niu, *Cryst Growth Des*, 2008, **8**, 3680-3688.
10. X. J. Kong, G. L. Zhuang, Y. P. Ren, L. S. Long, R. B. Huang and L. S. Zheng, *Dalton Transactions*, 2009, DOI: Doi 10.1039/B819792j, 1707-1709.
11. J. J. Hou and X. M. Zhang, *Cryst Growth Des*, 2006, **6**, 1445-1452.

APPENDIX B

HERE IS THE TITLE OF APPENDIX A

B.1 Additional Computational Details

Table B. 1: List of grid type and subdivisions of the brillouin zone for each dft calculations using Gamma.

ACUBAB	NUVYOT	DORDUK	SEQSOY	ITETEH	VOTMAS	IBICUT	GAXKOH
AJAYIT	OBUBOC	ECAHAT	SOXHUI	JETNOL	VUHJAK	IBIDAA	FUSYUO
AVEROJ	ODIMAQ	ECOSIY	TAKYOV	JUCXEK	WAHMEY01h	IGAHAB	FANWOI
BEPMAM	ODOXEK	EMANAH	TAPXIT01	KIYMIQ	WEMXIX	ILUGOM	CUVTUJ
BEPMEQ	OJICUG	EXOTUH	VACFOV01	KOFPEB	WEVQOD	ILUHUT	CUIMDZ01h
BEPMIU	ONIXOZ	FAKMAH	VACFOV	KOFPEB02	WEZCIO	ILUJAB	COXQUB
BEPNIV	PAPPIH	FALQEQ	VACFUB01	KOFPEB05	WUTBIW	ILUJEF	CODRUJ
BEXPAX	PAPRUU	FALQOA	VACFUB	LAGBUS	XADCOW	ILUJIJ	CODROD
BOMCUB	PARNON	FEXCES	VARREL	LAGCUT	XAKQIL	JAHNEM	CIGFEF
CERMIV	PELGOE	FIVYEP01	VARRIP	LAGHIL	XIPBII	JEBCOJ	CAXWIJ
DOTTUC	PUQXUV	GADMAA	WUTBES	LAJDUV	XOVVOU	JOGBIR	CAXWEF
DOTWAL	RAVWAO	GAYFUJ	YIWPEZ	LAJDUV01	XUNJEW	KANCIN	CAXWAB
ILIGEP	VOCXUH	IBICON	HOMZEP	BIYTEJ	PAPPED	NUCREJ	MIL-88C-dry
GELVID01	DEQFOU	LAJDUV02	YARGAB	KANMIX	CAXVUU	COF-1	RIVDEF
GERPUP	DAXHUH01	LAJDUV03	YAZWOM	KIGCEK	CAXVOO	COF-5	RONCIG
HAMREU	DAVYEG	LEDLEN	YUKBIP01	KOFPEB03	CAXVII	CEFLEF	RUCGOM
HEBZAR	CILDAD	ATOTIM	ZILBAZ	KUDLUR	CADPII	PEKKAS	SERKAC
HEBZEV	CAYSOK	BANMAG	MAZJEC	LAGCED	BUVXOG	NUVWIL	SERKEG
HIGRIA	BUVYIB	BARZUR	NABMUA	LARVIL	BENXUP	MIL-88C-open	SETSIV
HIHJUF	ATIJUJ	BEPLUF	NABMUA01	LOQLEJ	BELYIC	IBICED	TAPXIT
HOGLEV01	ANUGUM	BEPNOB	NOCLOH01	MURCIL	BAHGUN	IBICIH	TUVDIX
HOGTOM	ANOMUM	BEPNUH	NOCLOH02	MURCOR	BAHGUN04	ILIFOY	TUVDUJ
HUTZAX01	AMAFOK	BEPPAP	NOCLOH03	NALYEG	BAHGUN01	ILIFUE	UJEDIX
IBARUA	AFOVOH	BEPPIX	NOCLOH	NANMEW	MIL-88A-dry	ILIGAL	VATXEU
IBASEL	PUQYAC	BEPPOD	OFESAU	NIJZIP01	MIL-88A-open	HAMRIY	VECWUX
IBICAZ	KATDAM	BICDAU	OFESIC	NIJZOV	MIL-88B-dry	HURQUG	
FAKLIO	FAKLOU	FIVYEP	GELVEZ	GELVEZ02	GELVID	REGQUR	

APPENDIX C

ADDITIONAL GCMC RESULTS

C.1 Additional Adsorption Analysis

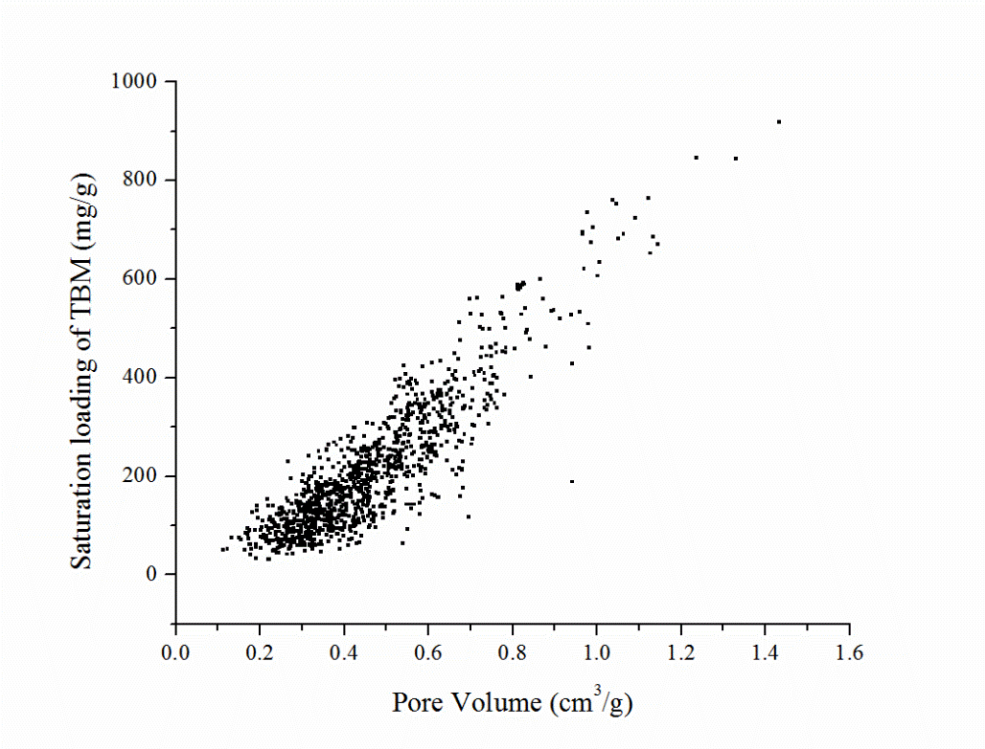

Figure C. 1: TBM saturation loading from single component GCMC simulations versus gravimetric pore volume.

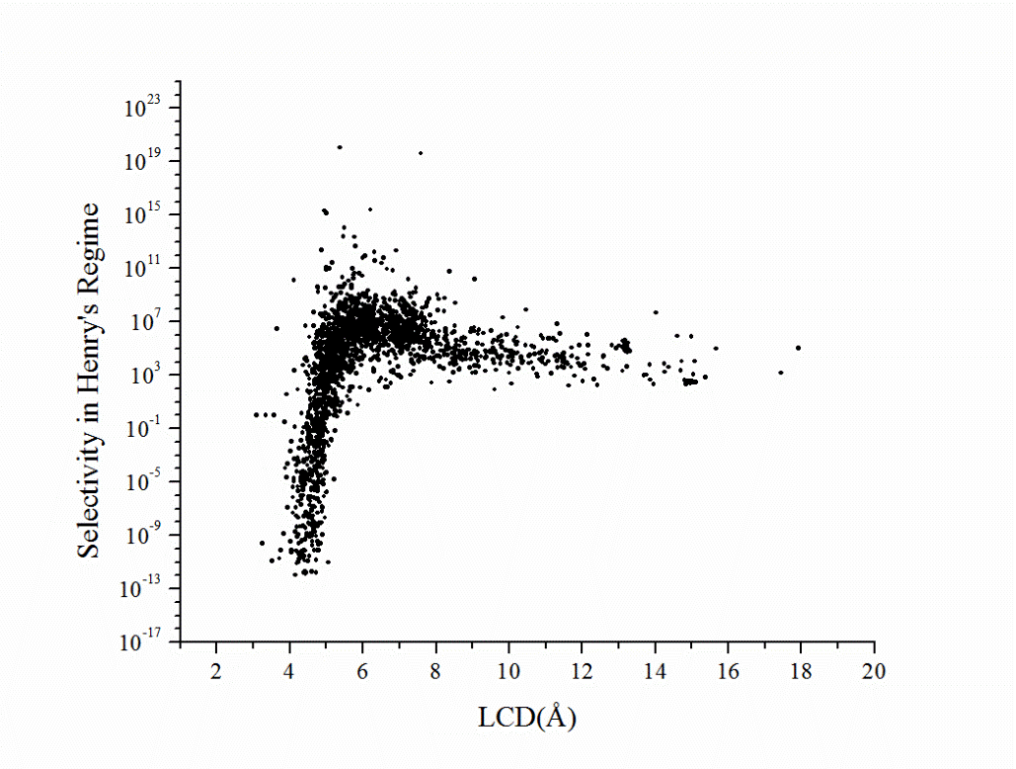

Figure C. 2: Henry's regime selectivity versus largest cavity diameter (LCD).

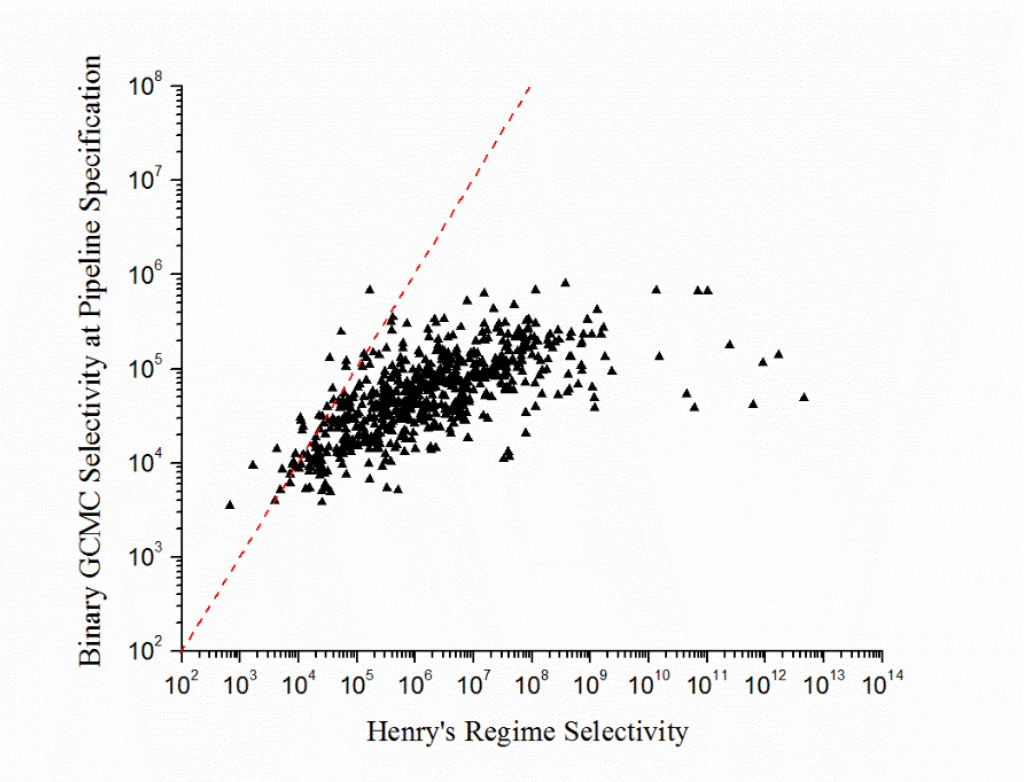

Figure C. 3: Binary GCMC selectivity at a representative pipeline composition of natural gas (10 ppm TBM in CH4, 18.1 atm) vs. Henry's regime selectivity for 654 structures.

APPENDIX D

COMPUTATIONAL DETAILS

D.1 Additional Computational Details

Basis set for Lanthanum prepared for use in CP2K:

```
La DZVP-MOLOPT-SR-GTH DZVP-MOLOPT-SR-GTH-q11
 1
 2 0 3 7 3 2 2 1
      2.61043358  0.35199091  0.10272260 -0.06808113 -0.15151046
0.13381188  0.07768261 -0.04502434  0.56108153
      1.97548354 -0.60467225 -0.25822195  0.15310013  0.39322808 -
0.41126147 -0.24128689  0.08813749 -0.67966568
      1.37683237 -0.12976539  0.21539666  0.05799973 -0.18082295
0.15710279  0.17606169 -0.16037691  0.42347127
      0.50317401  0.38709867 -0.03637620 -0.61681449  0.01304460
0.76568902  0.24859282  0.69197494  0.07320467
      0.21379586  0.29290169 -0.25270638 -0.06902891 -0.40402320
0.24356893  0.69804651  0.32599357  0.19414921
      0.08361942  0.48342794  0.12965143  0.75484782 -0.67849916 -
0.31853420  0.56934571 -0.49399811  0.02544931
      0.03181016 -0.15586999  0.89128029 -0.11636537 -0.40737349 -
0.20299666  0.17755680 -0.36789751  0.01461982
```

Trappe[1] force field used for CO_2:

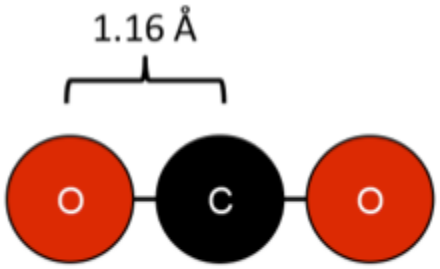

σ (Å)	3.05	2.80	3.05
ε/k_B (K)	79.0	27.0	79.0
q (e)	-0.35	+0.70	-0.35

Structures used in study of DDEC Charges:

ABUWOJ_clean	CATART03_clean	CUNXIS10_clean	FOHCIP_clean	HEBKEG_clean
AGARUW_clean	CEGDUO_clean	DEGJIK_clean	FUNCEX_clean	HOWPOZ_clean
AMUCOB_clean	CEGFAW_clean	EBEMEF_clean	GEHSAN_clean	IBUDOZ_clean
APEBED_clean	CEGWER_clean	EBEMII_clean	GIDKOU_clean	ICEGED_clean
BALMUW01_clean	CESYEF_clean	ECODEG_clean	GIMSIG_clean	JIVFUQ_clean
BONWAD_clean	CESYEF01_clean	EGEJIK_manual	GUYLOC_clean	KAYBIX_clean
BOWQAG_clean	CICYIX_clean	EKOPIE_clean	GUYMAP_clean	KAYBUJ_clean
BUDDIO_clean	COYTEQ_clean	EZUCIM_clean	HAFQUC_clean	KEXKAB_clean
BUKMUQ_clean	CUNXIS_clean	FEFDAX_clean	HAKWUM_clean	KEXKEF_clean

KINKAV_clean	MATVEJ_clean	PUSDOX_clean	RATDAS02_clean	SUHHOT_clean
LABJUV_clean	NADZEZ_clean	QATHOK_clean	RAXDAX_clean	TARWAK_clean
LAGNOY_clean	NAKLIW_clean	QEKLID01_clean	REGLOG_clean	TESGOO_clean
LELMIA01_clean	NARTUX_clean	QIFLIC_clean	RUFMUA01_clean	TESGUU_clean
LENRUS_clean	NASCIV_clean	QOJVAM_clean	RURPEA_clean	TEVZEA_clean
LIKFOB_clean	OFODAP_clean	QOKCID_clean	RUVMAX_clean	TEVZOK_clean
LUFQUZ02_clean	PAKXIK_clean	QOMDUS_clean	SEFBOV_clean	
MADVUJ_clean	PAPXUB_clean	QUGBUQ_clean	SETFUT_clean	
MATTUX_clean	PORVUO_clean	QUPHUF_clean	SEYDUW_clean	

AIMD calculation details:

All AIMD calculations were carried out using the Gaussian plane-wave (GPW) computational package CP2K 2.6[2] on the Argonne National Laboratories supercomputer

MIRA. We have chosen to use the Gordecker, Teter, Hutter dual-space pseudopotentials (GTH)[3] with the PBE functional, 650 Ry cutoff, and double-zeta valance polarized (DZVP)[4] basis sets. Simulations were performed in the NPT ensemble at 300 K (Nose thermostat) and 1 bar, using a 1 fs timestep.

Heat of adsorption and uptake of CO_2 in HKUST-1 at 1 bar and 298 K using the snapshot method.

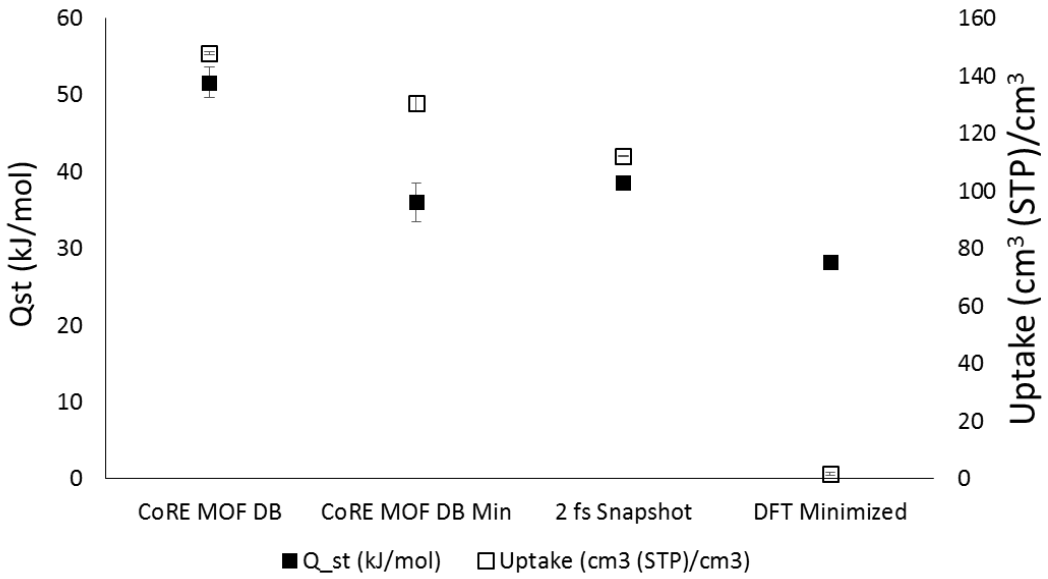

D.2 References

1. Martin, M.; Siepmann, J., *Journal of Physical Chemistry B* 1998, *102* (14), 2569-2577.

2. Hutter, J.; Iannuzzi, M.; Schiffmann, F.; VandeVondele, J., *Wires Comput Mol Sci* 2014, *4* (1), 15-25.
3. Goedecker, S.; Teter, M.; Hutter, J., *Phys Rev B* 1996, *54* (3), 1703-1710.
4. VandeVondele, J.; Hutter, J., *Journal of Chemical Physics* 2007, *127* (11).

APPENDIX E

ADITIONAL COMPUTATIONAL DETAILS

Point charges used for UiO66:

Atom Type	Charge (e)
C1	-0.0762
C3	-0.1039
C2	0.7469
H1	0.1184
H2	0.4807
O1	-1.2298
O3	-1.2372
O2	-0.6761
Zr1	2.5734

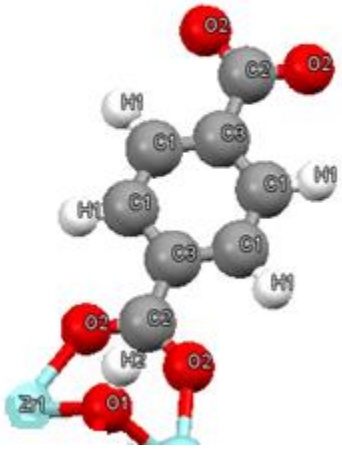

Point charges used for HKUST-1:

Atom Type	Charge (e)
C3	-0.1229
C1	-0.0079
C2	0.6500
H1	0.1339
O1	-0.5436
Cu1	0.8682

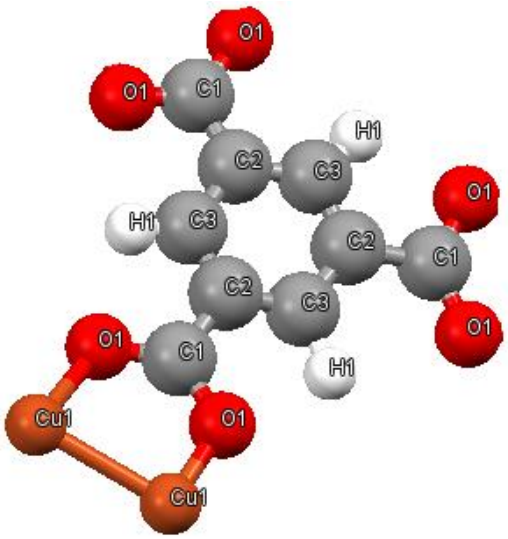

Point charges used for IRMOF-1:

Atom Type	Charge (e)
C3	-0.078
C1	0.698
C2	-0.091
H1	0.121
O1	-1.262
Zn1	1.118

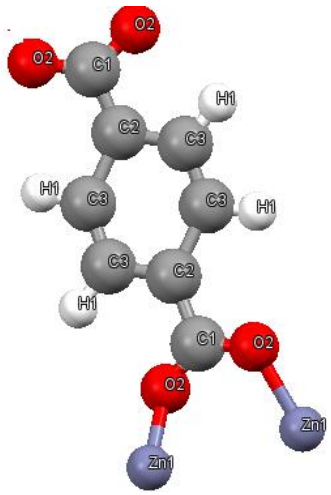

E.1 Loading of oX and eb in a GCMC-simulated binary uptake for a bulk equimolar mixture

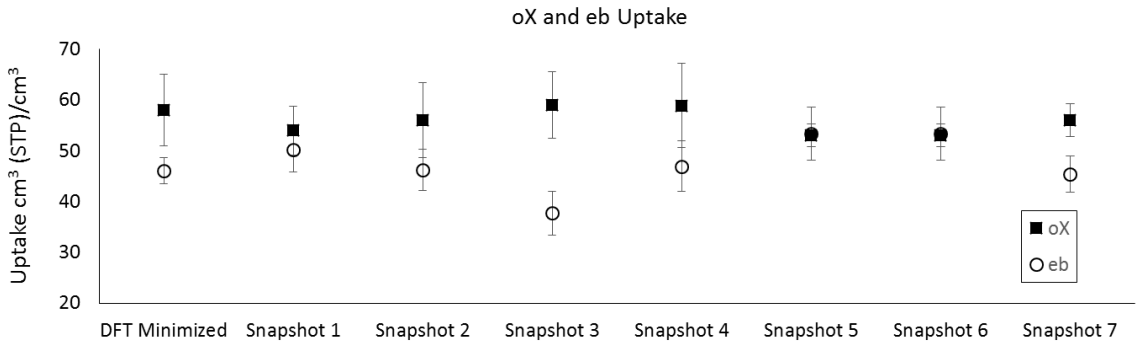

GCMC-simulated loading of oX and eb from a binary equimolar mixture. Loading of eb fluctuates between 37-53 cm^3 (STP)/cm^3 and can be up to 15% different from the uptake predicted for the DFT minimized. Similarly, loading of oX fluctuates between 53-58 cm^3 (STP)/cm^3 and can be up to 8% different from the uptake predicted for the DFT minimized